

ulm university universität
uulm

Advancements in VCSEL Technology: Transverse Mode Control and Matrix-Addressable 2-D Arrays

DISSERTATION

to obtain the academic degree of

DOKTOR-INGENIEUR
(DR.-ING.)

from the Faculty of Engineering and Computer Sciences
of Ulm University

by

ABDELSATTAR MOHAMED ABDELSATTAR GADALLAH
FROM FAYOUM, EGYPT

1st Referee:	PD Dr.-Ing. Rainer Michalzik
2nd Referee:	Prof. Dr. Raimund Hibst
Dean of the Faculty:	Prof. Dr.-Ing. Michael Weber

Oral Examination: Ulm, February 18, 2010

To my wife and my children Mohamed and Ahmed

Acknowledgment

Foremost, I would like to express my sincere gratitude to Priv.-Doz. Dr.-Ing. Rainer Michalzik, the head of VCSELs and optical interconnects group, who gave me the opportunity to perform this work under his supervision. He was a constant source of support for me during my thesis, for which I will be forever grateful. Without his collaboration, this work would not have been possible. He provided me with the thesis ideas of multi-spot shallow surface-relief rectangular-shaped VCSELs and densely-packed two dimensional matrix-addressable VCSEL arrays. I am indebted to him for all the support and knowledge he has given to me.

I wish to thank all people that I have worked with during this thesis. I would like to thank some of them explicitly: Dipl.-Ing. Andrea Kroner for scientific help and discussions during the design of the first mask and the processing of the first sample. I am very grateful to Dipl.-Ing. Ihab Kardosh for some useful discussions concerning the sample processing and helping me weed out the errors in the manuscript of this thesis. I would like to thank Dr.-Ing. Fernando Rinaldi, Dipl.-Phys. Dietmar Wahl, and Philips Technologie GmbH U-L-M Photonics, Ulm for providing me with the semiconductor material to do the different tasks of the thesis. I would like to thank Dipl.-Ing. Anna Bergmann for application of the device in micro-sized particle manipulation such as deflection and trapping. A lot of thanks to Dr.-Ing. Johannes Michael Ostermann for introducing me to different experimental setups, Dipl.-Ing. Wolfgang Schwarz for wire bonding, and Dr.-Ing. Philipp Gerlach for simulation of the excited transverse modes.

I am very grateful to M.Sc. Ahmed Al-Samaneh and special thanks to M.Sc. Mohamed Fikry for helping me to find the errors and providing me useful comments during writing the thesis manuscript.

I would like to thank the students who worked with me in matrix-addressable VCSEL arrays. These students are M.Sc. Shamsul Arafin and M.Sc. Dong Zhang, both did well tasks in this topic.

I am grateful to Mr. Rudolf Rösch for his cooperation in reactive ion etching and metalization process. A lot of thanks to Susanne Menzel for her advices in wet-chemical etching

process. I would like to thank Gerlinde Meixner for her nice drawings.

Many thanks to Sükran Kilic and Christine Bunk, the secretaries of the Institute of Optoelectronics for their help during the thesis time.

And lastly, I would like to thank Prof. Dr. K.J. Ebeling, Prof. Dr. P. Unger and Dr.-Ing. J. Mähnß for providing an excellently suited environment for research.

Advancements in VCSEL Technology: Transverse Mode Control and Matrix-Addressable 2-D Arrays

Abstract

One of the most important keys for the advancement of photonic technology is the development of vertical-cavity surface-emitting lasers (VCSELs). This is attributed to the special features that these devices offer. These features include inherent single-longitudinal mode operation, normal emission to the plane of the active layer(s), small volume, perfect coupling to optical fibers and lenses, low rate of change of wavelength relative to temperature and more. These features, together with its high-speed performance, have made the VCSEL an ideal transmitter in short-distance parallel fiber-optic interconnects.

The development of these lasers opens up new applications such as in spectroscopy, sensing, laser printing, and in longer distance communications. Many of these applications require stable high single-mode output powers of several milliwatts. Unfortunately, VCSELs operate at multi-transverse modes, owing to the large transverse dimensions. To enable an impact on new market areas, much research has been invested to achieve stable high single-mode output power.

For this aim, we contribute with a theoretical analysis, fabrication, and characterization of a novel VCSEL type, namely multi-spot surface-etched single-higher-order transverse mode VCSEL. This device exhibits high power in a single mode and a low differential resistance. The realization of the above mentioned enhancements together with simple manufacturing of the device is the target of the thesis. There are two main differences between this specially designed VCSEL and a standard one. Firstly, concerning the layer structure, a quarter-wavelength antiphase layer is added in order to induce a decrease in top mirror reflectivity. The function of this layer is to induce low reflectivity for the total structure. This layer is then selectively removed in a single processing step by means of wet-chemical etching such that the threshold gain of a desired mode, which is of higher order, is very low compared with that of all other transverse modes. With this method, a single-higher-order transverse mode VCSEL is realized. The second point concerns the shape of the mesa and thus of the

oxide aperture. It is no longer of circular shape, instead it is rectangular, where one side of the aperture is much larger than the other. With this asymmetric transverse cavity, single polarization can be achieved. In addition, the large aperture area of the device compared with other types of single-transverse mode VCSELs ensures low differential resistance as well as low beam divergence. Aside from performance issues, the manufacturing of this VCSEL needs only one additional lithography and etching step, which makes it attractive for commercial fabrication. The continuous-wave maximum output power of the single-higher-order transverse mode and the differential resistance of this device are 12 mW and 18 Ω, respectively. The corresponding single-mode, single-polarization output power is 12 mW. Fabrication processes of this laser are described in more details. As an attractive application of this VCSEL that we have investigated is optical manipulation of micro-particles such as deflection and trapping.

The field intensity profiles of the guided modes are calculated numerically as well as with an analytical approach. The main factors that control the selected mode such as the threshold gain, the confinement factor, and the phase parameter are calculated as a function of the active aperture, aiming to achieve single-higher-order transverse mode emission. For a given aspect ratio of a rectangular oxide aperture, the threshold gain difference between the selected mode and the competitive one is maximized via the optimization of relief diameter and the size of the aperture. Moreover, these calculations can be applied for other wavelength regimes with minor adjustments. The operating laser wavelength in our case is in the vicinity of 850 nm.

In addition, VCSELs are ideally suited to form two-dimensional (2-D) arrays of compact optical sources owing to their low threshold currents and high packing density. In this field, we introduce the manufacturing and characterization of top-emitting 16×16 elements wire-bonded 2-D matrix-addressable VCSEL arrays emitting in the 850 nm wavelength range, which may find future applications such as non-mechanical particle movement with optical multi-tweezers, confocal microscopy or free-space communications with beam steering capability.

Contents

1 Introduction **1**

1.1 Motivation . . . 1
1.2 The Obstacles of Single-Higher-Order Transverse Mode VCSELs . . . 2
1.3 The Obstacles of Densely-Packed Matrix-Addressable VCSEL Arrays . . . 2
1.4 Thesis Overview . . . 3

2 VCSEL Fundamentals **5**

2.1 Special Features of VCSELs . . . 5
2.2 Different VCSEL Structures . . . 6
2.2.1 Selectively Oxidized VCSELs . . . 6
2.2.2 Ion-Implanted VCSELs . . . 8
2.2.3 Etched Air-Post VCSELs . . . 9
2.2.4 Regrown VCSELs . . . 10
2.3 VCSEL Threshold . . . 11
2.3.1 Phase Condition . . . 11
2.3.2 Amplitude Condition . . . 11
2.4 Axial Confinement Factor . . . 12
2.5 Lateral Confinement Factor . . . 13
2.6 Transverse Mode Competition in VCSELs . . . 15
2.7 VCSEL Mirrors . . . 16
2.8 Output Power and Heat Flow in VCSELs . . . 18
2.9 VCSEL Applications . . . 19

3 Waveguiding in VCSELs **21**

3.1 Excited Transverse Modes in VCSELs . . . 21
3.1.1 Rectangular-Shaped VCSELs . . . 21
3.1.2 Circular-Shaped VCSELs . . . 25
3.1.3 The Effect of Heat on the Built-in Guiding . . . 27
3.1.4 Mode Designations in VCSELs . . . 29
3.1.5 Experimentally Reported VCSEL Modes . . . 29
3.2 BV Diagram . . . 31

3.3 Propagation of Higher-Order Transverse Modes in Free Space 33
3.3.1 Hermite–Gaussian Field 33
3.3.2 Laguerre–Gaussian Field 35
3.4 Near-Field of a Single-Higher-Order Transverse Mode VCSEL 36

4 Mode Selection Using Surface Etching in Rectangular-Shaped VCSELs 39
4.1 Introduction 39
4.2 Description of the Device 40
4.3 Analysis and Experimental Results 42
4.4 Near-Field of a Single-higher-order Transverse Mode VCSEL 47
4.5 Far-Field of a Single-Higher-Order Transverse Mode VCSEL 49

5 Semiconductor Technology for Device Manufacturing 51
5.1 Manufacturing of Single-Higher-Order Transverse Mode VCSELs 51
5.2 Manufacturing of Matrix-Addressable VCSEL Arrays 52

6 Experimental Results: Standard Versus Multi-Spot Surface-Etched VCSELs 57
6.1 Standard Rectangular-Shaped VCSEL Characteristics 57
6.1.1 Light–Current–Voltage Characteristics 57
6.1.2 Spectra Measurements 61
6.1.3 Near-Field Measurements 62
6.1.4 Far-Field Measurements 64
6.1.5 Polarization-Resolved LIV Characteristics 64
6.2 Multi-Spot Surface-Etched Single-Mode Rectangular-Shaped VCSELs 67
6.2.1 LIV Characteristics and Spectra 68
6.2.2 Statistical Investigations 72
6.2.3 Near-Field Results 73
6.2.4 Far-Field Intensity Measurements 74
6.2.5 Polarization-Resolved LIV Characteristics 76
6.3 Application of Multi-Spot Surface-Etched VCSELs in Optical Manipulation . 81

7 Experimental Results: Densely Packed Matrix-Addressable VCSEL Arrays 85
7.1 Introduction 85
7.2 Layer Structure 86
7.3 Fabrication Processes 87
7.3.1 Wet-Chemical Etching 87
7.3.2 Reactive-Ion Etching 88
7.4 Laser Characteristics 88
7.4.1 Wet-Etched Arrays 89
7.4.2 Dry-Etched Arrays 90

8 Conclusions 95
8.1 Multi-Spot Surface-Etched Rectangular-Shaped VCSELs 96

8.2 Matrix-Addressable VCSEL Arrays 96

A VCSEL Processing **99**
A.1 Multi-Spot Surface-Etched Rectangular-Shaped VCSELs 99
A.2 Wet-Etched Matrix-Addressable VCSEL Arrays 101
A.3 Dry-Etched Matrix-Addressable VCSEL Arrays 105

B Epitaxial Structures **109**

C List of Symbols and Acronyms **115**

D Publications **119**

Bibliography **121**

Chapter 1

Introduction

In this thesis, a new vertical-cavity surface-emitting laser (VCSEL) type, namely a multi-spot surface-etched rectangular-shaped VCSEL is reported. The device possesses many desirable features such as a high power for single-mode operation (using a surface etching technique), single polarization (using an asymmetric transverse cavity), low differential resistance, small focal depth and potentiality of long lifetime. These special features of this device are of practical interest for applications like spectroscopy, sensing and more. The single mode that oscillates in the device is a higher-order transverse mode. The single mode is selected using an inverted shallow surface relief technique [1]. The governing equations that control the operation of a single-higher-order transverse mode in this device are introduced. An interesting application that we investigated with this device is optical manipulation of micro-sized particles such as optical deflection and trapping.

In addition we report on the fabrication and characterization of densely-packed matrix-addressable VCSEL arrays emitting in the vicinity of 850 nm wavelength.

1.1 Motivation

The special features of VCSELs such as low power consumption, circular beam shape, emission perpendicular to the wafer surface, on-wafer testing before packaging, and efficient high-frequency modulation are providing the motivation for a continued search for new device types. Besides, VCSELs are ideally suited to form two-dimensional arrays of compact optical sources owing to their low threshold currents and high packing density. These make VCSELs attractive light sources for various applications like printing, engraving or pumping of solid-state lasers. As a matter of fact, the development of VCSELs is one of the key advances in photonic technology [2], [3]. However, VCSELs normally operate in multiple transverse modes, due to the large transverse dimensions of the device. Many VCSEL applications require high-power single-transverse mode emission. Hence, much effort has been invested in the research into high-power single transverse mode VCSELs.

For this aim, we contribute with a VCSEL type that provides a high-power single-mode record using shallow etching technique. In this technique, a quarter-wavelength antiphase

layer is added in order to induce a decrease in top mirror reflectivity. This layer is then selectively removed in processing by means of wet-chemical etching, such that the threshold gain of a desired mode is very low compared with that of all other transverse modes. The oscillating laser mode is a higher-order transverse one. The emitted laser wavelength is around 850 nm. The device shows also low differential series resistance record due to the large aperture area compared with that utilized in usual single transverse mode VCSELs.

As a separate device concept, we report on fabrication and characterization of top-emitting 16×16 elements wire-bonded matrix-addressable VCSEL arrays emitting in the vicinity of 850 nm, which may find future applications such as non-mechanical particle movement with optical multi-tweezers, confocal microscopy or free-space communications with beam steering capability.

1.2 The Obstacles of Single-Higher-Order Transverse Mode VCSELs

In order to generate a high-power single transverse mode, it is necessary to utilize a large aperture area to extract more power. However, a large aperture area index-guided VCSEL structure causes difficulties in obtaining single transverse mode operation due to the following facts:

- In an index-guided structure, the effective gain difference between the excited modes is small compared with a gain-guided structure [4]. Hence, as the current increases, the threshold gain of the neighboring mode is reached and more modes can be excited. On the other hand, gain-guided VCSELs are generally less efficient.
- As the aperture area increases, the number of excited transverse modes increases too, in analogy to the guided modes in an optical fiber (Sect. 3.2).

To overcome these challenges, we theoretically investigate the competition between these transverse modes in order to select the desired one. The factors that control this selection are the confinement factor and the threshold gain of each mode. These factors depend on the aperture area and the relief pattern. For each mode, we calculate the confinement factor and the threshold gain to investigate the dependence of these factors on the aperture area and the relief pattern. This allows us select the desired mode by maximizing the difference in threshold gains versus the competitive modes.

1.3 The Obstacles of Densely-Packed Matrix-Addressable VCSEL Arrays

We faced the following obstacles in manufacturing densely-packed matrix-addressable VCSEL arrays.

- In order to achieve matrix addressing in the VCSEL arrays, two etching steps are needed. In the first step, one etches 9 μm down to define the mesa and allow n-metalization above a buffer layer. After this deep etching, one needs to separate the columns by an additional lithographic process and an additional etching step. When applying a photolithographic process to define the columns after the first etching, there is a resolution limit in photolithography caused by this etching. When the distance between columns was 5 μm, the columns could not be separated due to this resolution limit.
- Planarization of this deep etched surface was difficult, however with the proper mask designs this was solved.

An alternative solution to overcome the resolution limit in photolithography (after deep-etched structures) is to use electron beam lithography in order to obtain more densely packed structures. In addition the proper mask design facilitated the planarization difficulty.

1.4 Thesis Overview

The next chapter deals with the essentials of VCSELs, such as their special features, their different structures, their thresholds, and their characteristics. The chapter is then concluded with VCSEL applications.

In Chap. 3, the theoretical basics related to waveguiding in index-guided VCSEL structures is discussed in detail for different aperture shapes. The effect of heat on waveguiding is also considered. The experimentally reported waveguided modes are reported. The propagation of single transverse modes in free space is discussed for different field distributions of the modes.

In Chap. 4, we introduce the governing equations that control the selection of a single-higher-order transverse mode. The factors controlling competition between these transverse modes such as the three-dimensional confinement factor, the threshold gain, and the phase parameter are discussed, aiming to select only one higher-order transverse mode.

The fabrication processes that are utilized to manufacture both the multi-spot surface relief VCSELs and matrix-addressable VCSEL arrays are discussed in more detail in Chap. 5.

In Chaps. 6 and 7, the experimental results of the thesis are reported. Chapter 6 presents the experimental results of both normal and multi-spot surface-etched rectangular-shaped VCSELs. These results include the light–current–voltage (LIV) characteristics, spectral features, near-field and far-field intensity measurements, and polarization-resolved LIV curves and spectra.

In Chap. 7, the experimental results of two generations of matrix-addressable VCSEL arrays, namely wet-etched and dry-etched matrix-addressable arrays are discussed. The thesis is finally concluded in Chap. 8 with a summary of the work.

Chapter 2

VCSEL Fundamentals

The vertical-cavity surface-emitting laser (VCSEL) is a certain type of semiconductor laser diode that has its radiation normal to the plane of the active material. It offers a lot of advantages compared with edge-emitting lasers. In this chapter, we give introduction about VCSEL structures, operation mechanism, advantages of this laser, and some possible applications.

2.1 Special Features of VCSELs

There are some unique features of VCSELs that allow them to replace conventional laser diodes or to open up new applications. The following is a concise description of these features.

- The emitted laser radiation is normal to the plane of the active region. This feature makes the devices well suited for fabrication in arrays, including two-dimensional arrays. In addition, this feature allows on-wafer testability, which has been a significant aspect of VCSEL production for parallel data communications. Moreover, when the laser emission is normal to the surface, incorporation of optical elements and flexibility in packaging are facilitated.
- The VCSEL is a small-volume laser, it could be of about 0.06 μm^3 [3]. This leads to ultra-low threshold currents of less than 100 μA [5]. In addition, a low laser threshold voltage only slightly higher than the bandgap voltage can be achieved [6]. The lower is the threshold current, the higher is the potential modulation speed, which is desirable for high-speed communications. In addition, the small threshold current allows formation of densely-packed two-dimensional VCSEL arrays.
- Inherent single longitudinal mode emission is achieved, owing to the short inner cavity length. However, multiple transverse modes are excited if no selective mechanism is utilized to guarantee single transverse mode operation.
- VCSELs with a circular aperture put out a circular output beam. This simplifies coupling into optical components such as lenses or fibers.

- Wavelength and thresholds are relatively insensitive against temperature variation. The rate of change of wavelength with respect to temperature for a VCSEL is 0.06 nm/K [7], while that of edge emitting lasers is 0.32 nm/K [7].

2.2 Different VCSEL Structures

Essentially there are four different VCSEL types, selectively oxidized VCSEL, ion-implantation VCSEL, etched air-post VCSEL and buried hetrostructure VCSEL (regrown VCSEL). The most efficient one is selectively oxidized or oxide-confined VCSEL. We start with it.

2.2.1 Selectively Oxidized VCSELs

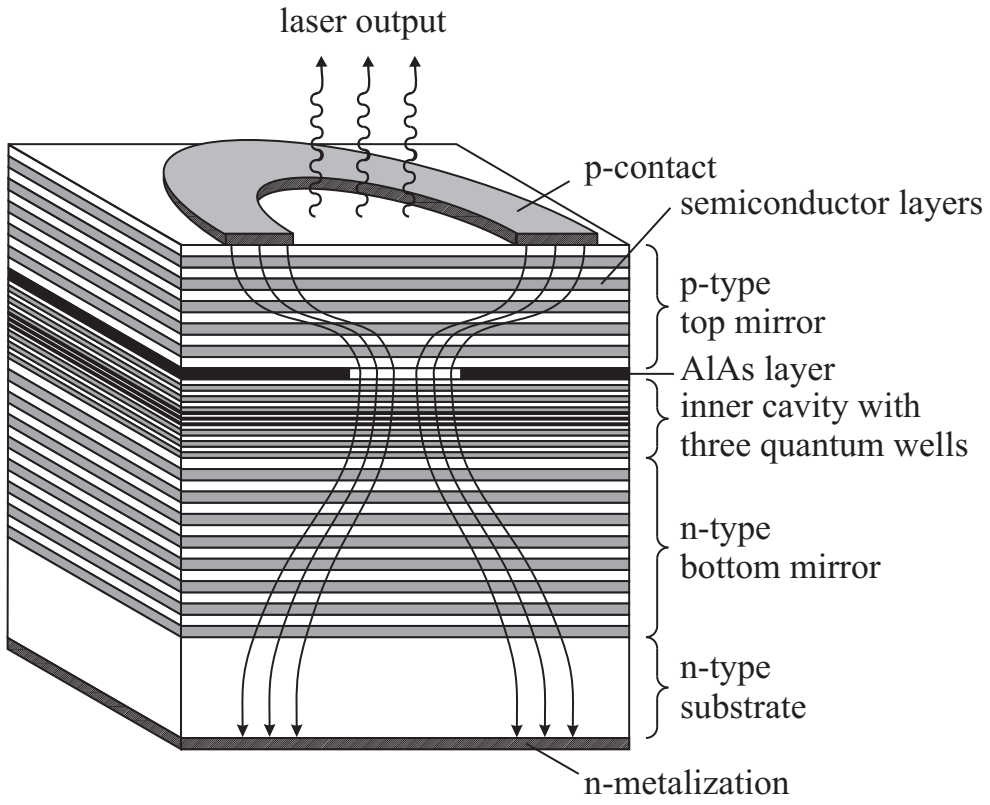

Figure 2.1: Sketch demonstrating an oxide-confined VCSEL structure.

Figure 2.1 shows a schematic drawing of such type of VCSEL. Grown above the n-doped substrate is an n-type distributed Bragg reflector (DBR). In the AlGaAs material system, silicon is utilized as an n-doping material. One pair of this DBR mirror consists of two layers, one with high refractive index $n_{\mathrm{B,h}}$ and the other with low refractive index $n_{\mathrm{B,l}}$. The corresponding thicknesses of these layers are $\lambda/(4n_{\mathrm{B,h}})$ and $\lambda/(4n_{\mathrm{B,l}})$, respectively, where λ is the laser wavelength in free space. The constructive interference occurring between the reflected waves from such pairs leads to high reflectivity. The typical number of these n-DBR

pairs is between 35 and 40. This number depends on the refractive index contrast between the layers of the pair. Above these n-DBR pairs is an n-doped graded-index hetrostructure to confine the carriers in the active medium. Then the active medium consists of quantum wells for efficient VCSELs. The number of quantum wells depends on the application. If the optical losses are very low, the lowest threshold can be obtained with a single QW. Three quantum wells, each 8 nm thick is a common design that provides higher laser output power as well as low threshold currents. The QWs are often separated 10 nm thick barrier layers. The laser wavelength emitted from the active medium depends on the material type as well as the inner cavity design. The most common laser emission wavelengths are 850 nm and 980 nm. The materials utilized corresponding to these wavelengths are GaAs and InGaAs, respectively. VCSEL emission wavelengths in the visible [8] as well as in the vicinity of 1.55 µm are also achieved [9]. Then there is a p-doped region with a higher bandgap energy to confine the carriers.

Above these layers, an AlAs oxide layer is grown. The function of this layer is twofold: When part of it is oxidized, current confinement as well as optical guiding take place. The oxidation process of the AlAs layer occurs when it is exposed to temperatures from 350 to 500 °C in a steam environment. A stable and reproducible oxidation technology requires control of carrier gas flow and the oxidation furnace temperature. These criteria can be met by employing mass-flow controllers to regulate the steam flow, supplied by bubbling an inert gas through water at a constant temperature into a temperature-controlled furnace. The lateral oxidation rate of AlAs has a linear temperature dependence [10].

Above this layer the p-DBR mirrors are grown. Carbon is utilized for p-doping. The last layer is grown with a heavily p-doping material to enhance current injection. Typical layer structures that we utilized in this thesis are listed in App. B.

The oxide-confined structure has some advantages compared with the other structures. First, the dielectric aperture not only confines the current, but also guides the modes. After the oxidation process, there is a built-in guiding caused by the lower refractive index of the oxidized part. Moreover, by controlling this step-index contrast in refractive index, one can obtain single transverse mode oscillation. The typical index step caused by this process is 2×10^{-3}. In addition, the aperture diameter can be small, leading to an ultra-low threshold current of the device.

Top- and bottom- emission oxide-confined VCSEL structures are possible. However, top-emission structure is more convenient due to avoiding thining of the substrate, which is required in bottom-emission structures.

Because carriers are transported through the p- and n-DBR mirrors, different approaches have been utilized to minimize the barriers at the numerous interfaces. One such method is, instead of utilizing high refractive index contrast between the mirror pair, to utilize graded-index layers such that the barrier will not be step-like, but graded. The same is true also for the doping of such pairs. This is what we utilized to reduce the barriers at the different interfaces. Alternatively, intracavity contacts are used for biasing the VCSELs [11].

2.2.2 Ion-Implanted VCSELs

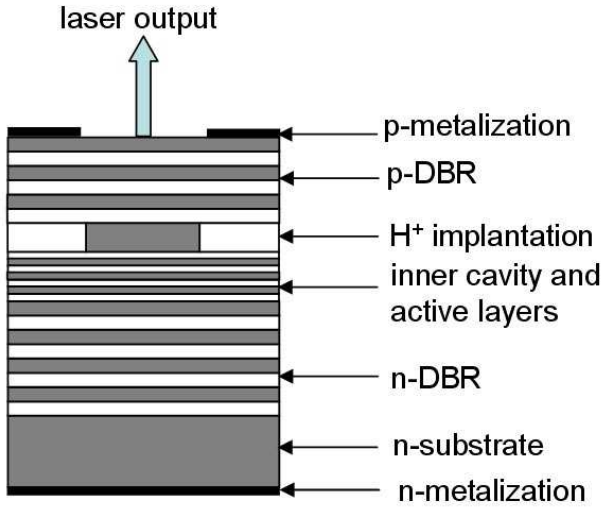

Figure 2.2: Ion implanted VCSEL Schematic.

A sketch demonstrating an ion-implanted VCSEL structure is shown in Fig. 2.2. The main difference between oxide-confined and ion-implanted VCSEL structures is the current confinement mechanism. While in oxide-confined VCSELs, selective oxidation of a certain layer is utilized to restrict the current, an ion-implantation process is utilized to confine the current in ion-implanted VCSELs.

Ion implantation into the top DBR mirror is utilized to concentrate the injected current into the active medium. The implanted ions create crystal vacancies. Such damage leads to regions of high resistivity. The ion implantation energy required to achieve current confinement within a VCSEL depends upon the mass of the ion used and the implant depth desired. Various ion species have been utilized such as H^+, O^+, N^+, and F^+, although proton implants are the most common.

similarly to oxide-confined VCSEL structures, both top- and bottom-ion implanted VCSEL structures are possible. However, top-emission ion-implanted VCSEL structure is convenient just to avoid thining of the substrate.

Compared with an oxide-confined structure, no built-in optical guiding occurs after the implantation process since the refractive index change is very small. In addition, one cannot decrease the aperture beyond a certain limit because of unavoidable lateral ion scattering. This leads to higher threshold currents compared with oxide-confined structures. Further, the implantation process has to be stopped some distance above the active region in order to make sure that no damage of the quantum wells can occur. This leads to lateral current spreading above the active region, i.e., some current is lost for stimulated recombination. In other words, the laser current injection efficiency is reduced.

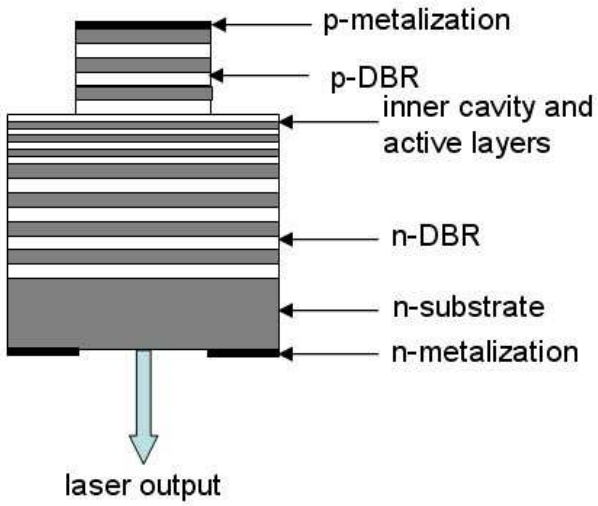

Figure 2.3: Sketch demonstrating an etched air-post VCSEL structure.

2.2.3 Etched Air-Post VCSELs

Figure 2.3 demonstrates a sketch of the etched air-post VCSEL. The etch depth is a trade-off between the electrical and optical loss experienced by an air-post VCSEL. When the etch stops at the p-DBR mirror, some current spreads away from the active region. On the other hand, when one etches into the n-DBR mirror, the exposed active region suffers from non-radiative recombination at the side walls. In general, the etch is usually stopped just above the active layer to avoid surface recombination of carriers. In this case, the current is confined to the lateral dimension of the top mesa, however, carriers are free to diffuse laterally in the active region. In addition, the thermal resistance of etched air-post VCSELs is high due to the removal of the semiconductor surrounding the etched mesa. In order to overcome this problem, ideally the etched mesa is encapsulated with an insulating material having a high thermal conductivity.

Both chemical wet-etching as well as dry-etching have been utilized to remove the epitaxial material around the laser cavity. Chemical wet-etching has several limitations, such as the undesirable undercut edge profile and the lack of process control to achieve a small size. However, with dry-etching such as chemically assisted ion beam etching (CAIBE) or reactive ion etching (RIE), small diameter etched air-post VCSELs can be accomplished.

Both top- and bottom-emission etched air post VCSEL structures are possible. However, in this case, the area of the top side becomes small after etching. Hence, bottom-emission etched air-post VCSEL structure is more convenient, since the p-metalization can be applied throughout the top side. This leads to an enhancement in the electrical properties of the laser. However, one needs to thin the substrate to avoid absorption for the laser wavelength.

Since just air is surrounding the etched mesa, strong index-guiding of the modes occurs which could lead to a reduction of the threshold current. The drawbacks of etched air-post VCSELs are greater diffraction and scattering losses, non-radiative recombination, and high thermal

resistance without utilizing materials having a higher thermal conductivity surrounding the etched mesa.

2.2.4 Regrown VCSELs

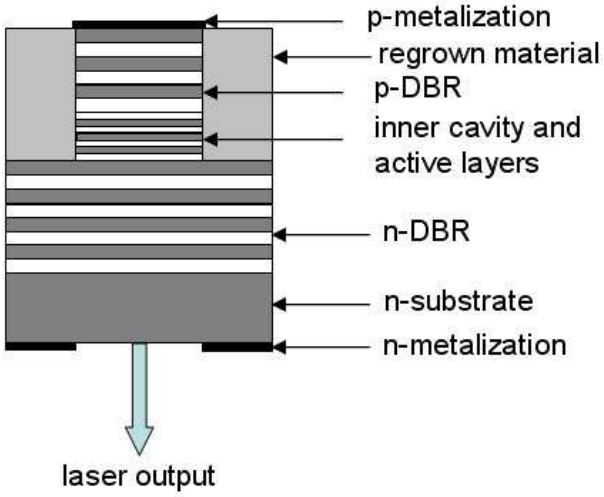

Figure 2.4: Sketch demonstrating a regrown VCSEL structure.

Figure 2.4 is a schematic drawing of a buried hetrostructure VCSEL. It is the only structure from all the above mentioned that provides lateral carrier confinement. In addition, when the regrown material surrounding the active material has a lower refractive index, this structure would include all the desired lateral confinements. However, the fabrication of such structures has been met with only partial success. Much of the problems result from the difficulties with direct regrowth over a deeply etched mesa containing high Al content layers. Surface passivation with sulfide treatments has been attempted with encouraging results [12] but no technique of stabilizing the surface has been found.

Both top- and bottom-emission regrown VCSEL structures are possible. However, in this case the area of the top side becomes small after etching. Hence, bottom-emission regrown VCSEL structure is more convenient, since the p-metalization can be applied throughout the top side. This leads to an enhancement in the electrical properties of the laser. However, one needs to thin the substrate to avoid absorption for the laser wavelength.

For the fabrication of such types of structures, first a dry etching process to remove the materials surrounding the active medium is done followed by regrowth of another higher bandgap material. Such regrowth process can be done either by liquid phase epitaxy, molecular beam epitaxy or by metal organic vapor phase epitaxy. The main advantages of such structure are optical confinement, current confinement, and restored heat sink. Owing to the difficulties in regrowth, no commercial VCSELs of this type are available.

2.3 VCSEL Threshold

When forward bias is applied to a VCSEL structure, the carriers (electrons and holes) are transported toward the quantum well(s). Radiative and non-radiative recombination occurs between electrons and holes, leading to creation of radiation. When such radiation overcomes the losses, the laser can oscillate. Such losses are mainly due to internal losses and light out-coupling losses. The internal losses are due to free-carrier or fundamental absorption and scattering at interfaces. Out-coupling losses are due to some fraction of radiation is transmitted through the DBR mirrors. For laser radiation to occur, the number of photons should remain unchanged after one round-trip, in other words the amplitude of the field should be constant. In addition, the phase of the electric field must repeat itself after one round-trip. The following is a discussion of both cases.

2.3.1 Phase Condition

The phase condition is that the phase of the electric field must repeat itself after one round-trip, i.e.,

$$m\lambda = 2n_{\mathrm{cav}}L, \tag{2.1}$$

where L is the inner cavity length, n_{cav} is the average refractive index in the cavity, λ is the vacuum wavelength, and m is a positive integer. For most VCSEL cavities, the inner cavity length is one material wavelength, i.e., $m = 2$.

2.3.2 Amplitude Condition

The amplitude condition can be written as [2]

$$\Gamma g_{\mathrm{th}} = \alpha_{\mathrm{i}} + \alpha_{\mathrm{m}}, \tag{2.2}$$

where Γ is the three-dimensional mode confinement factor, g_{th} the laser threshold gain, α_{i} the intrinsic cavity loss, and α_{m} the mirror loss. Obviously, the threshold gain can be reduced by enhancing the confinement factor [13].

The three-dimensional mode confinement factor is given by

$$\Gamma = \Gamma_{xy}\Gamma_z, \tag{2.3}$$

where Γ_{xy}, Γ_z are the lateral confinement factor and axial confinement factor, respectively. The intrinsic cavity loss is given by [14]

$$\alpha_{\mathrm{i}} = \Gamma_z\alpha_{\mathrm{a}} + (1 - \Gamma_z)\alpha_{\mathrm{p}} + \alpha_{\mathrm{sc}}, \tag{2.4}$$

where α_{a} is the free-carrier loss within the active segments, α_{p} is the free-carrier loss within the passive segments, and α_{sc} is general scattering loss throughout the cavity due to sidewall

roughness. The coupling mirror loss is given by [15]

$$\alpha_{\mathrm{m}} = \frac{1}{L_{\mathrm{eff}}} \ln \frac{1}{\sqrt{R_{\mathrm{t}} R_{\mathrm{b}}}}, \tag{2.5}$$

where L_{eff}, R_{t}, R_{b} are the effective cavity length, the reflectivity of the top DBR mirror, and the reflectivity of the bottom DBR mirror, respectively. The effective cavity length in (2.5) is given by [15]

$$L_{\mathrm{eff}} = L + l_{\mathrm{eff,t}} + l_{\mathrm{eff,b}} \tag{2.6}$$

where $l_{\mathrm{eff,t}}$ and $l_{\mathrm{eff,b}}$ are the effective top and bottom mirror penetration depths, respectively. They are given by [2]

$$l_{\mathrm{eff,t,b}} = \frac{\lambda}{4\Delta n_{\mathrm{B}}} r_{\mathrm{m}} \approx \frac{\lambda}{4\Delta n_{\mathrm{B}}} \tanh\left(\frac{m\Delta n_{\mathrm{B}}}{n_{\mathrm{B}}}\right) \tag{2.7}$$

where Δn_{B} is the difference in refractive index of the mirror pair, n_{B} is the average refractive index of the mirror pair, r_{m} is the maximum amplitude reflectivity of the top or bottom mirror, and m is the number of mirror pairs. For structure M04-050 (see App. B) with the number of mirror pairs equal to 23 for the top mirror and 38.5 for the bottom mirror, and from Fig. 2.5, $\Delta n_{\mathrm{B}} = 0.43$, $n_{\mathrm{B}} = 3.275$. This leads to $l_{\mathrm{eff,t}} = 0.492$ µm, $l_{\mathrm{eff,b}} = 0.493$ µm, and $L_{\mathrm{eff}} = 1.24$ µm.

Axial and lateral confinement factors are of great importance to determine which transverse mode has the lowest threshold. The following is detail to determine such factors.

2.4 Axial Confinement Factor

The axial confinement factor is defined as [2]

$$\Gamma_z = \xi \frac{N_{\mathrm{w}} L_{\mathrm{w}}}{L_{\mathrm{eff}}}, \tag{2.8}$$

where ξ, N_{w}, and L_{w} are the axial enhancement factor, the number of quantum wells and the thickness of each quantum well, respectively. Figure 2.5 shows the numerical axial field distribution near the active medium (left axis) and the refractive index distribution of the different layers (right axis) calculated using the transfer matrix method [15]. Such field distribution is sinusoidal in the inner cavity, and the field envelope decays exponentially in the top and bottom DBRs. For these field distributions, the axial enhancement factor is [15]

$$\xi = 1 + \frac{\lambda}{4\pi n_{\mathrm{cav}}} \frac{\Sigma_{i=1}^{N_w} \sin(4\pi n_{\mathrm{cav}} z_{ih}/\lambda) - \sin(4\pi n_{\mathrm{cav}} z_{il}/\lambda)}{\Sigma_{i=1}^{N_w} z_{ih} - z_{il}}, \tag{2.9}$$

where quantum wells are located at positions $z_{il} \leq z \leq z_{ih}$ with $i = 1, ..., N_w$. With the axial propagation constant $\beta = 2\pi n_{\mathrm{cav}}/\lambda$, (2.9) reduces to

$$\xi = 1 + \frac{1}{2\beta} \frac{\Sigma_{i=1}^{N_w} \sin(2\beta z_{ih}) - \sin(2\beta z_{il})}{\Sigma_{i=1}^{N_w} z_{ih} - z_{il}}. \tag{2.10}$$

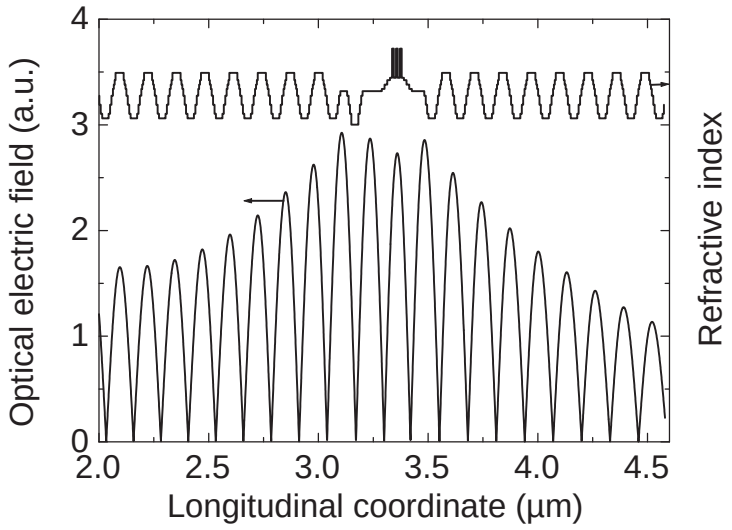

Figure 2.5: Axial field distribution (left axis) and refractive index distribution (right axis) as a function of the axial coordinate in the vicinity of the active medium.

The axial enhancement factor can be as large as 2, if a thin active layer is centered at the standing-wave peak in the cavity. On the other hand it is zero if the thin active layer is centered at a standing-wave node. In our case, $\lambda = 0.85$ μm, $N_{\mathrm{w}} = 3$, $L_{\mathrm{w}} = 8$ nm, $n_{\mathrm{cav}} = 3.3$, and the barrier thickness = 10 nm we get $\xi = 1.82$.

By substitution in (2.8), with $\xi = 1.82$, $N_{\mathrm{w}} = 3$, $L_{\mathrm{w}} = 8$ nm, and $L_{\mathrm{eff}} = 1.24$ μm, the axial confinement factor is 0.0225.

2.5 Lateral Confinement Factor

The transverse field distributions emitted from a VCSEL depend on the shape and dimension of the active aperture, the layer structures, heat effects, and pumping inhomogeneity or the so-called current spreading. Figures 2.6 and 2.7 show the simulated intensity distributions with the mode designations emitted from a circular-shaped VCSEL and a rectangular-shaped VCSEL, respectively. The active aperture diameter of the circular-shaped VCSEL is 10 μm and the active aperture dimension of the rectangular-shaped VCSEL is 10 μm × 80 μm. In the simulation, it is assumed that the refractive index of the core is n_1 surrounded by a less refractive index of the cladding $n_2 = n_1 - \Delta n$. For more details about the simulation of such modes, see Sect. 3.1.1. The lateral confinement factor [4] of the aperture $\Gamma_{xy,A,i}$ for a transverse mode i is defined as the ratio of the power in the active aperture P_A divided by the power of the mode P_i , i.e.,

$$\Gamma_{xy,A,i} = \frac{P_A}{P_i}. \tag{2.11}$$

$\Gamma_{xy,A,i}$ depends on the shape and dimension of the aperture. The dependence of $\Gamma_{xy,A,i}$ on the aperture area for circular-shaped VCSELs for the modes LP_{01} and LP_{11} are demonstrated in Fig. 2.8. As seen from the figure, with increasing the aperture area, the confinement factor

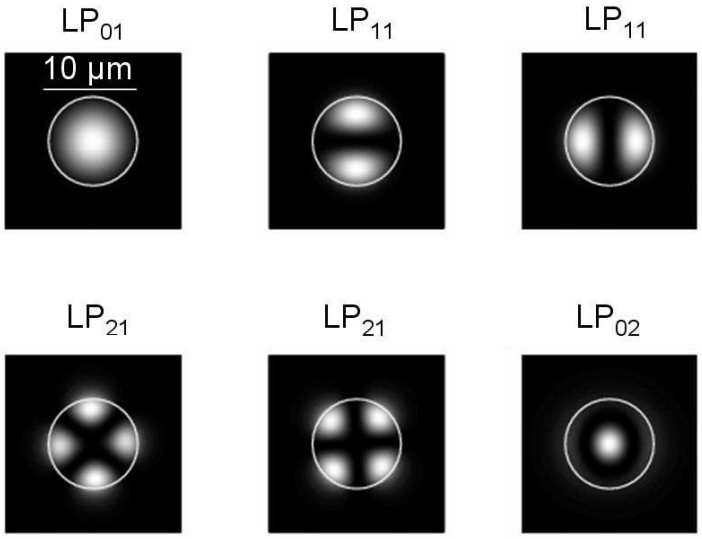

Figure 2.6: Simulated intensity profiles of the lowest 6 transverse modes and their designations in a circular-shaped VCSEL. The active aperture diameter is 10 µm, λ = 850 nm, n_1 = 3.3, and $\Delta n = 2\times10^{-3}$.

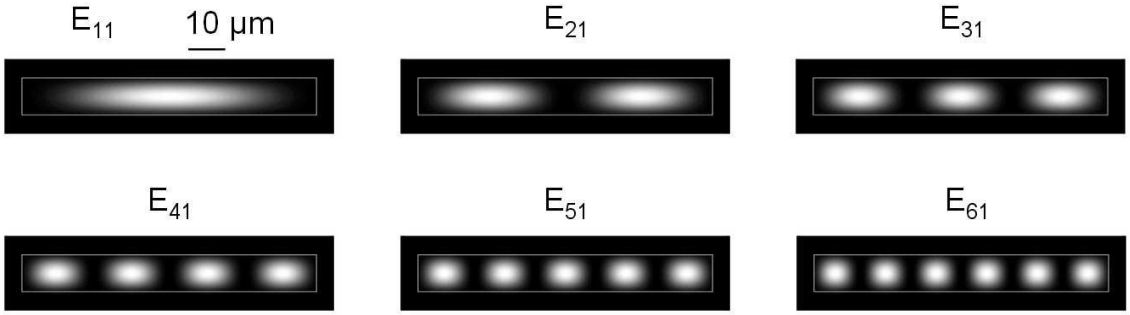

Figure 2.7: Simulated intensity profiles of the lowest 6 transverse modes and their designations in a rectangular-shaped VCSEL. The active aperture area is 10 µm × 80 µm, λ = 850 nm, n_1 = 3.3, and $\Delta n = 2\times10^{-3}$.

increases. Moreover, the value of $\Gamma_{xy,A}$ for the fundamental mode is the highest one among all other transverse modes. Also indicated in the graph is the difference between the confinement factors of the fundamental mode and the LP_{11} mode. Such difference decreases with increasing aperture area. Similarly, Fig. 2.9 plots the dependence of the lateral confinement factor as a function of the aperture area for the rectangular-shaped VCSEL with aspect ratio equal to 8 for the modes E_{91} and $E_{10\,1}$ (for more details about these modes, see Sect. 3.1.1).

For higher-order modes such as E_{91} and $E_{10\,1}$ the lateral confinement factor is small compared with that of the fundamental mode. In addition, the difference between the lateral confinement factors for the modes E_{91} and $E_{10\,1}$ is small compared with that of LP_{01} and LP_{11}. Moreover, as the aspect ratio increases from 8 to 10, the difference between the confinement

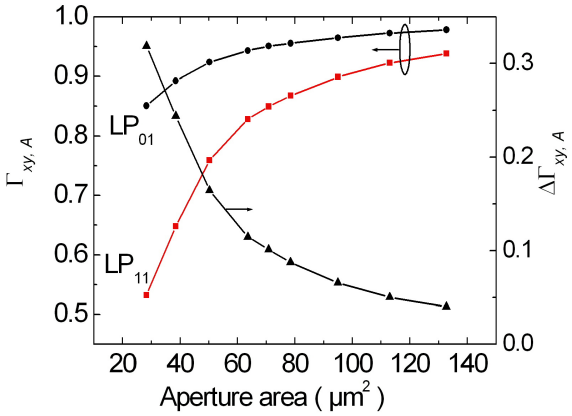

Figure 2.8: Lateral confinement factor (left axis) and the difference in lateral confinement factors (right axis) for the modes LP_{01} and LP_{11} as a function of the aperture area for circular-shaped VCSELs.

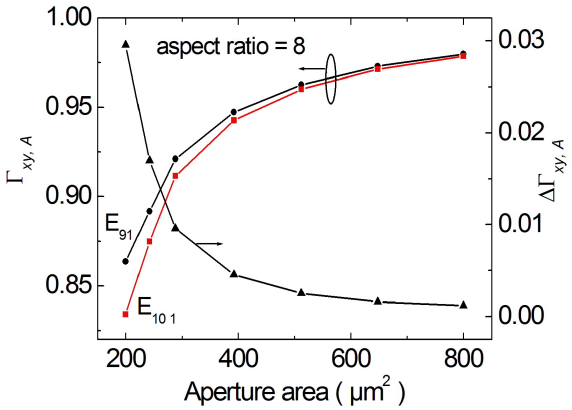

Figure 2.9: Lateral confinement factor (left axis) and the difference in lateral confinement factors (right axis) for the modes E_{91} and $E_{10\,1}$ as a function of the aperture area for rectangular-shaped VCSELs with aspect ratio = 8.

factors for the modes E_{91} and $E_{10\,1}$ gets smaller, as shown in Fig. 2.10.

2.6 Transverse Mode Competition in VCSELs

In the longitudinal direction of a VCSEL, there is only one oscillating longitudinal mode. This is attributed to the short inner-cavity length of VCSELs and the narrow stop-band of the VCSEL mirrors. However, in the transverse direction, there are a lot of transverse modes that can oscillate when the active aperture is large. The number of excited transverse modes as a function of the aperture area for a typical VCSEL structure is discussed in Sect. 3.2. When no selection mechanism is applied to select a certain transverse mode, the fundamental mode has the highest value of $\Gamma_{xy,A,i}$. This lateral confinement factor for the transverse mode

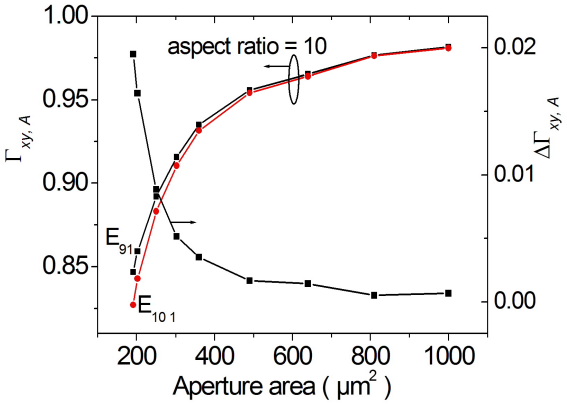

Figure 2.10: Lateral confinement factor (left axis) and the difference in lateral confinement factors (right axis) for the modes E_{91} and $E_{10\,1}$ as a function of the aperture area for rectangular-shaped VCSELs with aspect ratio = 10.

is a measure for its effective gain. Therefore, it is defined as [4]

$$\Gamma_{xy,A,i} = \frac{g_{eff,i}}{g}, \tag{2.12}$$

where $g_{eff,i}$ is the effective gain for the mode i, and g is the material gain. Hence, as $\Gamma_{xy,A,i}$ is high for a certain transverse mode, the threshold gain of this mode will be low, as implied in (2.2). The lower is the mode order, the higher is the lateral confinement factor, as seen also from Figs. 2.8–2.10. This means the fundamental mode is always has the lowest laser threshold, unless an external mechanism is applied to select a certain higher order transverse mode. Thus selecting a higher-order transverse mode becomes a challenge. In Sect. 4.3, we introduce the governing factors that control higher-order transverse mode selection when using the shallow relief etching technique to select the mode.

2.7 VCSEL Mirrors

The short cavity of a VCSEL reduces the gain per round-trip of the mode and thus a high reflectivity for the laser wavelength is required as well as reduction of losses. The distributed Bragg reflectors (DBRs) provide high reflectivity for VCSELs. DBRs consist of multiple layers with alternating high and low refractive index. The maximum possible amplitude reflectivity is obtained with quarter-wave thick dielectric layers. The peak power reflectivity of the top DBRs and bottom DBRs of a VCSEL are given by [15]

$$R_{\mathrm{t,b}} = \left(\frac{1 - b_{\mathrm{t,b}}}{1 + b_{\mathrm{t,b}}}\right)^2 \tag{2.13}$$

with

$$b_{\mathrm{t}} = \frac{n_{\mathrm{S}}}{n_{\mathrm{C}}} \left(\frac{n_{\mathrm{B,1}}}{n_{\mathrm{B,h}}}\right)^{2m} \tag{2.14}$$

and

$$b_{\mathrm{b}} = \frac{n_{\mathrm{B,1}}^2}{n_{\mathrm{S}} n_{\mathrm{C}}} \left(\frac{n_{\mathrm{B,1}}}{n_{\mathrm{B,h}}} \right)^{2m}, \tag{2.15}$$

where n_{S} and n_{C} are the substrate and cladding refractive indices, respectively. For calculating the peak power reflectivity R_{t} of the top DBR, it is assumed that a wave is incident from a cladding and transmitted through m mirror pairs into the substrate, which is air. In case of calculating the bottom peak reflectivity R_{b}, it is assumed that a wave is incident from the cladding passes through m mirror pairs, then a low refractive index layer and then the high-index substrate. Figure 2.11 shows the power reflectivity R and a magnitude $\ln(1/R)$ proportional to the mirror loss for both the top mirror, where the last interface is air (circles), and the bottom mirror, where the last interface is the substrate (squares). Note the logarithmic scale of the right axis. In this calculation, the two layers forming one

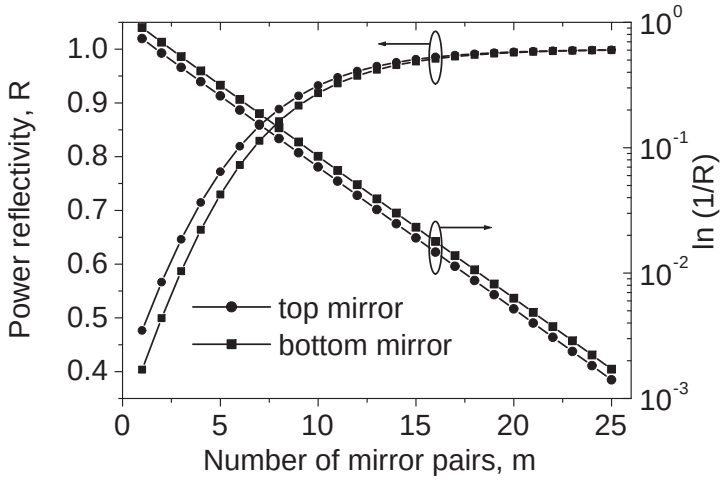

Figure 2.11: Peak power reflectivity (left axis) and a magnitude proportional to the mirror loss (right axis). The circles correspond to the top mirror in the VCSEL and the squares correspond to the bottom mirror.

mirror period are $Al_{0.2}Ga_{0.8}As/Al_{0.9}Ga_{0.1}As$ with refractive indices $n_{\mathrm{B,h}} = 3.49$, and $n_{\mathrm{B,1}} = 3.06$, respectively. Such a pair is typically utilized in our VCSEL structures (see App. B). The power reflectivity of the top mirror is higher than that of the bottom mirror for the same number of periods, since the refractive index contrast of the last pair in case of the top mirror is higher than that of the bottom mirror. Another important dependence is the power reflectivity as a function of the wavelength.

Multilayer dielectric mirrors and other reflecting layers in a VCSEL are generally analyzed by a transmission matrix approach that includes the individual properties of the various layers [15], [16]. Figure 2.12 shows the numerical power reflectivity of the bottom mirror as a function of the wavelength for $Al_{0.2}Ga_{0.8}As/Al_{0.9}Ga_{0.1}As$ pairs and 38.5 periods.

There is a flatness of the reflectivity near the Bragg resonance, the so-called the stop-band of the mirror. Such spectral width of the stop-band is given by [17]

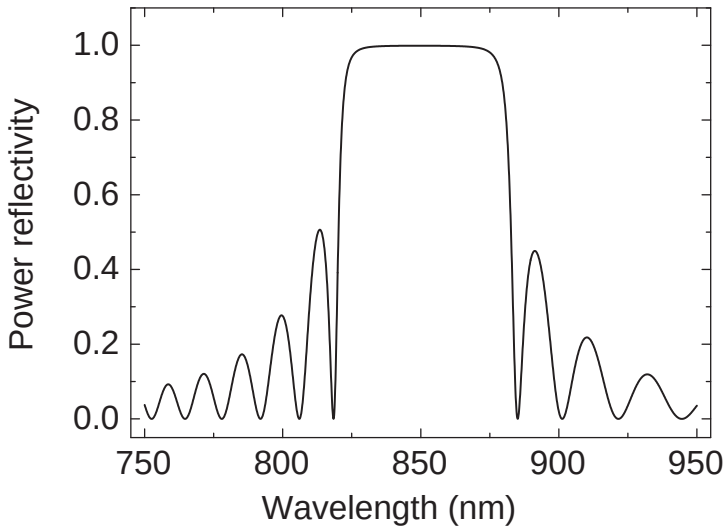

Figure 2.12: Power reflectivity of a bottom DBR with 38.5 periods of $Al_{0.2}Ga_{0.8}As$/ $Al_{0.9}Ga_{0.1}As$.

$$\Delta\lambda_{\mathrm{sb}} = \frac{2\lambda_{\mathrm{B}}\Delta n_{\mathrm{B}}}{\pi n_{\mathrm{B}}}, \tag{2.16}$$

where Δn_{B} is the difference in refractive index of the materials forming the mirror pair and n_{B} is the effective refractive index of the mirror. It is given by

$$n_{\mathrm{B}} = 2\left(\frac{1}{n_{\mathrm{B,h}}} + \frac{1}{n_{\mathrm{B,l}}}\right)^{-1}. \tag{2.17}$$

The calculated reflectance spectrum using the transfer matrix method for a monolithic VCSEL emitting in the vicinity of 850 nm using layer structure M04-050 (see App. B) is depicted in Fig. 2.13. The dip in the center of the mirror stop-band corresponds to the cavity resonance and thus the VCSEL emission wavelength.

2.8 Output Power and Heat Flow in VCSELs

Above the threshold current I_{th} and below the thermal rollover, the emitted output power P_{out} from a VCSEL increases linearly with the pumping current I [18], i.e.,

$$P_{\mathrm{out}} = \frac{h\nu}{q}\eta_{\mathrm{d}}(I - I_{\mathrm{th}}) \tag{2.18}$$

where $h\nu$ is the laser photon energy, q is the electron charge, and η_{d} is the differential quantum efficiency. The differential quantum efficiency is evaluated from the slope of the output power versus current, i.e.,

$$\eta_{\mathrm{d}} = \frac{q}{h\nu}\frac{dP_{\mathrm{out}}}{dI}. \tag{2.19}$$

A crucial consideration for efficient VCSEL performance is the heat removal from the device. As the pumping current increases, there is a rise in the junction temperature. This rise ΔT

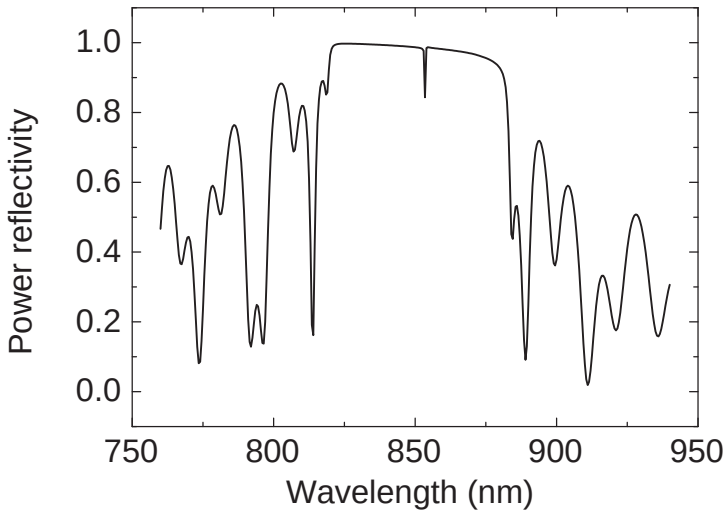

Figure 2.13: Power reflectivity spectrum of a monolithic VCSEL for structure M04-050, see App. B.

is related to the thermal conductivity of the substrate σ_{T} and the effective aperture radius a_{eff} through [19]

$$\Delta T = \frac{P_{\mathrm{IV}} - P_{\mathrm{out}}}{4 a_{\mathrm{eff}} \sigma_{\mathrm{T}}}, \tag{2.20}$$

where P_{IV} is the input electric power and P_{out} is the emitted light power. The thermal conductivity of GaAs is 0.44 W/(cm K). This equation assumes heat flow from a circular area with radius a_{eff} into a half-space filled with a medium with thermal conductivity σ_{T}.

2.9 VCSEL Applications

Owing to low-cost manufacturing, small size, high efficiency, capability of high-speed modulation, ability to be manufactured in one-dimensional and two-dimensional arrays, ease of packaging, collimating and coupling to optical fiber, VCSELs are of practical interest for many applications [20]. The following are just some of them:

- VCSELs are ideal light sources for optical data communications [21]. Data transmission at 10 Gbit/s is possible using this light source [22].
- VCSELs are a convenient light source for optical tweezers [23]–[25], where contact-free optical manipulation of biological material like DNA or cells with forces in the pN range is exploited in mechanical and spectral studies as well as transport and sorting applications.
- VCSELs have attracted attention in confocal microscopy [26], in which one or many isolated points of illumination shine on one or many isolated points of the object, and these are detected by one or many isolated points of detectors. The main advantage of VCSELs in this application is the high packing density of one- or two-dimensional arrays.

- VCSELs are also well suited for computer mice. With polarization-controlled single transverse mode VCSELs, unwanted movements of the pointer are avoided in optical mice [27].
- VCSELs can be used for optical scanners [28].
- Coherent VCSELs with single-mode single-polarization emission are attractive sources in spectroscopic applications. These single-mode applications allow quantitative detection of, e.g., oxygen (763 nm) [29] and moisture (795 nm). In addition, this coherent radiation can be used to excite Cs or Rb in atomic clocks [30].

Chapter 3

Waveguiding in VCSELs

The degree of waveguiding varies from one VCSEL structure to another. In air-post VCSELs it is maximum, and in proton-implanted VCSELs it is minimum. In both, oxide-confined and regrown structures, one can control it. This guiding effect influences the VCSEL threshold by confining the beam. In this chapter, we introduce details about the transverse field distributions of the guided transverse modes in oxide-confined structures. Both the geometry and heat effects are considered.

3.1 Excited Transverse Modes in VCSELs

In order to obtain single-higher-order mode operation, it is crucial to investigate the excited modes in VCSEL structures. First we will discuss the modes in normal rectangular-shaped VCSELs with large aperture. This means that no mechanism is utilized to select a certain mode, instead, the VCSEL supports many transverse modes. Such modes are analyzed in two cases: Built-in guiding, where the guiding is just due to the oxidation process that occurs for a part of the AlAs layer. The second case is including heat effects, which lead to a change of the magnitude of guiding. In addition, the modes guided in circular-shaped VCSELs are also discussed. The section is then concluded with the experimentally published work about this issue.

3.1.1 Rectangular-Shaped VCSELs

In order to investigate the modes that can be excited in normal rectangular-shaped VCSELs by the built-in guiding caused via oxidation, we introduce two different approaches. The first one is based on solving the reduced wave equation numerically and the second is an analytical solution using the Marcatili approach [33]. For solving it numerically, we assume that a rectangular core of refractive index n_1, which corresponds to the non-oxidized cross-sectional area of the cavity, is immersed in a cladding layer of refractive index $n_2 < n_1$, which is a typical approach for index-guided VCSELs, as considered in [4] and [34]. The indices n_1 and n_2 are interpreted as average quantities in the longitudinal cavity direction. The

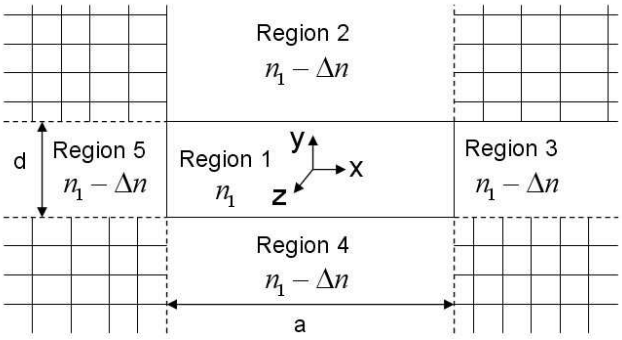

Figure 3.1: Approximation of the active aperture of a rectangular-shaped VCSEL with refractive index n_1 surrounded by a lower refractive index medium $n_2 = n_1 - \Delta n$.

index difference $\Delta n = n_1 - n_2$ for modes in this case is just due to the oxidation process. In mathematical form

$$\Delta n = \Delta n_{\text{ox}}, \tag{3.1}$$

where Δn_{ox} is due to the lateral change of the effective refractive index caused by thermal oxidation of the active aperture. This refractive index contrast is related to the cavity resonance shift $\Delta\lambda_{\text{ox}}$ as [15]

$$\Delta n = n_1 \Delta\lambda_{\text{ox}}/\lambda \ , \tag{3.2}$$

where λ is the lasing wavelength. The parameter $\Delta\lambda_{\text{ox}}$ is easily determined from two calculations with the transfer matrix method [15] as the difference in resonance wavelengths in the non-oxidized and oxidized parts of the cavity. With known indices n_1 and n_2, we then numerically solve the reduced wave equation (see (3.3) with symbol interpretation is explained after it) in the transverse plane while applying the Dirichlet boundary conditions, i.e., the electric field diminishes at the boundary of the calculation window. This solution is provided by finite element method (FEM) using partial differential equation (PDE) package in MATLAB program. In this method, the calculation window is divided into lots of triangles, each called an element and the function inside the triangle area is integrated. For more details about FEM to solve (3.3) using MATLAB program, see [31]. The result is a usually large number of guided transverse modes.

For an 8 µm × 70 µm active aperture area VCSEL with layer structure M04-050 (see App. B), the refractive index along the propagation direction is 3.3, as calculated using the transfer matrix method with the REFLEX code [32]. After oxidation of the AlAs layer, the average refractive index decreases from 3.3 to 3.298. Such difference in refractive index leads to a built-in guiding and there are 33 modes excited in this aperture using the numerical solution of this problem. The electric field of the lowest 8 modes of these solutions are depicted in Fig. 3.2. Such modes are essentially transverse electromagnetic in nature and the mode designation in this case is used according to Marcatili notations [33]. The mode designation is E_{pq}, where p is the number of extrema along the aperture length (x-direction), and q is the number of extrema along the aperture width (y-direction). In addition, each mode is either polarized in x-direction or in y-direction. The designation of the modes is shown in

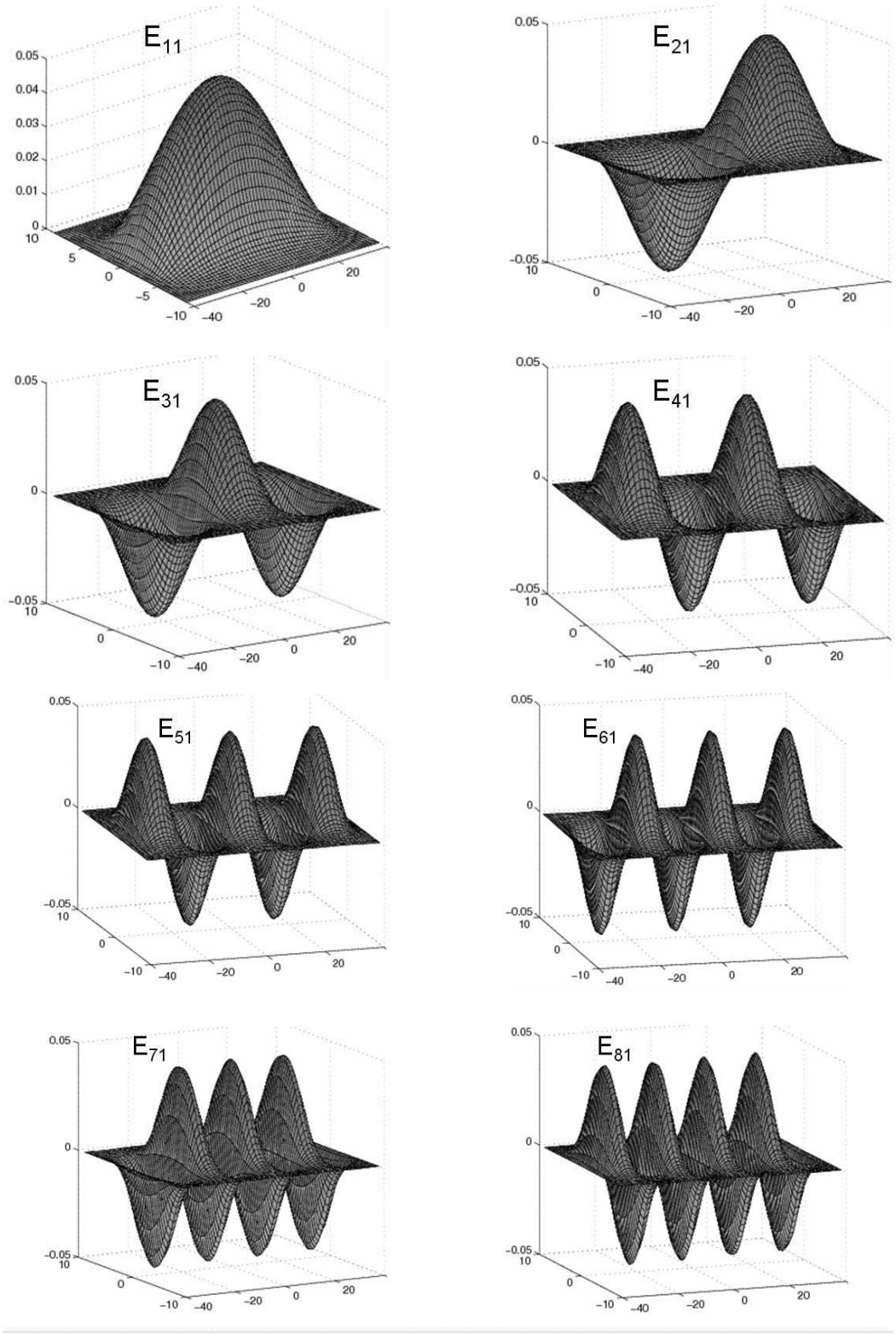

Figure 3.2: Simulated optical electric field profiles of the lowest 8 modes and their designations in a VCSEL with 8 µm × 70 µm aperture area, $\lambda = 850\,\text{nm}$, $n_1 = 3.3$, $\Delta n = 2{\times}10^{-3}$. The size of the calculation window is 18 µm × 80 µm.

the graph of Fig. 3.2. For the mode designations that are utilized in the thesis, we refer to Sect. 3.1.4.

In order to solve the problem analytically and obtain the modes, we refer to Fig. 3.1, where the active aperture of refractive index n_1 is surrounded by a lower refractive index $n_2 = n_1 - \Delta n$, and the fields in the corner regions are neglected according to the Marcatili approximation. The transverse components of the electric or magnetic fields have to satisfy the reduced wave equation

$$\partial^2\psi/\partial x^2 + \partial^2\psi/\partial y^2 + (n_m^2 k^2 - \beta^2)\psi = 0 \ , \tag{3.3}$$

where ψ is either E_x, E_y, H_x, or H_y and n_m is the refractive index in region m. The propagation constant in z-direction (perpendicular to xy-plane) is $\beta = kn_{\text{eff}}$ with the wavenumber $k = 2\pi/\lambda$ and the effective refractive index in the longitudinal direction n_{eff}. There are two types of modes that such a structure can support, namely E^y_{pq} and E^x_{pq}. E^y_{pq} modes are predominantly polarized in y-direction and consist mainly of E_y and H_x. Correspondingly, E^x_{pq} modes are mainly x-polarized with dominant E_x and H_y. The field components E_y and H_x of the modes E^y_{pq} that satisfy (3.3) in the m-th region in Fig. 3.1 are given by [35], (p. 94)

$$E_{ym}(x,y) = H_{xm}(x,y) \cdot \begin{cases} (n_1^2k^2 - k_y^2)/(2\pi\nu\epsilon_0 n_1^2\beta) & \text{for } \ m = 1, \\ (n_2^2k^2 - k_{y2}^2)/(2\pi\nu\epsilon_0 n_2^2\beta) & \text{for } \ m = 2, \\ (n_2^2k^2 - k_y^2)/(2\pi\nu\epsilon_0 n_2^2\beta) & \text{for } \ m = 3, \\ (n_2^2k^2 - k_{y2}^2)/(2\pi\nu\epsilon_0 n_2^2\beta) & \text{for } \ m = 4, \\ (n_2^2k^2 - k_y^2)/(2\pi\nu\epsilon_0 n_2^2\beta) & \text{for } \ m = 5 \end{cases} \tag{3.4}$$

and

$$H_{xm}(x,y) = \begin{cases} M_1 \cos(k_x x + \alpha)\cos(k_y y + \varphi) & \text{for } m = 1, \\ M_2 \cos(k_x x + \alpha)\exp(-\mathrm{i}k_{y2} y) & \text{for } m = 2, \\ M_3 \cos(k_y y + \varphi)\exp(-\mathrm{i}k_{x3} x) & \text{for } m = 3, \\ M_4 \cos(k_x x + \alpha)\exp(\mathrm{i}k_{y2} y) & \text{for } m = 4, \\ M_5 \cos(k_y y + \varphi)\exp(\mathrm{i}k_{x3} x + \gamma) & \text{for } m = 5, \end{cases} \tag{3.5}$$

where the refractive index and the propagation constant in region m are related by

$$k_{xm}^2 + k_{ym}^2 + \beta^2 = n_m^2 k^2 \ . \tag{3.6}$$

M_m are the field amplitudes, $2\pi\nu$ is the angular frequency, and ϵ_0 is the permittivity in free space. The angles α, φ locate the field maxima and minima in region 1, and γ equals to 0° or 90°. For matching the fields at the boundaries between region 1 and regions 2 and 4, we have assumed in (3.4), (3.5) that

$$k_{x1} = k_{x2} = k_{x4} = k_x \tag{3.7}$$

and similarly

$$k_{y1} = k_{y3} = k_{y5} = k_y \tag{3.8}$$

to match the fields between regions 1, 3, and 5. In addition, from the symmetry of the structure, one finds that

$$k_{x3} = k_{x5} \tag{3.9}$$

and

$$k_{y2} = k_{y4}. \tag{3.10}$$

Similarly, the field components E_x and H_y of E^x_{pq} modes are given by

$$E_{xm}(x,y) = \begin{cases} M_1 \cos(k_x x + \alpha)\cos(k_y y + \varphi) & \text{for } m = 1, \\ M_2 \cos(k_x x + \alpha)\exp(-\mathrm{i}k_{y2} y) & \text{for } m = 2, \\ M_3 \cos(k_y y + \varphi)\exp(-\mathrm{i}k_{x3} x) & \text{for } m = 3, \\ M_4 \cos(k_x x + \alpha)\exp(\mathrm{i}k_{y2} y) & \text{for } m = 4, \\ M_5 \cos(k_y y + \varphi)\exp(\mathrm{i}k_{x3} x + \gamma) & \text{for } m = 5 \end{cases} \tag{3.11}$$

and

$$H_{ym}(x,y) = -E_{xm}(x,y) \cdot \begin{cases} (n_1^2 k^2 - k_y^2)/(2\pi\nu\mu_0 n_1^2 \beta) & \text{for } m = 1, \\ (n_2^2 k^2 - k_{y2}^2)/(2\pi\nu\mu_0 n_2^2 \beta) & \text{for } m = 2, \\ (n_2^2 k^2 - k_y^2)/(2\pi\nu\mu_0 n_2^2 \beta) & \text{for } m = 3, \\ (n_2^2 k^2 - k_{y2}^2)/(2\pi\nu\mu_0 n_2^2 \beta) & \text{for } m = 4, \\ (n_2^2 k^2 - k_y^2)/(2\pi\nu\mu_0 n_2^2 \beta) & \text{for } m = 5. \end{cases} \tag{3.12}$$

From (3.5)–(3.11), the field in region 1 is sinusoidal and decays exponentially in the other regions, since k_{x3} and k_{y2} are imaginary quantities. In order to compare the numerical and analytical solutions, the analytical and numerical field profiles of the mode E_{81} in the plane $y = 0$ is plotted in Fig. 3.3. There is a very good agreement between the analytical solution and the numerical solution from Fig. 3.2. There is a small difference between the peak positions using both solutions at the edges of the waveguide. Moreover, the higher is the mode order, the more deviation between the analytical solution and the numerical one. A similar plot in the plane $x = 4.54\,\mu\mathrm{m}$ is shown in Fig. 3.4 for the same mode.

3.1.2 Circular-Shaped VCSELs

The convenient coordinates of circular-shaped VCSELs are cylindrical coordinates (r, φ, z). Figure 3.5 shows a model of this waveguide [4]. In the figure, the active region of refractive index n_1 is surrounded by a current blocking material of higher bandgap and lower refractive index n_2. The transverse field distributions that satisfy the Helmholtz equation can be written as [4]

$$E_t(r,\varphi) = \begin{cases} C_1 J_m(ur/r_a)\cos(m\varphi + \varphi_0) & \text{in the core with } r < r_a, \\ C_2 K_m(vr/r_a)\cos(m\varphi + \varphi_0) & \text{in the cladding with } r \geq r_a \end{cases} \tag{3.13}$$

with J_m and K_m being Bessel and Hankel functions of order m, C_1, C_2 are constants, and u and v are the normalized radial propagation constants for core and cladding, respectively.

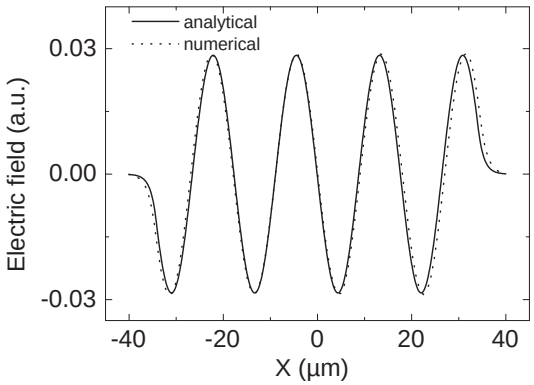

Figure 3.3: Electric field profiles of the mode E_{81} using the analytical (solid curve) and the numerical (dotted curve) solutions. The graph is plotted in the plane $y = 0$.

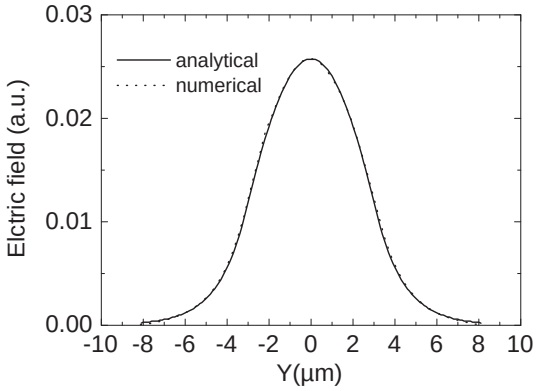

Figure 3.4: Electric field profiles of the mode E_{81} using the analytical (solid curve) and the numerical (dotted curve) solutions. The graph is plotted in the plane $x = 4.54\,\mu\text{m}$.

These propagation constants can be written as

$$u = r_a\sqrt{n_1^2k^2 - \beta^2}, \tag{3.14}$$

$$v = r_a\sqrt{\beta^2 - n_2^2k^2}. \tag{3.15}$$

In addition, the Helmholtz equation for the circular-shaped VCSELs can be solved numerically using the FEM with PDE package in MATLAB program as described in the previous subsection.

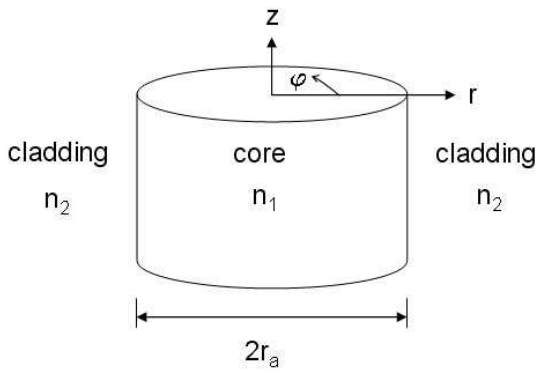

Figure 3.5: Schematic drawing of a circular waveguide with step-index profile, modeling the active layer of an index-guided VCSEL; after [4].

Figure 3.6 shows the electric field distributions for the lowest 4 transverse modes in a circular-shaped VCSEL by solving the Helmholtz equation numerically using the finite element method. The parameters used in the simulations are core diameter $2r_a = 10$ μm, $\lambda = 850$ nm, $n_1 = 3.3$, and $\Delta n = 2{\times}10^{-3}$.

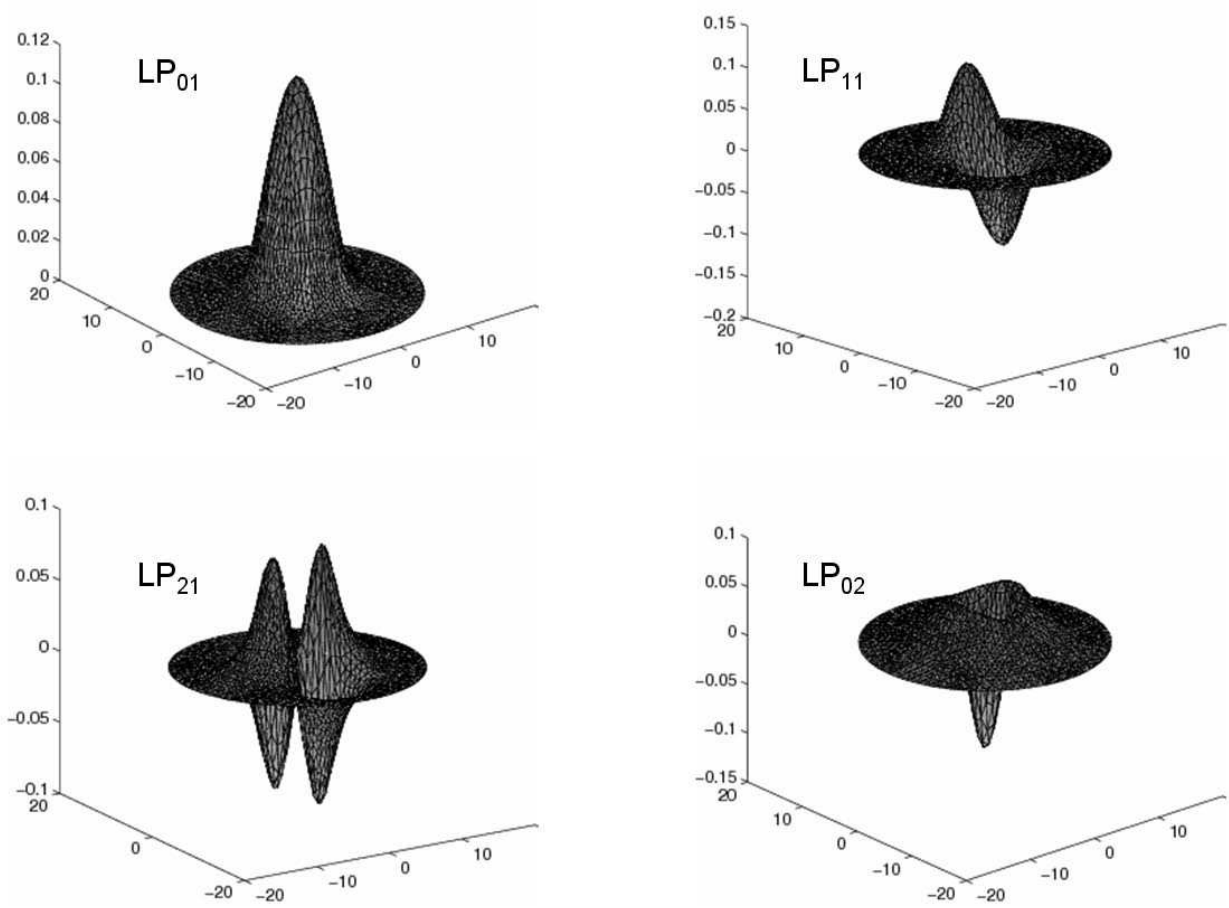

Figure 3.6: Simulated optical electric field profiles of the four lowest-order transverse modes and their designations in a circular-shaped VCSEL. The active aperture diameter is 10 μm, λ = 850 nm, $n_1 = 3.3$, $\Delta n = 2\times10^{-3}$. The simulations were done with the program MATLAB on a calculation window with 20 μm diameter.

3.1.3 The Effect of Heat on the Built-in Guiding

In the previous subsection, we described the excited modes neglecting heat effects. However, during the continuous-wave operation of VCSELs, heat will be generated due to non-radiative recombination and Joule heating in all layers. In order to include such heat effects, the refractive index contrast Δn in (3.1) is modified to include the current–refractive index dependence and temperature–refractive index dependence. In another way, (3.1) is modified to become [36]

$$\Delta n = \Delta n_{\text{ox}} + \frac{\partial n}{\partial N}\Delta N + \frac{\partial n}{\partial T}\Delta T. \tag{3.16}$$

The second term in the right-hand side in (3.16) is due to antiguiding caused by changes in carrier concentration N (with increasing the carrier concentration, the refractive index decreases). The rate of change of refractive index with carrier density for AlGaAs layer structures is $\partial n/\partial N \approx -1\times10^{-21}$ cm^3, as reported in [37].

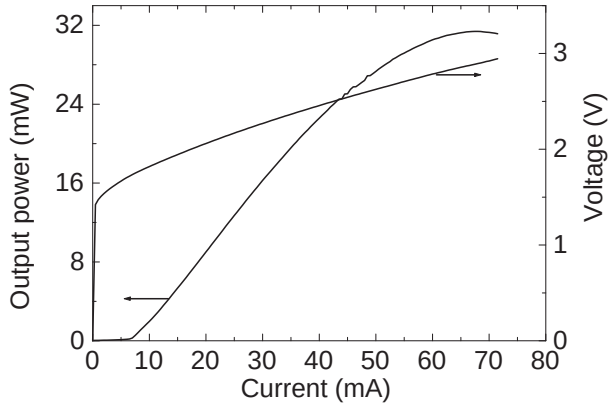

Figure 3.7: LIV characteristics of a normal rectangular-shaped VCSEL. The active aperture area is 8 µm × 70 µm .

Let us now take an experimental case: An 8 µm × 70 µm active aperture area VCSEL. The light–current–voltage (LIV) characteristics of such a device are shown in Fig. 3.7. Let us call it VCSEL 1 to refer to it. At 20 mA, the nominal current density is 3.57 kA/cm^2. The carrier density N is related to the current density j through [38]–[40]

$$j = qwN_w B_{\text{eff}} N^2, \tag{3.17}$$

where w, N_w, and B_{eff} are the thickness of the quantum well, the number of quantum wells, and the effective recombination coefficient, respectively. Bimolecular recombination and equal carrier concentrations are assumed in (3.17). The measured effective recombination coefficient for AlGaAs material is 0.9×10^{-10} cm^3/s, as reported in [41]. Thus, the corresponding nominal carrier density by substituting in (3.17) is 1×10^{19} cm^{-3}, where w=8 nm and N_w=3. This means that the contribution of antiguiding caused by increase of the carrier density is –0.01 in the active region. However, this value has to be weighted throughout the layer structure. This is achieved by multiplying it in the axial confinement factor (see Sect. 2.4). The weighted antiguiding effect is then $-0.01 \times 0.0225 = -2.3 \times 10^{-4}$.

The third term in the right-hand side in (3.16) is due to the thermal lensing effect. The rise in the junction temperature is given by [19]

$$\Delta T = \frac{P_{\text{IV}} - P_{\text{out}}}{2\pi d \sigma_{\text{T}}} \ , \tag{3.18}$$

where P_{IV} is the input electrical power in the device and P_{out} is the emitted laser power, σ_{T} is the thermal conductivity, and d is the thickness of the sheet carrying away heat. In (3.18), the heat is assumed to be distributed within a sheet of thickness $d \approx 5$ µm. The thermal conductivity σ_{T} of GaAs is 0.44 (W/cm K). At 20 mA, the temperature contrast from the center of the device to the edge using (3.18) and the LIV curves in Fig. 3.7 is 22.5 K. The variation of refractive index with temperature depends on the Al-content [42]. It is set to be 2×10^{-4} K^{-1}. This leads to 4.5×10^{-3} step index contrast obtained from the contribution of thermal lensing. The net index contrast is then 6.3×10^{-3} with the heat and current effects taken into account. This means the index contrast is increased a factor of 3 compared

to the built-in guiding at this current. The profile of the refractive index in the transverse coordinate of the active aperture under this large injection tends to focus the laser beam in the center. In other words, in response to this heat effect under high pumping, the laser medium acts like a lens. Under this condition of high pumping level, one can write the refractive index as a function of the transverse coordinates $n(r)$ in terms of the refractive index at the center $n(r = 0)$ as follows [43]

$$n(r) = n(r = 0) - \frac{1}{2}Ar^2 \ , \tag{3.19}$$

where A is a constant and $r^2 = x^2 + y^2$. This means the refractive index varies quadratically with the distance r from the optical axis. Such quadratic dependence was also reported in gain-guided VCSELs [44]. Such a medium is called the complex square law medium, and the electric field of the transverse modes as a function of x and y is described by Hermite-Gaussian functions [45]–[47] of the form

$$E_{gh}(x, y) = H_g\left(\frac{\sqrt{2}x}{\omega}\right) H_h\left(\frac{\sqrt{2}y}{\omega}\right) \exp\left(\frac{-r^2}{\omega^2}\right) \ , \tag{3.20}$$

where g, h are the transverse mode numbers and equal to the number of zeros in x- and y-directions, respectively. H_g and H_h are Hermite polynomials of order g and h, respectively, and ω represents the spot size. The first four lowest-order modes in the plane $y = 0$ are plotted in Fig. 3.8 using Hermite-Gaussian functions with $\omega = 15\,\mu\text{m}$.

3.1.4 Mode Designations in VCSELs

The following mode designations are utilized throughout the thesis:

- When the modes are excited in circular-shaped VCSELs, the modes are designated as LP_{mn}. The indices m and n are the azimuthal and radial transverse mode numbers, respectively. The LP designation in this case is utilized to be consistent with the literature on optical fibers.
- When the modes are excited in rectangular-shaped VCSELs, the designation E_{pq} is applied. The positive integer numbers p and q represent the number of peaks in x and y directions, respectively. The designation E_{pq} is utilized to be consistent with Marcatili designation [33]. For the special case when p is larger than or equal to 10, a space between p and q is utilized to separate p from q.

3.1.5 Experimentally Reported VCSEL Modes

In this subsection, we will discuss the intensity distributions of the VCSEL transverse modes as reported experimentally using high-resolution instruments. In oxide-confined VCSELs as well as ion-implanted VCSELs, Hermite–Gaussian profiles have been reported. Degen et al.

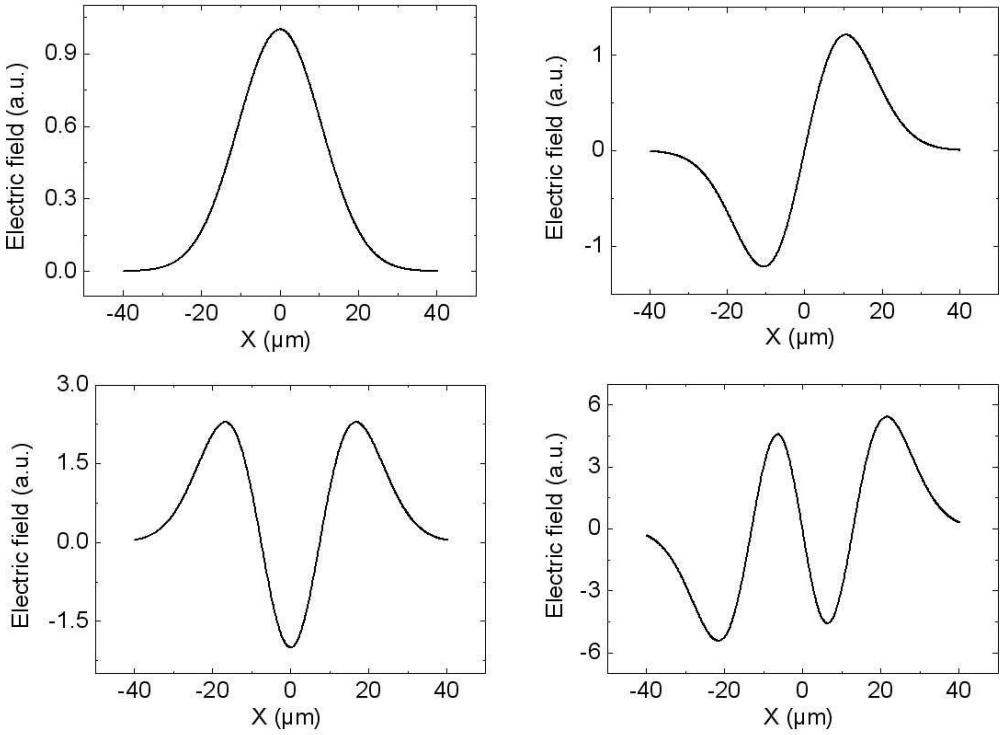

Figure 3.8: Electric field profiles of the four lowest-order modes in the plane $y = 0$ using Hermite–Gaussian functions 3.20. The parameter ω equals to 15 µm.

[49] reported experimentally that oxide-confined VCSELs exhibit a wide variety of emission patterns from low-order Hermite–Gaussian modes to high-order Laguerre–Gaussian modes. From his measurements he concluded that inhomogeneities in the pump profile caused by current spreading dominate the transverse emission properties. For ion-implantation VCSELs, Chang-Hasnain et al. [48] performed some near-field measurements and reported that the excited modes are Hermite–Gaussian modes. For large-aperture ion-implanted VCSELs operated well above laser threshold Li et al. [50] concluded from the measurements that both Hermite–Gaussian and Laguerre–Gaussian modes were excited. In addition, superpositions of Hermite–Gaussian modes of first order modes have been already reported [51], [48].

In our case of the normal rectangular-shaped VCSELs, the circular symmetry is broken. This means Laguerre–Gaussian modes can not be excited in rectangular-shaped VCSELs, and only Hermite–Gaussian mode are to be expected. Figures 3.9 and 3.10 show the near-field intensity profiles of some excited higher-order transverse modes (for more details about the setup, see Sect. 6.1.3). The active aperture areas and the currents at which measurements were done are indicated in the figure captions. The devices are normal VCSELs, where no mechanisms are utilized to select a certain transverse mode. This means that the devices operate in the multi-transverse mode regime. Mode designations are written in the graphs. It is worth to mention that complicated interactions of effects are occurring, which affect the emitted near-field intensity. These effects include pumping inhomogeneity throughout the active aperture and temperature gradient from the center of the aperture to its edge. While

the current density increases from the center of the aperture to its edge, the temperature decreases. This will affect the distribution of the refractive index throughout the aperture. According to [49], in oxide-confined VCSELs inhomogeneities in the pump profile caused by current spreading dominate the transverse emission properties. As the active aperture area increases from Fig. 3.9 to 3.10, the inhomogeneity in pumping increases. The result is that the excited modes in Fig. 3.10 are less homogeneous compared to those in Fig. 3.9.

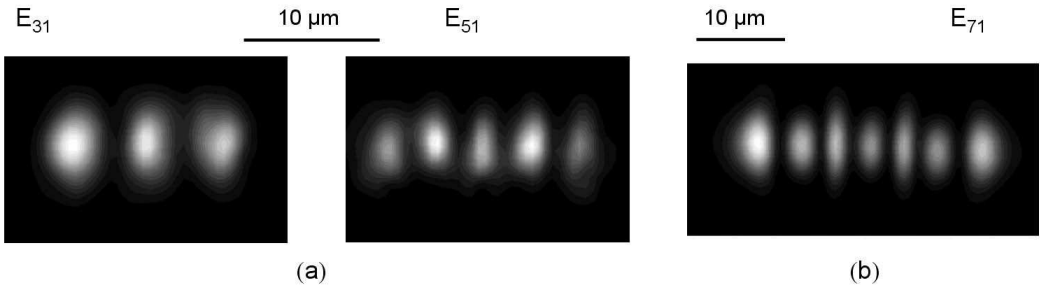

Figure 3.9: Near-field intensity profiles of some transverse modes in a normal rectangular-shaped VCSEL with (a) 5 µm × 15 µm and (b) 6 µm × 30 µm aperture areas. The measurements were done at (a) 5 mA and (b) 10 mA.

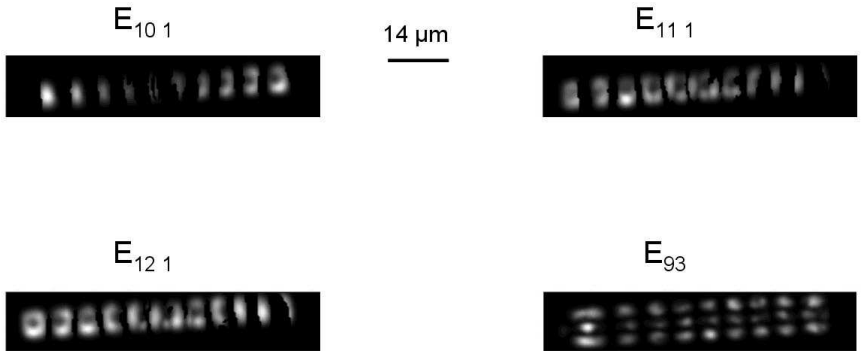

Figure 3.10: Near-field intensity profiles of some transverse modes in a normal rectangular-shaped VCSEL with 8 µm × 70 µm aperture area. The measurements were done at 20 mA, and the scanned area in the near-field is 14 µm × 90 µm.

3.2 BV Diagram

In this section we will discuss the BV diagram generated from the built-in guiding of normal rectangular-shaped VCSELs caused by oxidation of a part of the AlAs layer. The corresponding BV diagrams of such a structure obtained from the analytical and the numerical solutions for an aspect ratio of 3 are shown in Fig. 3.11. The frequency parameter V and the

phase parameter B are defined as

$$V = \frac{2\pi}{\lambda} d \sqrt{n_1^2 - n_2^2} \,, \tag{3.21}$$

$$B = \frac{n_{\text{eff}}^2 - n_2^2}{n_1^2 - n_2^2} \,, \tag{3.22}$$

where d is the aperture width. From Fig. 3.11 it is seen that even the fundamental mode E_{11} has a cut-off frequency. Furthermore, the cut-off frequencies of the numerical solutions are smaller than those of the analytical solutions. This is attributed to neglecting the fields in the corners for the analytical solutions. In addition, the phase parameters of the numerical solutions are higher than those of analytical solutions at the same value of the frequency parameter. As the aspect ratio a/d (see Fig. 3.1) increases from 3 to 10, the separation between modes on the V-axis decreases, as shown in Fig. 3.12. In addition, the order of appearance of the modes changes as the aspect ratio changes. It is worth to mention that the BV diagrams plotted in Figs. 3.11 and 3.12 are not universal but changes with the layer structure, i.e., depends on n_1 and n_2. The BV diagram for circular aperture VCSELs with the same structure is displayed in Fig. 3.13. In this case, the parameter d in (3.21) is identified with the *radius* of the oxide aperture to be consistent with the literature on optical fiber theory, i.e., $d = r_a$ from Fig. 3.5. The number of guided modes is low due to the fact that the aspect ratio is equal to one. It is plotted in Fig. 3.13 (right) as a function of the aperture area. For counting the modes in Fig. 3.13 (right) both cos- and sin-distributions are counted, but each mode is assumed to have only one polarization.

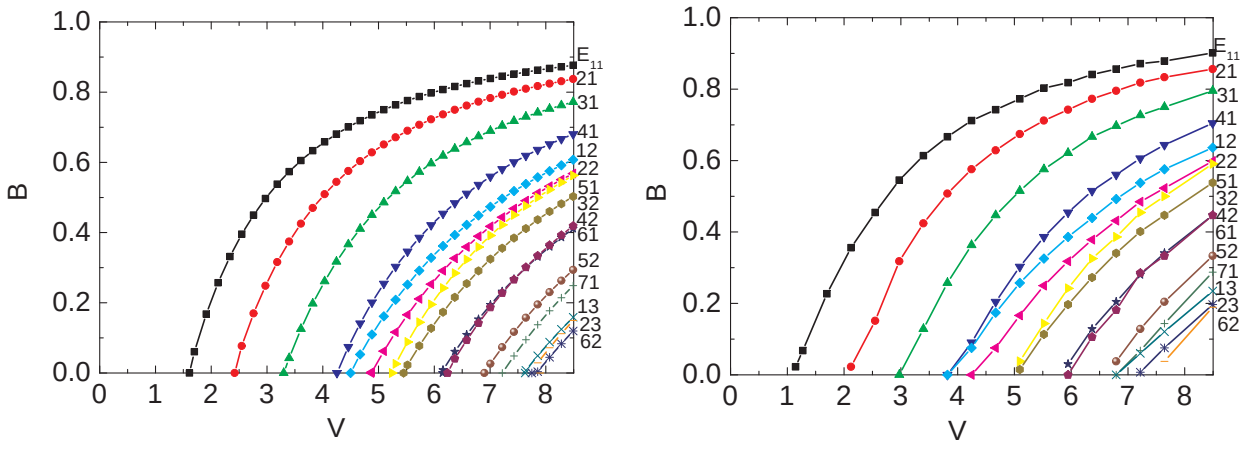

Figure 3.11: BV diagram of rectangular-shaped VCSELs obtained from analytical solutions (left) and numerical solutions (right). The aspect ratio is 3.

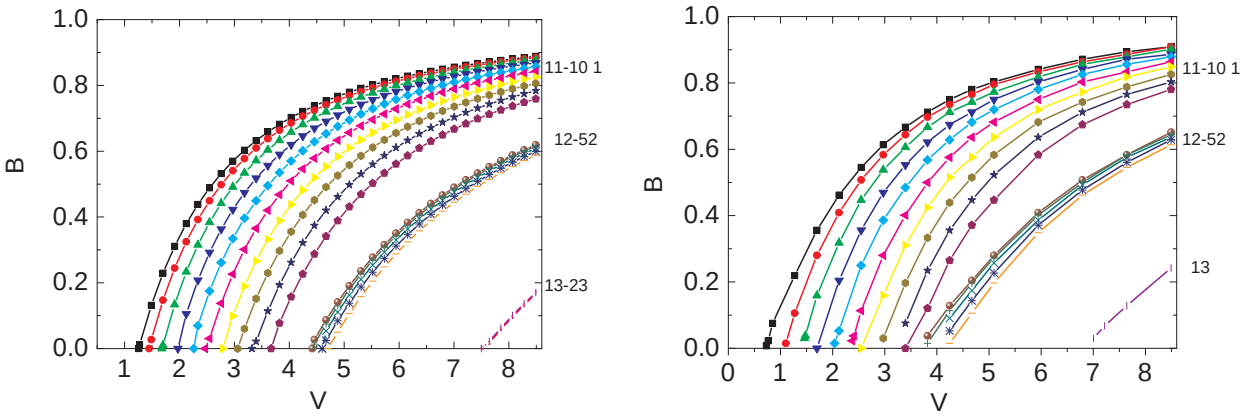

Figure 3.12: BV diagram equivalent to Fig.3.11 for an aspect ratio of 10.

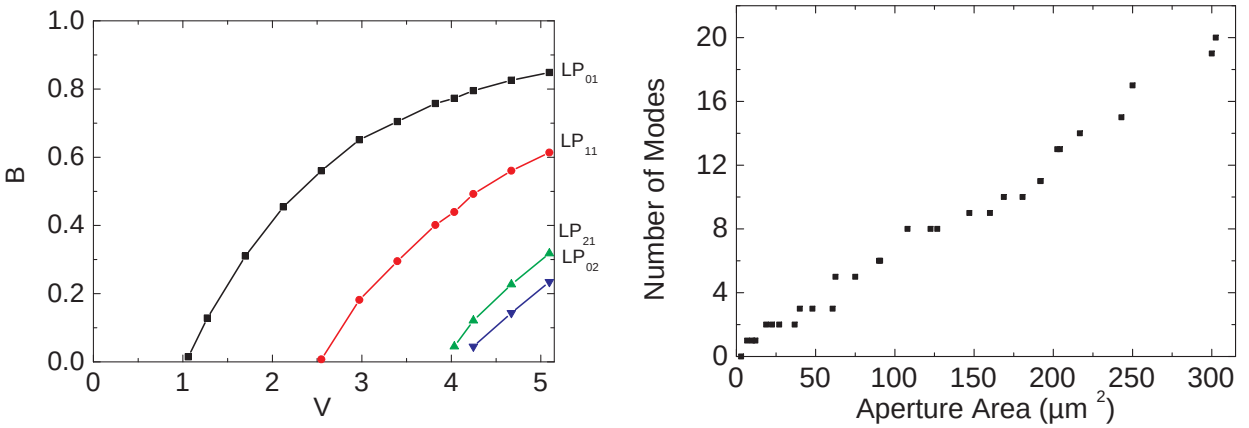

Figure 3.13: Numerically calculated BV diagram of circular-shaped VCSELs (left) and the number of modes as a function of the aperture area (right).

3.3 Propagation of Higher-Order Transverse Modes in Free Space

In this section we wish to discuss beam parameters of higher-order transverse modes as they propagate in a lossless homogeneous medium. The mode propagation of rectangular-shaped and circular-shaped VCSELs will be discussed.

3.3.1 Hermite–Gaussian Field

When the active aperture of a VCSEL is of rectangular shape, cartesian coordinates are convenient to describe its modes. Since these VCSELs break the circular symmetry, the beam emitted from such VCSELs has two specific spot sizes: One is along the aperture length and is termed ω_a, and the other is along the aperture width and is termed ω_d. The corresponding radii of curvature of these spots are given by [52]

$$R_a = z\left[1+\left(\frac{\pi\omega_a^2}{\lambda z}\right)^2\right], \tag{3.23}$$

$$R_d = z\left[1+\left(\frac{\pi\omega_d^2}{\lambda z}\right)^2\right], \tag{3.24}$$

where z indicates that the propagation occurs in z-direction. As a practical definition of the spot size for a higher-order mode, Luxon and Parker [53] defined the spot size to be half the distance from the centers of the outer intensity peaks.

When the modes excited in rectangular-shaped VCSELs are described by Hermite–Gaussian distributions, the intensity of such a beam is given by [54]

$$I_{gh}(x,y,z) = I_0\frac{\sigma_x(0)\sigma_y(0)}{\sigma_x(z)\sigma_y(z)}H_g^2\left(\frac{x}{\sigma_x(z)}\right)H_h^2\left(\frac{y}{\sigma_y(z)}\right)\exp\left(-\frac{r^2}{\sigma_x(z)\sigma_y(z)}\right) \tag{3.25}$$

with I_0 as the intensity in the plane $z = 0$. The parameter σ is related to ω through

$$\sigma_s = \frac{\omega_s}{\sqrt{2}}. \tag{3.26}$$

σ_s along the x-and y-axes in any plane of constant z is defined as

$$\sigma_s(z) = \sigma_s(0)\left(1+\frac{z^2}{z_0^2(s)}\right)^{1/2}, \tag{3.27}$$

in which s represents x or y, and

$$z_0(s) = \frac{2\pi}{\lambda}\sigma_s^2(0) = \frac{\pi}{\lambda}\omega_s^2(0) \tag{3.28}$$

is the Rayleigh range of the fundamental mode. Equations (3.23) and (3.24) suggest that the beam emitted from asymmetric apertures has two different Rayleigh ranges (defined from (3.28)): One characterizes the length of the aperture and the other characterizes the width of the aperture. The meaning of $\sigma_s(z)$ for the fundamental mode is $1/e$ half-width for the beam intensity along the x or y axis in any plane of constant z [54]. However, for the higher-order beams $\sigma_s(z)$ has no such simple meaning. Higher-order beams do not form simple spots of light but form more complicated patterns (see Sect. 3.1.5). For this reason, Carter [54] suggested the square root of twice the variance as the measure of the dimensions of the illuminated area in the plane of constant z along the s-axis for the higher-order mode, i.e.,

$$\sigma_s(z)l = \left(\frac{2\int\int_{-\infty}^{\infty} s^2 I_{gh}(x,y,z)dxdy}{\int\int_{-\infty}^{\infty} I_{gh}(x,y,z)dxdy}\right)^{1/2}, \tag{3.29}$$

in which l represents g or h. All the extrema of the illuminated area are contained in a rectangle of area $2\sigma_x(z)\times 2\sigma_y(z)$, which gives a meaning for $\sigma_s(z)$. By substituting from (3.25) into (3.29) and performing the integration we obtain

$$\sigma_s(z)l = \sigma_s(z)(2l+1)^{1/2}. \tag{3.30}$$

and using (3.27) the spot size of mode order l in the plane of constant z along the s-axis is given by

$$\sigma_s(z)l = \sigma_s(0)(2l+1)^{1/2}\left(1+\frac{z^2}{z_0^2(s)}\right)^{1/2}. \tag{3.31}$$

Luxon et al. [55] modified the last expression by including the quantity k_l of the higher-order mode in the expression, i.e.,

$$\sigma_s(z)l = \sigma_s(0)(2l+1)^{1/2}k_l\left(1+\frac{z^2}{z_0^2(s)}\right)^{1/2}, \tag{3.32}$$

with

$$k_l = 1 + 0.73l^{-0.78}, \tag{3.33}$$

This quantity is related to the correction factor C_l of the higher-order mode through [56]

$$C_l = \frac{l+0.5}{k_l^2}, \tag{3.34}$$

with C_l accounts for the deviation of the mode from the ideally theoretical Gaussian beam. For the fundamental mode it is 1 and it increases with increasing the mode order. Furthermore, the Rayleigh range of the higher-order mode $z_0(s)_l$ is related to spot size of the fundamental mode $\omega_0(s)$ by [55]

$$z_0(s)_l = \frac{\pi\omega_0^2(s)}{\lambda}\frac{k_l^2}{2l+1}. \tag{3.35}$$

In addition, the transverse mode spacing in a Fabry-Pérot cavity with plane-plane mirrors is given by [17]

$$\Delta\nu = \frac{c}{2\pi n z_0(s)} = \frac{ck_l^2}{2\pi n(2l+1)z_0(s)_l}, \tag{3.36}$$

where c and n are the velocity of light in vacuum and the refractive index of the mode in the medium. In terms of the wavelength separation between two neighboring transverse modes $\Delta\lambda$ (3.36) becomes

$$\Delta\lambda = \frac{\lambda^2}{2\pi n z_0(s)} = \frac{k_l^2\lambda^2}{2\pi n(2l+1)z_0(s)_l}. \tag{3.37}$$

By measuring $\Delta\lambda$, the Rayleigh range, and thus the spot size can be estimated, see Sect. 6.1.3.

3.3.2 Laguerre–Gaussian Field

When the distribution of the refractive index is parabolic, the analytical solutions of the Helmholtz equation in cylindrical coordinates are found to be Laguerre–Gaussian distributions. The intensity profiles of such modes are described by [57]

$$I_{mn}(r,\varphi,z) = K(z)\left(\frac{2r^2}{\omega^2}\right)^m\left[L_n^m\left(\frac{2r^2}{\omega^2}\right)\right]^2\exp(-2r^2/\omega^2)\begin{cases}\sin^2 m\varphi,\\ \cos^2 m\varphi,\end{cases} \tag{3.38}$$

where L_n^m represent the generalized Laguerre polynomial and K is a function of z which does not affect the analysis. The indices m and n represents the azimuthal and radial transverse mode numbers, respectively. Similar to (3.29), the spot size in the circular aperture of the higher-order mode is defined as

$$\sigma_r(z)mn = \left(\frac{2\int_0^{2\pi}\int_0^{\infty} r^2 I_{mn}(r,\varphi,z) r dr d\varphi}{\int_0^{2\pi}\int_0^{\infty} I_{mn}(r,\varphi,z) r dr d\varphi} \right)^{1/2}, \tag{3.39}$$

By performing the integration, one obtains a relation between the spot size of any higher-order mode and that of the lowest-order mode as

$$\sigma_r(z)mn = \omega_0(2m+n+1)^{1/2}\left(1+\frac{z^2}{z_0^2}\right)^{1/2} \tag{3.40}$$

with $z_0 = \pi\omega_0^2/\lambda$ as the Rayleigh range.

3.4 Near-Field of a Single-Higher-Order Transverse Mode VCSEL

The exact calculations of the near-field intensity profiles of a single-higher-order transverse mode are rather complicated and are beyond the scope of this experimentally oriented thesis. In these calculations one needs to know the heat sources (mainly current-induced) and then solve the heat equation to know the temperature distribution in the transverse coordinates. Moreover, the current distribution in the transverse coordinates is needed to be calculated. After performing these calculations, the laser field has to be coupled with these effects [58], [59].

However, we will try an approach to deduce the near-field intensity. In this approach we will use the inverse Fourier transform of the measured far-field to obtain the near-field. Then we will compare it to the measured near-field intensity profile. The far-field intensity of a single-higher-order transverse mode, $I(\theta_x)$ (see Sect. 4.5 for more details) is related to the near-field $E(x)$ through [60]

$$I(\theta_x)/\cos^2(\theta_x) \propto \left| \int_{-\infty}^{\infty} E(x)\exp(ik\sin(\theta_x)x)dx \right|^2 \tag{3.41}$$

for the x-direction. In contrast to [60], a term $\cos^{-2}(\theta_x)$ on the left-hand side of (3.41) has been omitted since during the experiment the photodetector is always oriented perpendicular to the measurement direction (see Fig. 6.12). An equivalent equation applies for y-direction. Moreover, for a coherent laser source the angle of divergence is small and the paraxial approximation can be applied. In the paraxial approximation, the angle between the wave vector and optical axis is small such that $\sin(\theta_x) \approx \theta_x$. In our case the main side-lobe occurs at $\approx 3^\circ$ (see Fig. 4.23). With these considerations, (3.41) becomes

$$I(\theta_x) \propto \left| \int_{-\infty}^{\infty} E(x) \exp(ik\theta_x x) dx \right|^2 . \tag{3.42}$$

This means the near-field intensity can be obtained by an inverse Fourier transform. Hence, the near-field intensity is

$$I(x) \propto \left| \int_{-\infty}^{\infty} E(\theta_x) \exp(-ik\theta_x x) d\theta_x \right|^2 . \tag{3.43}$$

The field $E(\theta_x)$ is obtained by taking the positive values of the measured $I(\theta_x)$. In addition, the phase of the field is assumed to be constant across the semi-circle through which the photodetector moves. The measured near-field intensity profiles of an 8-spot surface-etched 6.3 µm × 68.3 µm single-mode VCSEL as well as the calculated one using this approach and the analytical solution (3.11) are depicted in Fig. 3.14 with the solid curve, the dash-dotted curve, and the dashed curve, respectively. The current at which the near-field intensity was measured is 30 mA. The positions at which the measured intensity peaks occur are shifted from the calculated ones (using (3.43)) due to heat effects. In addition, the emitted laser intensities from the 8 spots are not equal due to the pumping inhomogeneity caused by current spreading in the large active aperture.

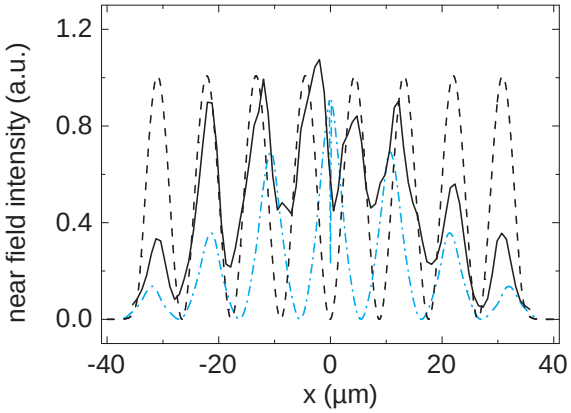

Figure 3.14: Near-field intensity profiles in the horizontal direction of an 8-spot surface-etched rectangular-shaped VCSEL with 6 µm relief diameter of each spot and 9 µm pitch. Solid, dashed and dash-dotted curves are corresponding to measurement, calculation using (3.11), and calculation using (3.43), respectively.

Chapter 4

Mode Selection Using Surface Etching in Rectangular-Shaped VCSELs

In this chapter, we introduce a theoretical and an experimental analysis of VCSELs with rectangular-shaped apertures that allow operation on a single higher-order transverse mode. The aperture has a width d and a length a with $a > d$ according to Fig. 3.1. The mode selection is based on a spatial variation of the threshold gain by adding an antiphase layer with an etched relief pattern. This pattern is chosen to select a higher-order transverse mode by reducing the threshold gain of the desired mode and increasing the threshold gain of other modes. The main factors that control the selected mode such as the threshold gain, the confinement factor, and the phase parameter are calculated as a function of the active aperture, aiming to achieve single-higher-order transverse mode emission. For a given aspect ratio a/d of a rectangular oxide aperture, the threshold gain difference between the selected and neighboring modes is maximized via the relief diameter and the size of the aperture. By this mechanism, mode selection was successfully achieved in this work. Attractive applications for such devices are found in optical manipulation of micro-particles such as sorting and separation.

4.1 Introduction

VCSELs have attracted considerable interest due to their low divergence and nonastigmatic beam characteristics as well as low-cost manufacturing, testing and packaging. Besides, the ability of single-mode operation in longitudinal and transverse directions is one of the most distinguished advantages of these lasers. Single-mode VCSELs offer different applications ranging from data transmission to optical sensing [21], [61]. While single-longitudinal mode operation is inherent to the short cavity design of VCSELs, the transverse mode behavior depends on the size of the active aperture as well as the layer structure. In order to select the fundamental mode, the active aperture of the VCSEL has to be small. This deteriorates the performance of the device by increasing both the thermal resistance and the ohmic series

resistance. Moreover, the device lifetime is decreased and mass production is made more difficult due to tight aperture tolerances.

For this purpose, we report on a large-area single-higher-order mode rectangular-shaped VCSEL. The technique utilized in mode selection in this device is shallow surface etching, where multi-spot surface etching is "tailored" to select a certain transverse mode. The large size of this VCSEL offers record-low series resistances as well as record-high output powers. In addition, operation on a higher-order transverse mode is of interest in multiple optical trapping [62] and potentially in optical data storage [63].

4.2 Description of the Device

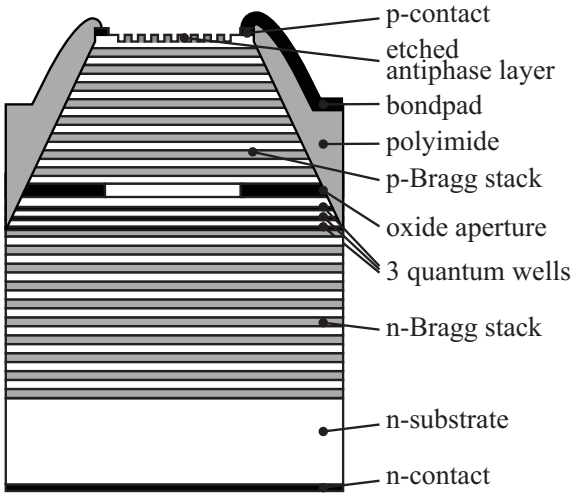

Figure 4.1: Schematic drawing of a multi-spot shallow surface-etched rectangular-shaped VCSEL.

A schematic drawing of a multi-spot shallow surface-etched rectangular-shaped VCSEL is depicted in Fig. 4.1. The layer structure consists of 23 C-doped $Al_{0.2}Ga_{0.8}As/Al_{0.9}Ga_{0.1}As$ p-DBR pairs as top mirror (plus the topmost GaAs quarter-wave layer) and 38.5 Si-doped $Al_{0.2}Ga_{0.8}As/Al_{0.9}Ga_{0.1}As$ DBR pairs as the bottom mirror. The DBR are graded in composition and doping concentration for minimizing the free-carrier absorption and decreasing the electrical resistance. The active region composed of three 7.9 nm thick GaAs quantum wells (QWs) separated by 9.9 nm thick $Al_{0.27}Ga_{0.73}As$ barriers is positioned in an optical cavity with a thickness of one material wavelength. The laser emission wavelength using these materials together with the cavity design is in the vicinity of 850 nm. A 32 nm thick AlAs oxidation layer is placed in the first Bragg pair above the QWs as shown in Fig. 4.1. The function of this layer is twofold: When a part of it is oxidized to form the active aperture, not only the excitation current is confined but also optical guiding of the laser radiation occurs. The shallow surface etching technique in the quarter-wave layer is utilized to allow operation on a certain higher-order transverse mode. A top-view micrograph of a fully-processed

multi-spot shallow surface etched rectangular-shaped VCSEL is shown in Fig. 4.2. For this device, 8-spot surface etching was applied to enforce lasing of the E_{81} mode with eight peaks along the aperture length and one peak along the aperture width. Devices that do not employ multi-spot surface etching, but in which just the antiphase layer is totally removed, are termed standard or normal rectangular-shaped VCSELs. A micrograph demonstrating such a standard VCSEL is shown in Fig. 4.3.

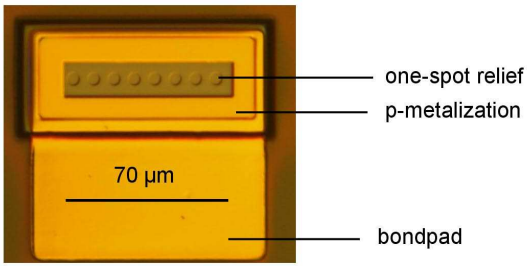

Figure 4.2: Micrograph showing the top view of a fully-processed 8-spot surface-etched rectangular-shaped VCSEL.

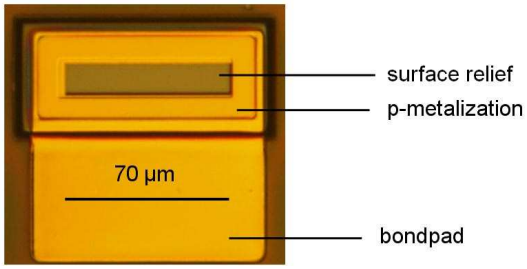

Figure 4.3: Micrograph showing the top view of a fully-processed standard rectangular-shaped VCSEL.

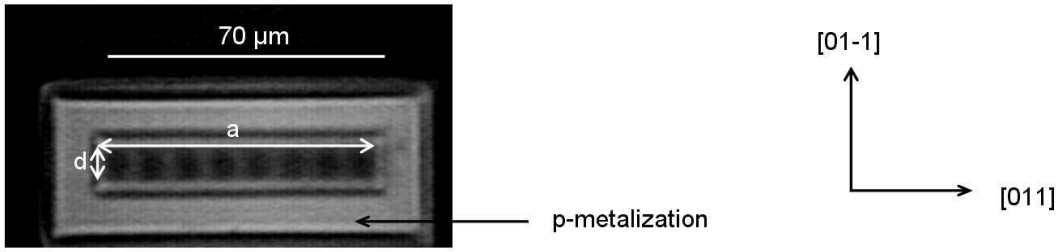

Figure 4.4: Micrograph showing the active aperture of width d and length a in case of an 8-spot surface-etched rectangular-shaped VCSEL (left). The micrograph is recorded with an infrared microscope. The aperture width and length are oriented parallel to the crystal directions $[01\bar{1}]$ and [011], respectively (right).

There are two main differences between a multi-spot shallow surface-etched rectangular-shaped VCSEL and a normal circular-mesa VCSEL. Firstly, concerning the layer structure, a quarter-wavelength antiphase layer is added in order to induce a decrease in top mirror reflectivity. This layer is then selectively removed such that the threshold gain inside the shallow etching spot is minimum and outside it is maximum. With this way the threshold gain of a certain mode is minimized, and that of all other modes is maximized. This will provide selection for a certain higher-order transverse mode. This selective etching is carried out by means of wet-chemical etching. The second point concerns the shape of the mesa and thus of the oxide aperture. It is no longer of circular shape, instead it is rectangular, where one side of the rectangle is much longer than the other. A micrograph showing the VCSEL mesa and its active aperture with a multi-spot etched surface is displayed in Fig. 4.4 (left). The aperture width and length are oriented parallel to the crystal directions $[01\bar{1}]$ and [011], respectively, as indicated in Fig. 4.4 (right).

4.3 Analysis and Experimental Results

In order to select the oscillation of a certain higher-order transverse mode in a multi-spot shallow surface-etched rectangular-shaped VCSEL, for example the mode E_{81} , a linear pattern with 8 circular spots each having 4 µm diameter is etched through the entire antiphase layer. We refer to this pattern as pattern 1. The pattern is chosen such that the centers of the spots coincide with the positions of the peaks of the intensity profile. Here we assume that the etching does not perturb the field. The selection of the lasing mode in such a structure depends on the three-dimensional confinement factors Γ of the modes and the threshold gains g_{th}, where

$$\Gamma = \Gamma_z \Gamma_{xy,p} \tag{4.1}$$

with Γ_z representing the axial confinement factor and $\Gamma_{xy,p}$ representing the lateral confinement factor of the etching pattern. For more details about the axial confinement factor, see Sect. 2.4. In analogy to fiber theory, $\Gamma_{xy,p}$ is defined as [4]

$$\Gamma_{xy,p} = \frac{P_{\mathrm{p}}}{P_{\mathrm{t}}}, \tag{4.2}$$

where P_{p} and P_{t} are the power in the area of the etch pattern and the total power of the mode, respectively. Figure 4.5 (left) demonstrates the overlapping between the mode E_{81} and pattern 1. According to our calculations of the lateral confinement factors of the modes that can be excited in an active aperture area of 8 µm × 70 µm, the most competitive mode to the E_{81} mode is the $E_{12\,1}$ mode. Figure 4.5 (right) shows the overlapping between the $E_{12\,1}$ mode and pattern 1 over the same aperture area. It is worth to mention that once the aperture dimensions or the pattern changes, the most competitive mode to E_{81} can change. For instance, at an aperture area of 6 µm × 48 µm, and when pattern 1 is applied, the most competitive mode to the E_{81} mode is the E_{71} mode. On the other hand, with an aperture area of 7 µm × 56 µm and pattern 1, the most competitive mode to the E_{81} mode becomes the E_{61} mode.

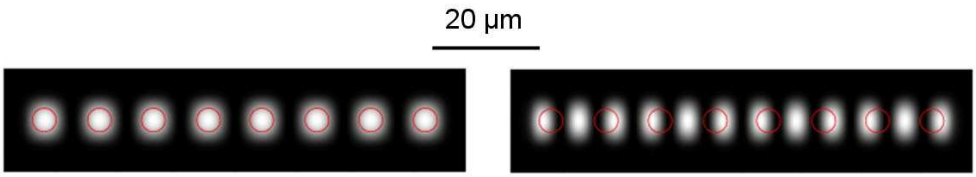

Figure 4.5: Simulated intensity profiles of the modes E_{81} (left) and $E_{12\,1}$ (right) for an active aperture area of 8 µm × 70 µm. Pattern 1 is indicated in the graph with black circles.

The three-dimensional confinement factor Γ as a function of the aperture width for both the E_{81} mode and its competitive mode E_c is shown in Fig. 4.6. With increasing the aperture width, the confinement factor decreases. Further, with increasing the aspect ratio, the confinement factor decreases. The corresponding threshold gain of the mode depends on

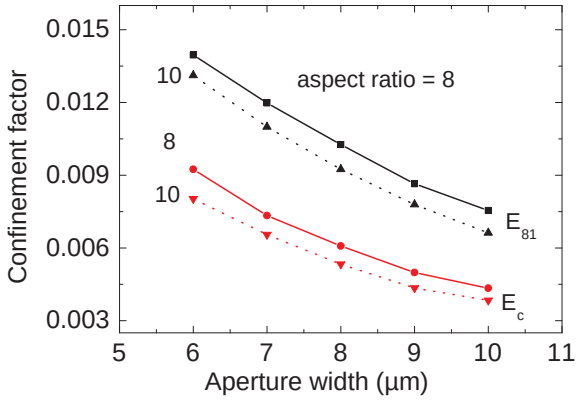

Figure 4.6: Dependence of the confinement factor Γ of the modes E_{81} and E_c on the aperture width d for structure 1 with pattern 1. Aspect ratios a/d are 8 or 10.

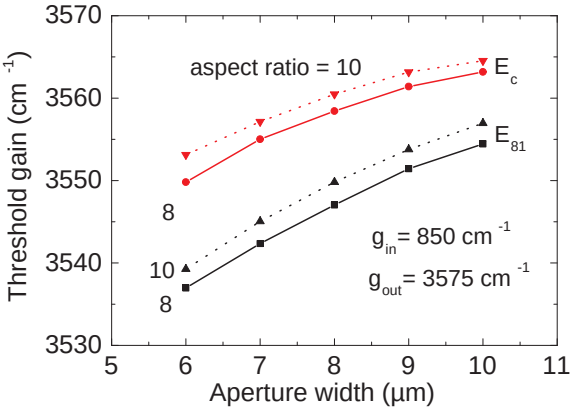

Figure 4.7: Dependence of the threshold gain g_{th} of the modes E_{81} and E_c on the aperture width d for structure 1 with pattern 1. Aspect ratios a/d are 8 or 10.

Γ as well as on the threshold gains inside and outside the spot area, namely g_{in} and g_{out}, respectively, where $g_{\text{in}} < g_{\text{out}}$. These threshold gains are calculated for the given structure using the transfer matrix method [15]. The threshold gain of the particular mode is then given by

$$g_{\text{th}} = \Gamma g_{\text{in}} + (1 - \Gamma) g_{\text{out}} \ . \tag{4.3}$$

The threshold gain of a certain mode to be selected increases with increasing the aperture width as well as with increasing the aspect ratio. Figure 4.7 shows such dependence for the modes E_{81} (to be selected) and E_c (the competitive one) for $g_{\text{in}} = 850\,\text{cm}^{-1}$ and $g_{\text{out}} = 3575\,\text{cm}^{-1}$ (let us refer to this as structure 1).

An important parameter to assess the degree of selection of the desired mode is the difference between its threshold gain $g_{\text{th,s}}$ and that of the most competitive mode $g_{\text{th,c}}$. With the confinement factors of the selected and the competitive mode, Γ_{s} and Γ_{c}, respectively, it is written as

$$\Delta g_{\text{th}} = g_{\text{th,c}} - g_{\text{th,s}} = (\Gamma_{\text{s}} - \Gamma_{\text{c}}) \cdot (g_{\text{out}} - g_{\text{in}}) \ . \tag{4.4}$$

The threshold gain difference for such structures tends to decrease as the aperture increases. This is shown in Fig. 4.8 for aspect ratios of 10 and 8 for structure 1 with pattern 1. Both the LIV characteristics and the spectrum emitted from a laser with structure 1 and pattern 1 are shown in Fig. 4.9 and Fig. 4.10, respectively. The active aperture of the device is $8\,\mu\text{m} \times 70\,\mu\text{m}$. At 25 mA, the VCSEL shows multi-wavelength operation. Hence, structure 1 with pattern 1 is not suitable for true single-mode selection. This is attributed to the small difference in threshold gains between the desired mode and the competitive mode (see Fig. 4.8). The LIV characteristics of a standard rectangular-shaped device (without any pattern) with the same aperture area is shown in Fig. 4.9 (solid curves) just for comparison to the patterned device. The threshold current of the patterned device is higher than that of the standard one due to the higher threshold gain induced by the antiphase layer in the

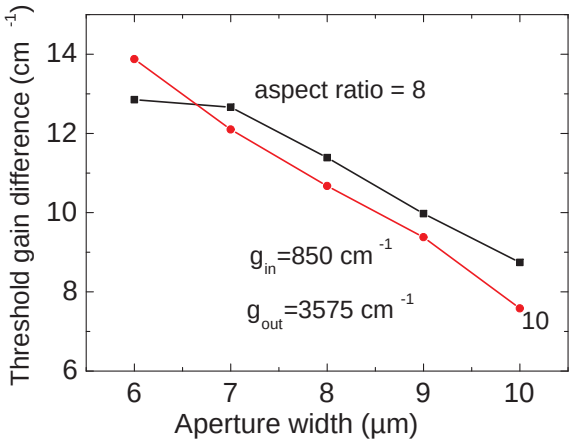

Figure 4.8: Dependence of the threshold gain difference Δg_{th} between the modes E_{81} and E_c on the aperture width d for structure 1 with pattern 1. Aspect ratios a/d are 8 or 10.

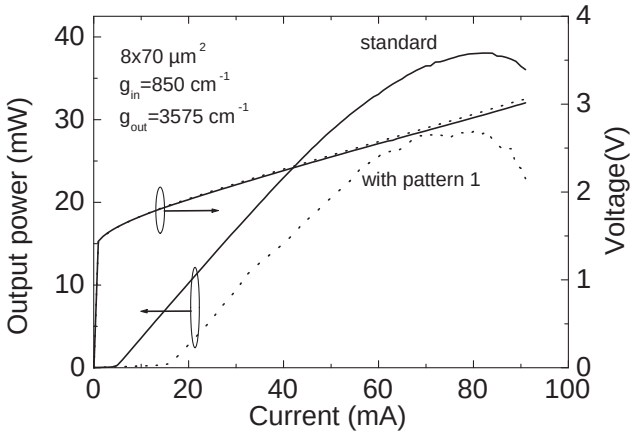

Figure 4.9: LIV characteristics of a VCSEL with structure 1 and pattern 1 (dotted curves) and that of a standard VCSEL with structure 1. The active aperture for both VCSELs is 8 µm × 70 µm.

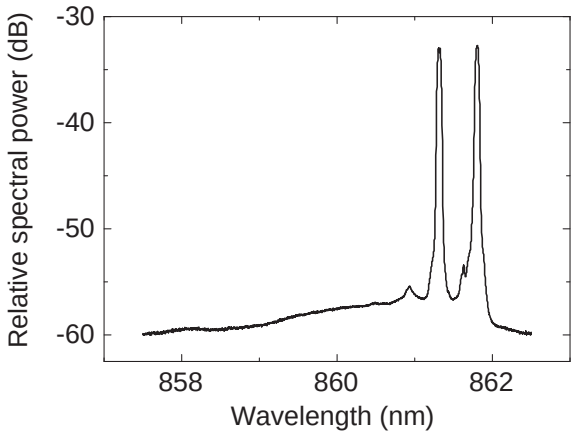

Figure 4.10: Laser emission spectrum of the patterned VCSEL from Fig. 4.9 at 25 mA current.

patterned device. Moreover, thermal rollover occurs with low output power compared with the standard one.

From (4.4) it is understood that mode selection is the better, the higher is the difference in threshold gains inside and outside the etched regions. For this purpose, another structure (number 2) has been utilized [1] with $g_{\mathrm{in}} = 1401\,\mathrm{cm}^{-1}$ and $g_{\mathrm{out}} = 6318\,\mathrm{cm}^{-1}$. The threshold gains of the modes as well as their difference are plotted in Fig. 4.11 (left) for structure 2 with pattern 1. It is seen that the threshold gains of the modes become large compared with structure 1 with pattern 1 (see Fig. 4.7 for comparison). The LIV characteristics from a sample with structure 2 is shown in Fig. 4.12 both for a standard device (without any

[1] The wafer of this structure was provided by Philips Technologie GmbH U-L-M Photonics and the layer structure is not known for us.

pattern) and an 8-spot shallow relief device (with pattern 1). The active apertures of the devices in Fig. 4.12 are both 7.5 µm × 69.5 µm. In practice, the higher thresholds of the modes in structure 2 with pattern 1 prevented lasing entirely (see dashed output power curve in Fig. 4.12), and we had to pre-etch the antiphase layer by 16 nm to reduce g_{out} from 6318 cm^{-1} to 3025 cm^{-1} (structure number 3). The results for this structure (number 3) are shown in Fig. 4.11 (right). As illustrated, the threshold gains of the modes decrease a lot compared with structure 2 before the pre-etching (see Fig. 4.11 (left) for comparison). However, the threshold gain differences between modes in structure 3 with pattern 1 are small compared with structure 2 with the same pattern. The LIV characteristics of structure 3 are shown in Fig. 4.13 for a devices with pattern 1 (dotted curve) and a standard device (solid curve). The light–current of the patterned VCSEL curve shows kinks at 20 mA and at 26.5 mA. These kinks indicate the onset of the competitive modes. Hence, below 20 mA this device operates in a single mode and above this value it shows multimode emission.

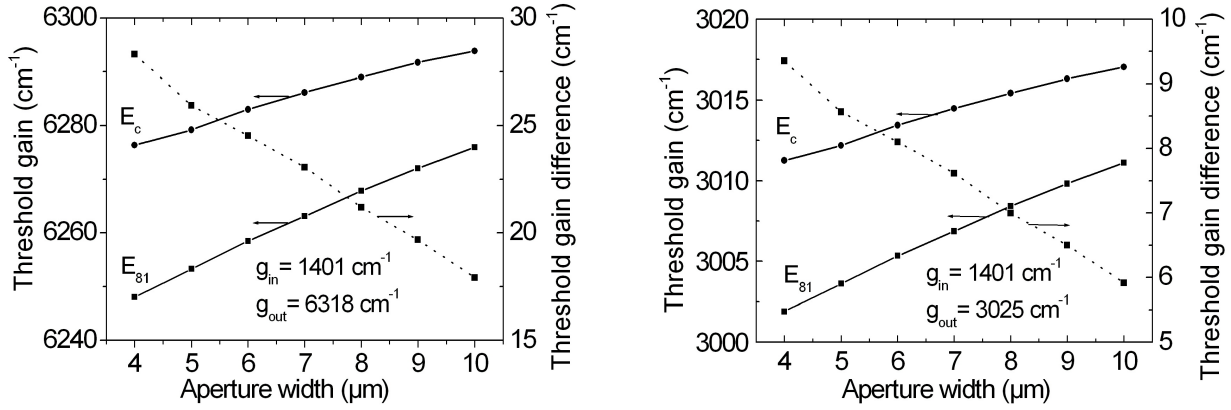

Figure 4.11: Threshold gains and their difference in VCSELs with layer structure 2 (left) and structure 3 (right), both with pattern 1 as a function of the aperture width d for the modes E_{81} and E_c. Aperture length and width are related by $a - d = 62\,\mu\text{m}$, i.e., the aspect ratio is not constant here.

This behavior is also observed in the emitted spectra shown in Fig. 4.14. Thus, the device cannot provide single-mode operation up to thermal rollover. In order to obtain a single-higher-order transverse mode even at maximum output power, we used again structure 2 but with another etching pattern (number 2). In this pattern, 8 circular spots each having 6 µm diameter (instead of 4 µm in pattern 1) are etched through the entire antiphase layer to match the mode E_{81}.

Figure 4.15 (left) shows the overlapping between the E_{81} mode (the mode to be selected) and pattern 2 (indicated with white circles). The overlapping of pattern 2 with mode E_{81} is higher than that of pattern 1 with mode E_{81} (see Fig. 4.5 for comparison). As the diameter of each spot changes from 4 µm to 6 µm, the competitive mode also changes from $E_{12\,1}$ to E_{91}. Figure 4.15 (right) shows the overlapping between the E_{91} mode and pattern 2. The confinement factors of the modes E_{81} and E_{91} as a function of the aperture width for a sample with layer structure 2 and pattern 2 is shown in Fig. 4.16. The increase in the spot diameter from 4 µm

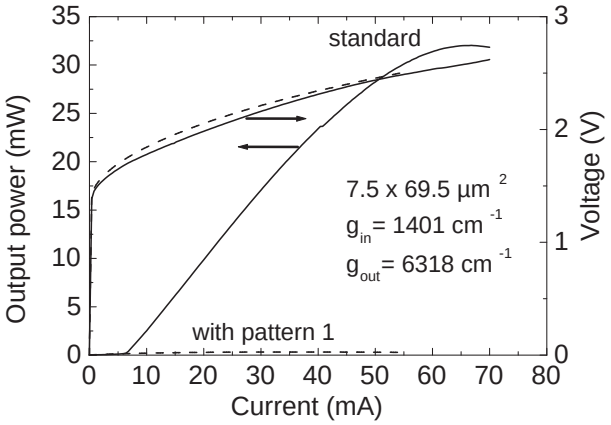

Figure 4.12: LIV characteristics of a VCSEL with structure 2 and pattern 1 (dashed curves) and that of a standard VCSEL with structure 2. The calculated values of g_{in} and g_{out} as well as the dimensions of the oxide aperture are given in the graph. The higher threshold gain prevent lasing of the patterned VCSEL.

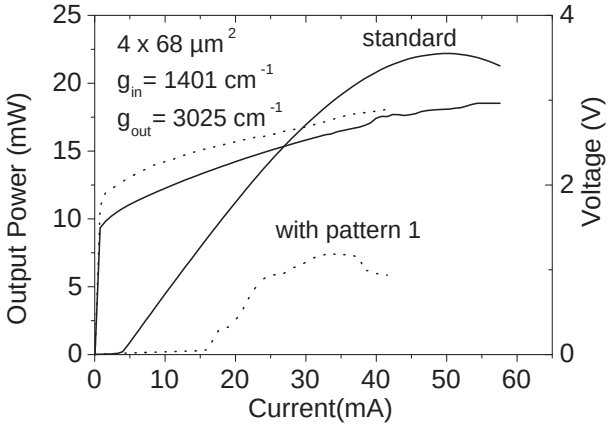

Figure 4.13: LIV characteristics of a VCSEL with structure 3 and pattern 1 (dotted curves) and that of a standard VCSEL with structure 3. The calculated values of g_{in} and g_{out} as well as the dimensions of the oxide aperture are included in the graph.

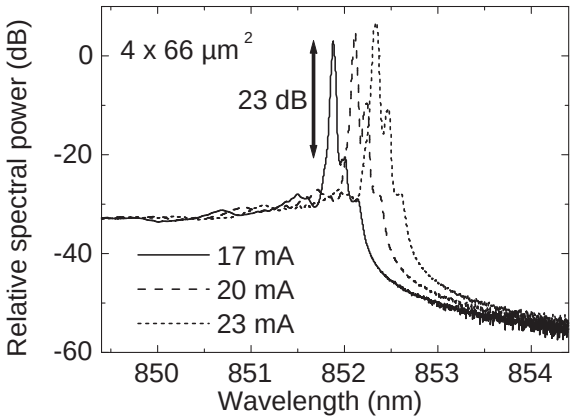

Figure 4.14: Laser emission spectra of a VCSEL with structure 3 and pattern 1 at different bias currents. The active aperture size is 4 µm × 66 µm.

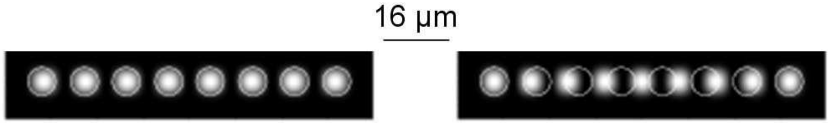

Figure 4.15: Simulated intensity profiles of the targeted mode E_{81} (left) and the competitive mode E_{91} (right). The active aperture is 6.3 µm × 68.3 µm. The etching spots are indicated with white circles.

to 6 µm leads to an increase of the confinement factor (compare Figs. 4.6 and 4.16). The

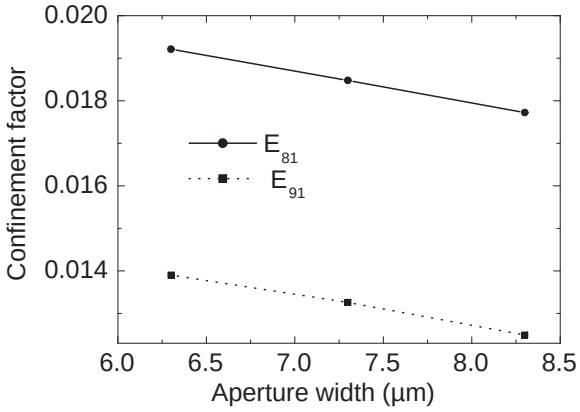

Figure 4.16: Dependence of the confinement factor Γ of the modes E_{81} (desired mode) and E_{91} (competitive mode) on the aperture width d for samples with structure 2 and pattern 2. Aperture length and width are related by $a - d = 62\,\mu m$. The individual diameter of an etch spot is 6 µm.

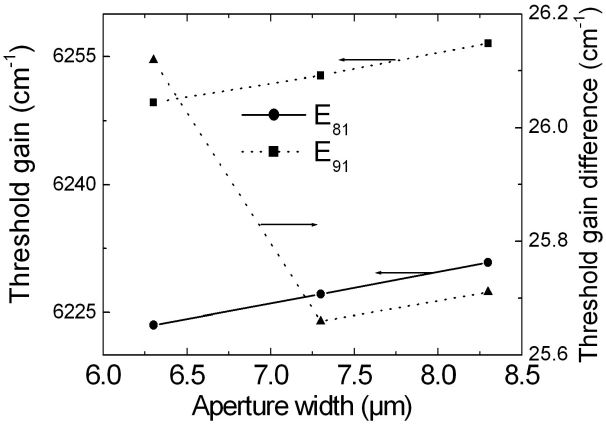

Figure 4.17: Threshold gains and their difference as a function of the aperture width corresponding to Fig. 4.16.

corresponding threshold gains of the modes E_{81} and E_{91} as a function of the aperture width is plotted in Fig. 4.17 (left axis). There is a slight decrease of the threshold gains compared with Fig. 4.11 (left). Figure 4.17 (right axis) plots the corresponding threshold gain difference between the modes E_{81} and E_{91} for a sample with structure 2 and pattern 2. There is an enhancement of the threshold gain difference using this pattern compared with structure 3 having pattern 1 (see Fig. 4.11 (right) for comparison).

The LIV characteristics and spectra of a VCSEL with layer structure 2 and pattern 2 are shown in Fig. 4.18 and Fig. 4.19, respectively. As shown in the spectrum at 50 mA, which is above the thermal rollover point, only one main mode oscillates. The maximum single-mode output power exceeds 12 mW.

4.4 Near-Field of a Single-higher-order Transverse Mode VCSEL

In order to identify the main modes in the spectra in Fig. 4.19 and Fig. 4.14, we have performed spectrally resolved near-field measurements by scanning a lensed fiber tip over the output aperture with high resolution. Figure 4.20 (left) and Fig. 4.21 (left) show the corresponding measured near-field intensities of the VCSELs having spectra of Fig. 4.19 and Fig. 4.14, respectively. The near-fields are recorded at currents of 30 mA and 18 mA, respectively, and show clear signatures of the E_{81} mode. The emitted laser intensity from each spot is not constant due to the current density inhomogeneity [49] and heat inhomogeneity

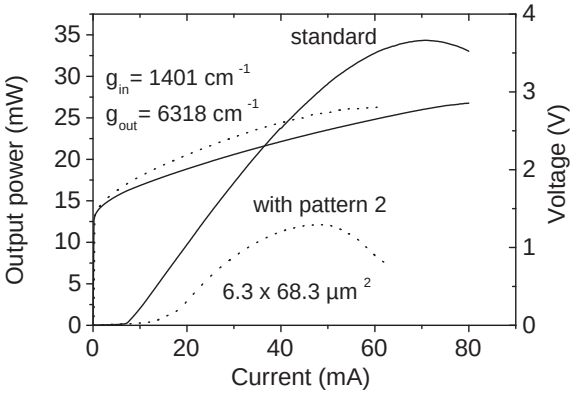

Figure 4.18: LIV characteristics of a VCSEL with structures 2 and pattern 2 (dotted curves) and that of a corresponding standard VCSEL. The active aperture is 6.3 µm × 68.3 µm.

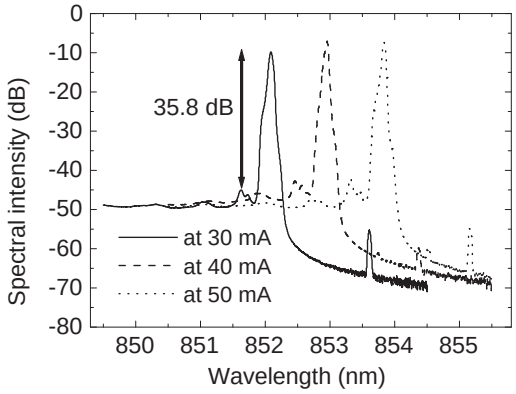

Figure 4.19: Laser emission spectra of the patterned VCSEL from Fig. 4.18 for different bias currents.

[44] throughout the active aperture. The simulated intensity profiles of these modes using the finite element method are displayed in Fig. 4.20 (right) and Fig. 4.21 (right). The heat effect and the current inhomogeneity are neglected in the simulations.

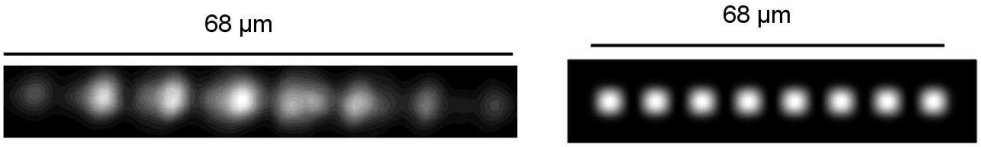

Figure 4.20: Measured near-field intensity profile (left) of an 8-spot etched VCSEL with structure 2 and pattern 2 recorded at 30 mA and the corresponding simulated intensity profile of the selected E_{81} mode (right). The active aperture area is 6.3 × 68.3 µm^2 and the individual spot diameter is 6 µm.

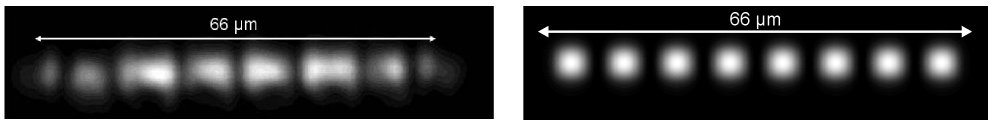

Figure 4.21: Measured near-field intensity profile (left) of an 8-spot etched VCSEL with structure 2 and pattern 1 recorded at 18 mA and the corresponding simulated intensity profile of the selected E_{81} mode (right). The active aperture area is 4 × 66 µm^2 and the individual spot diameter is 4 µm.

4.5 Far-Field of a Single-Higher-Order Transverse Mode VCSEL

Let us now discuss the far-field pattern obtained from a multi-spot shallow-etched rectangular-shaped VCSEL of Fig. 4.2 having spectra as shown in Fig. 4.19. The coherent laser spots emitted from such a device produce an interference pattern. We need to determine the intensity at the detector when the distance Z between detector and VCSEL is at least 100 times larger than the aperture area divided by the wavelength, A/λ, which is the condition for the far-field. The device has eight spots with $d_\mathrm{r} = 6\,\mu\mathrm{m}$ diameter of each relief and $b = 9\,\mu\mathrm{m}$ pitch, as indicated in Fig. 4.22.

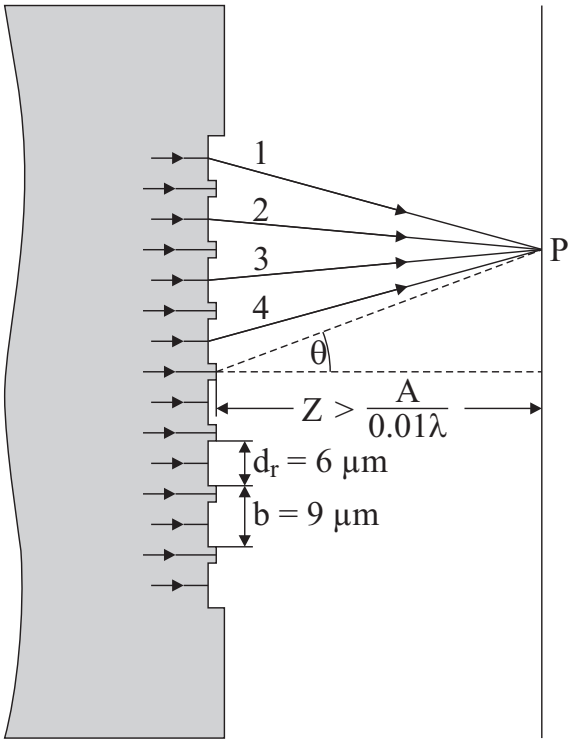

Figure 4.22: Sketch illustrating the device parameters for interference in the far-field. The point P indicates the detector position.

When the detector is scanned over all angles θ, the far-field intensity of such a pattern is given by [64]

$$I(\theta) = I_0(2J_1(\alpha)/\alpha)^2(\sin(N\beta)/\sin(\beta))^2, \tag{4.5}$$

where I_0 is a constant intensity, $J_1(\alpha)$ is the first-order Bessel function and

$$\alpha = \pi d_\mathrm{r} \sin(\theta)/\lambda. \tag{4.6}$$

The term $(\sin(N\beta)/\sin(\beta))^2$ is due to the interference between these multiple coherent laser spots. N is equal to the number of spots (in this case $N = 8$) and

$$\beta = \pi b \sin(\theta)/\lambda + \pi/2. \tag{4.7}$$

The term $\pi/2$ accounts for the antiphase layer added above the p-DBR. The first-order Bessel function in (4.5) is responsible for the diffraction.

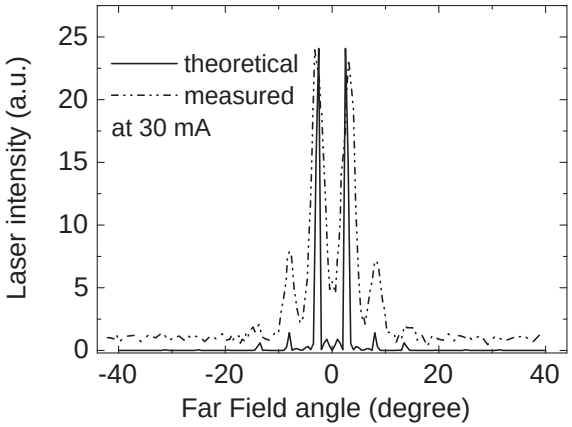

Figure 4.23: Far-field intensity profiles of an 8-spot surface-etched rectangular-shaped VCSEL with 6 µm diameter of each spot and 9 µm pitch. The laser current is 30 mA. The active aperture area is 6.3 µm × 68.3 µm. Solid and dash-dotted curves are for theoretical and measured far-field intensities, respectively.

The calculated and the measured far-field intensity profiles are indicated in Fig. 4.23. There is a good agreement between the theoretical and measured far-fields. The broadening in the measured curve is attributed to heat effects. As the current flows through the VCSEL structure, heat is generated. The temperature profile tends to focus the beam in the center. The focussing of the beam in the near-field means more divergence of the beam in the far-field, as observed in Fig. 4.23. The intensity maxima of the pattern are defined by the condition

$$\beta = \pi b \sin(\theta_m)/\lambda + \pi/2 = m\pi, \tag{4.8}$$

where the integer m gives the order of interference. The corresponding angles at which these maxima occur are given by

$$\theta_m = \arcsin\left[\frac{\lambda}{b}\left(m - \frac{1}{2}\right)\right]. \tag{4.9}$$

Chapter 5

Semiconductor Technology for Device Manufacturing

In this chapter, the different processes needed for device manufacturing are discussed. For the experimental work of the thesis, both single-higher-order transverse mode rectangular-shaped VCSELs and densely packed matrix-addressable VCSEL arrays are manufactured and characterized. Some essential processes of manufacturing are discussed briefly in this chapter. However, the VCSEL growth is outside the scope of this thesis. More details about VCSEL growth at Ulm University are found in [65]–[67]. The layer structures of some VCSELs utilized in this thesis are listed in App. B. All samples utilized in the thesis are grown by molecular beam epitaxy.

5.1 Manufacturing of Single-Higher-Order Transverse Mode VCSELs

A crucial process throughout manufacturing is photolithography. In this process, the structure of the mask is transformed to the semiconductor sample using the convenient photoresist. Essentially, there are two types of photoresists, namely positive photoresist and negative photoresist. For the positive photoresist, the region which is exposed to ultra-violet (UV) radiation will be removed during the development process. This allows the same structure of the mask to be transformed to the semiconductor sample. For the negative photoresist, the part which is exposed to UV radiation will solidify, and during development, only the unexposed part will be removed. The different processes that are done to manufacture higher-order transverse mode and normal rectangular-shaped VCSELs are depicted in Fig. 5.1 and Fig. 5.2. First the mesas with different patterns are defined using a photolithographic process, as shown in step 1 in Fig. 5.1. Then shallow etching is carried out to select certain higher-order transverse mode. In step 2 of Fig. 5.1 (left), 8-spot shallow surface etching to select the E_{81} mode is illustrated. For obtaining a standard device without any pattern, complete etching of the antiphase layer is done, as demonstrated in step 2 in Fig. 5.1 (right).

Then the relief is covered with photoresist (step 3) and wet etching to a depth below the AlAs layer is carried out (step 4). Thermal oxidation of a part of the AlAs layer is done. The most critical step in processing is this step, because single-mode behavior is very sensitive to the active aperture dimension. The function of this process is two fold: Not only current confinement, but also optical guiding. In step 6 in Fig. 5.2, n-metalization of the back side of the wafer is done. In step 7, a photolithographic process for p-metalization is performed, so that one can apply a p-ring contact. In step 8, a lift-off process is done after the evaporation of the metals. Both n- and p-metalization are needed to obtain ohmic contacts. Polyimide passivation is done in step 9 to avoid a short-circuit when the bondpad metalization (step 10) is formed. Top-view photographs of fully-processed 8-spot shallow surface-etched and standard rectangular-shaped VCSELs are shown in Fig. 4.2 and Fig. 4.3, respectively.

5.2 Manufacturing of Matrix-Addressable VCSEL Arrays

The most appropriate devices for the fabrication of large two-dimensional arrays of compact, coherent optical sources are VCSELs, owing to their low threshold currents and their high packing density. These two-dimensional arrays are of great potential importance for optical interconnection schemes, optical scanners and confocal laser microscopes.

In this section we will discuss briefly the manufacturing of matrix-addressable VCSEL arrays. For more details about this device, see Chap. 7. Using photolithography, we define the mesas of VCSELs in the arrays, then etch down to the heavily-doped n-buffer layer. While chemical wet-etching is cheap, it does not allow a high packing density of the array, owing to anisotropic etching of the mesa. We fabricated two generations of matrix-addressable VCSEL arrays, one using wet-etching and the other using dry-etching. After reaching the n-layer, another lithographic is applied to isolate the columns. Then thermal oxidation of a part of the AlAs layer is done. Afterwards, n-metalization is applied throughout the columns. Figure 5.3 shows a sketch of the VCSEL array after defining the mesas, etching down to the heavily-doped n-layer, separation of the columns and applying an n-metalization above the columns. The next step is to planarize the etched regions with polyimide. Three polyimide steps are needed to make such planarization. First filling the grooves between columns, and then two polyimide steps are needed for planarization because of the large height difference. Figure 5.4 shows a schematic drawing of the VCSEL array after polyimide planarization. Then a p-metalization is applied throughout the rows. Figure 5.5 shows a sketch after this p-metalization. For packaging of these VCSEL arrays, thick metal layers are evaporated on the bondpad to guarantee a successful wire bonding process. The last step is wire bonding to a circuit package. A photograph of the final chip after mounting is illustrated in Fig. 7.4.

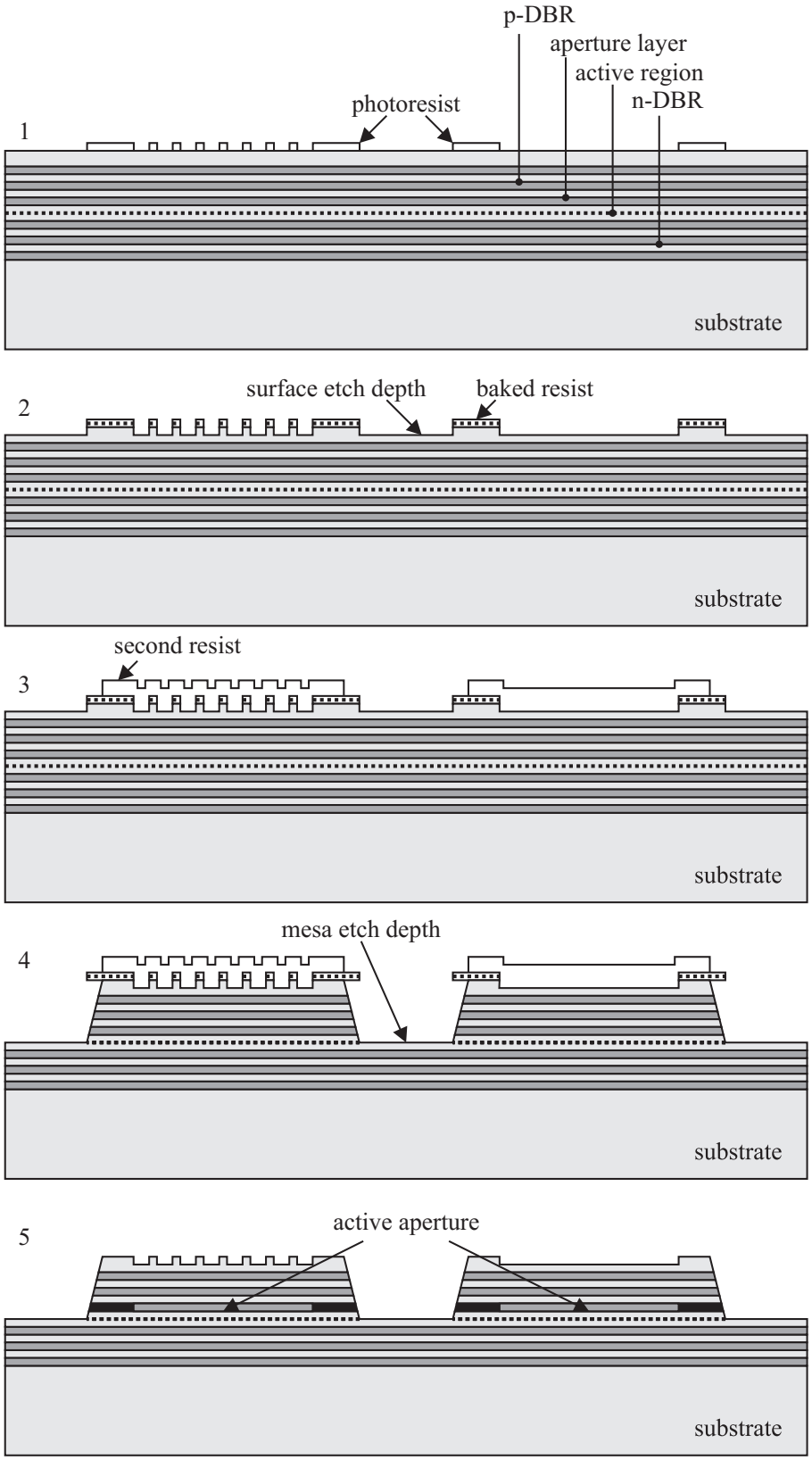

Figure 5.1: Sketch of processing sequences of single-higher-order transverse mode (left) as well as normal rectangular-shaped (right) VCSELs.

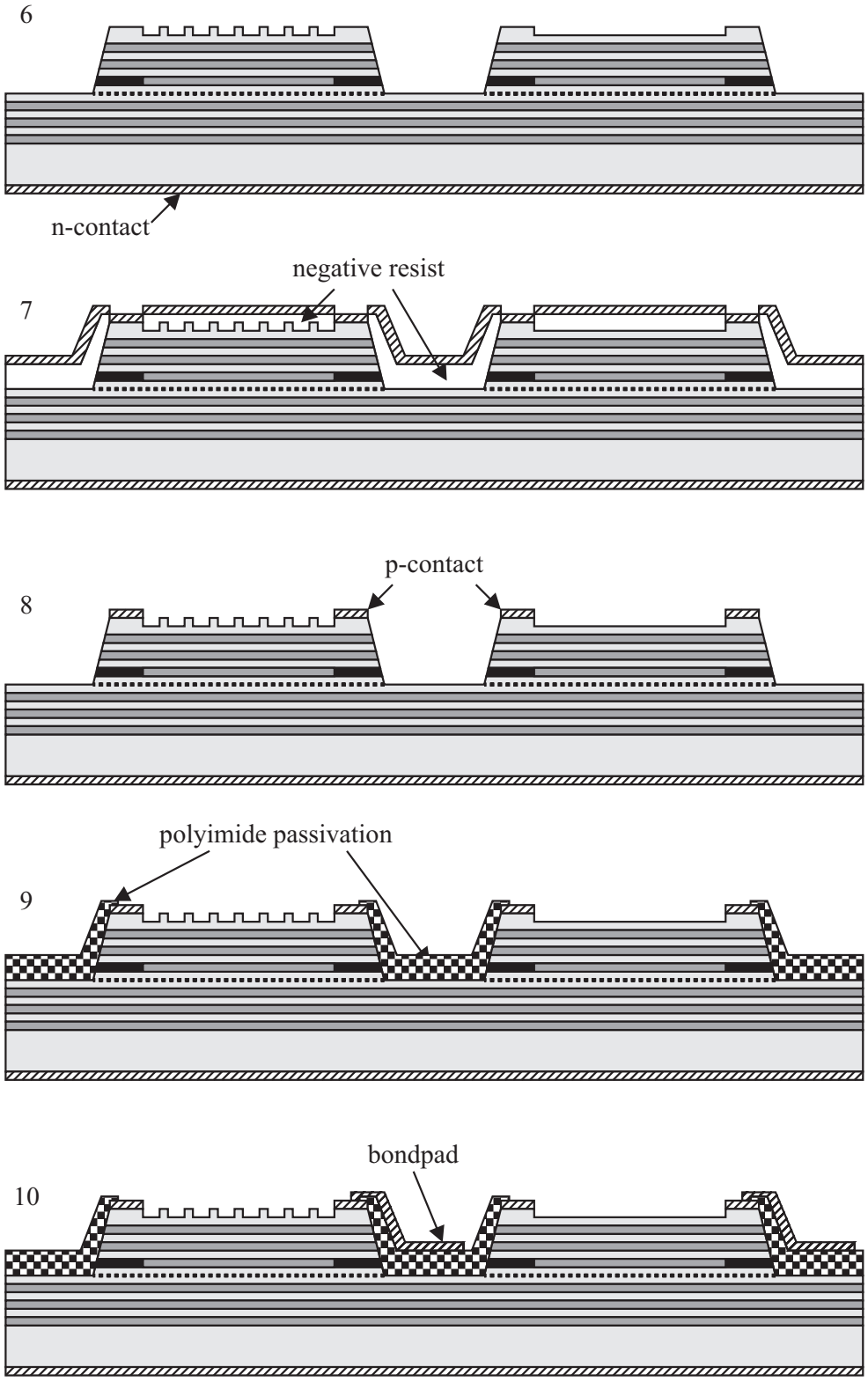

Figure 5.2: Processing sequences continued from Fig. 5.1.

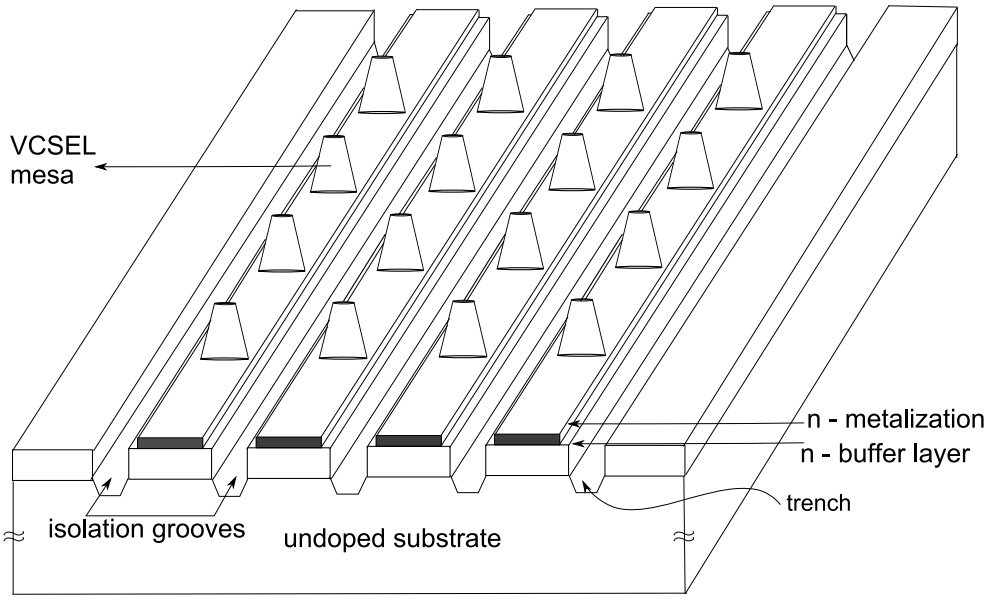

Figure 5.3: Sketch demonstrating defining the mesas, columns and n-metalization for columns in matrix-addressable VCSEL array processing.

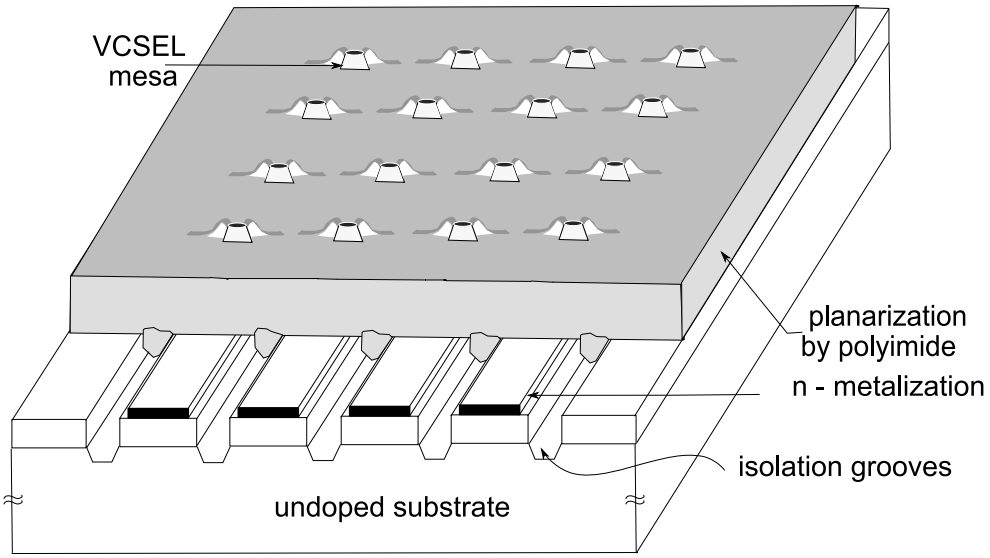

Figure 5.4: Sketch demonstrating polyimide filling between columns and polyimide planarization throughout the VCSEL arrays.

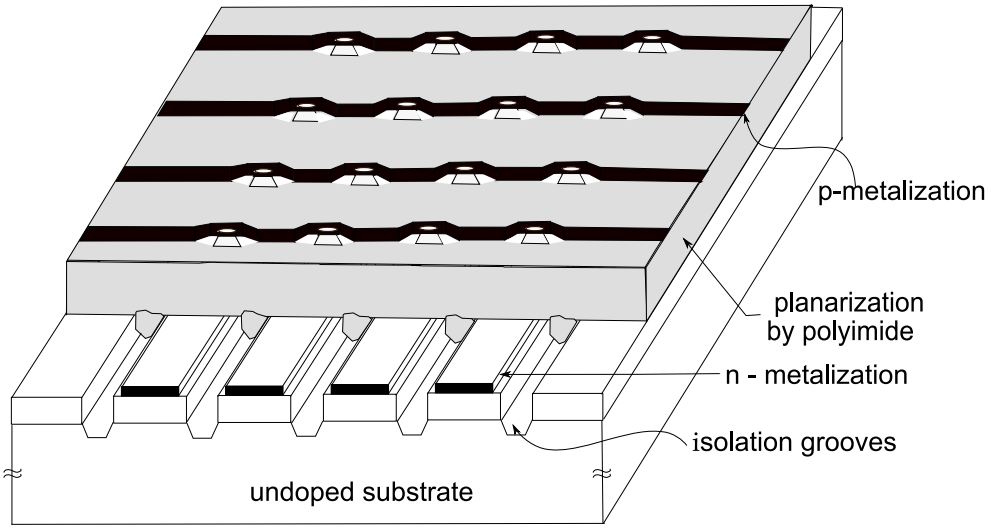

Figure 5.5: Sketch demonstrating p-metalization through the rows in matrix-addressable VCSEL arrays.

Chapter 6

Experimental Results: Standard Versus Multi-Spot Surface-Etched VCSELs

In this chapter, the laser characteristics of standard and multi-spot surface-etched rectangular-shaped VCSELs are investigated. By the words "standard" or "normal" we mean that the antiphase layer above the top DBR is totally removed so that we have the standard layer structure of the VCSEL. And with the word "rectangular-shaped" we mean that the active aperture area is of a rectangular shape with an aperture length a and an aperture width d. The term "multi-spot surface-etched" indicates that the top surface of the VCSEL has a shallow etch pattern of multiple spots in order to stimulate laser oscillation for only a specific transverse mode. Such a shallow etch pattern is applied to the antiphase layer, which is above the top p-DBR mirror. The standard rectangular-shaped VCSELs serve as reference devices for the multi-spot surface-etched lasers.

6.1 Standard Rectangular-Shaped VCSEL Characteristics

In this section, laser characteristics such as differential quantum efficiency, threshold current density together with the spectra, near- and far-fields of standard rectangular-shaped VCSELs are investigated in detail, aiming for a performance enhancement in both single-mode and multi-mode regimes of such type of VCSELs. A micrograph showing a top view of a fully-processed normal rectangular-shaped VCSEL is shown in Fig. 4.3.

6.1.1 Light–Current–Voltage Characteristics

A schematic representation of the setup utilized for the light–current–voltage (LIV) characterization is shown in Fig. 6.1. The CCD (charge-coupled device) camera with the monitor, the halogen lamp, the two lenses and the beamsplitters in the setup are used to image an individual VCSEL and hence to allow electrical contacting of the device.

In order to investigate the effect of changing the oxide aperture size on the performance of normal rectangular-shaped VCSELs, different mesa dimensions have been processed on a molecular beam epitaxially grown sample with good layer homogeneity. LIV characteristics of lasers with different widths d and lengths a are illustrated in Fig. 6.2. The active dimensions (width $\times$ length) of the devices, e.g., $1.5\,\mu\text{m} \times 28\,\mu\text{m}$, are indicated in the graphs. As the aperture length increases, both the threshold current and the maximum output power at thermal rollover increase. For example, when the aperture area is $1.5\,\mu\text{m} \times 8\,\mu\text{m}$, the threshold current and the output power at thermal rollover are 0.5 mA and 1.7 mW, respectively. These values increase to 1.5 mA and 6 mW as the aperture area increases to $1.5\,\mu\text{m} \times 28\,\mu\text{m}$.

As displayed in Fig. 6.2, a laser output power up to 40 mW can be obtained using a $9.5\,\mu\text{m} \times 88\,\mu\text{m}$ aperture. On the other hand, a threshold current as low as 0.5 mA is realized using a $1.5\,\mu\text{m} \times 8\,\mu\text{m}$ aperture.

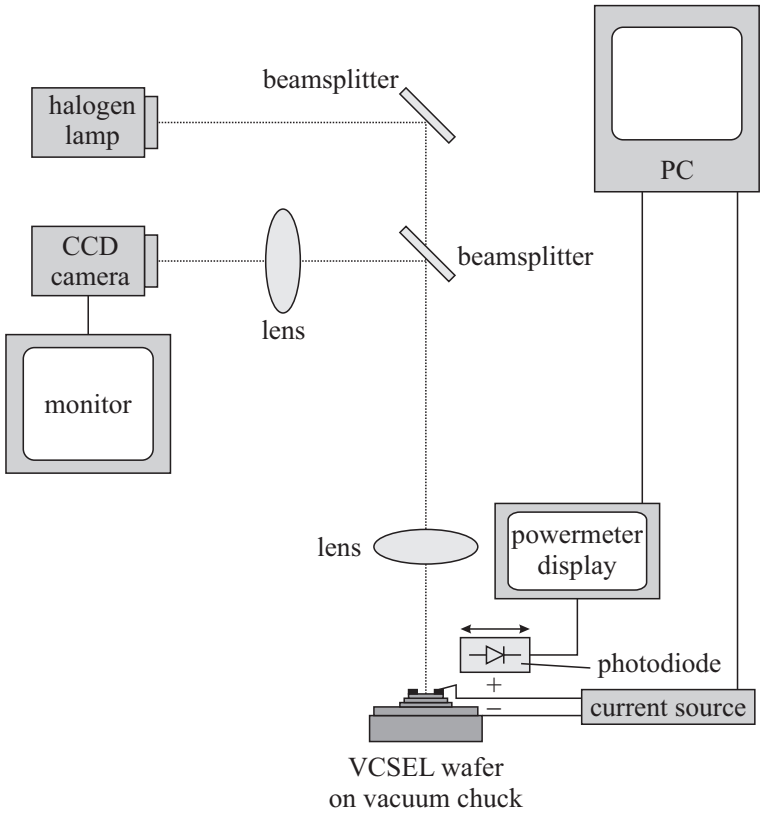

Figure 6.1: Sketch of the measurement setup.

The dependence of the differential quantum efficiency η_d and the nominal threshold current density j_{th} on the aperture dimensions were also investigated. The latter is calculated using

$$j_{\text{th}} = \frac{I_{\text{th}}}{d \times a}, \tag{6.1}$$

with I_{th} as the threshold current. In (6.1) it is assumed that the current is constant throughout the active aperture. The differential quantum efficiency η_d above laser threshold and below thermal rollover is defined using (2.20).

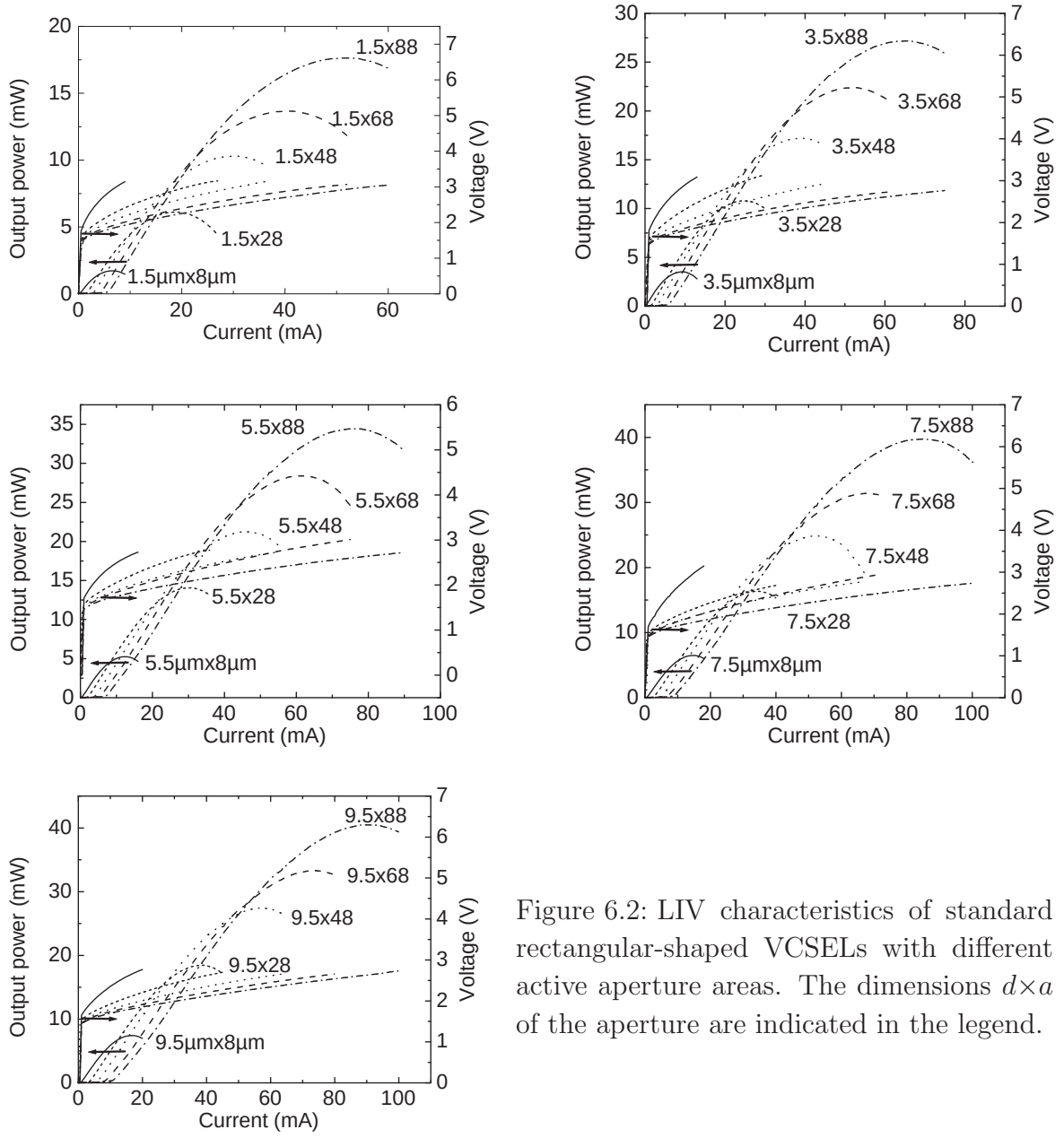

Figure 6.2: LIV characteristics of standard rectangular-shaped VCSELs with different active aperture areas. The dimensions $d \times a$ of the aperture are indicated in the legend.

Figure 6.3 shows the dependence of η_d as a function of the aperture length at different aperture widths. At aperture widths of 1.5 µm, 3.5 µm, and 7.5 µm, η_d is maximum at 48 µm aperture length. However, at 5.5 µm and 9.5 µm aperture widths, η_d is maximum at an aperture length of 28 µm. The dependence of η_d on the aperture width for different lengths is depicted in Fig. 6.4. For aperture widths below 6 µm, the scattering losses decrease as the aperture width increases, and hence the differential quantum efficiency increases. The highest η_d among the investigated VCSELs was measured as 51.7 % at 9.5 µm × 28 µm active aperture area. This enhancement in the differential quantum efficiency is attributed to an optimized active aperture of the device [68]. The nominal threshold current density as a function of the aperture width is depicted in Fig. 6.5. It reflects the scattering losses α_s that occur when the aperture width is less than about 6 µm. The scattering loss for a single pass

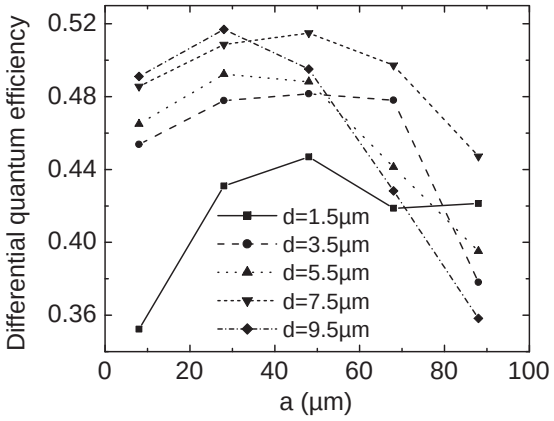

Figure 6.3: Differential quantum efficiencies from Fig. 6.2 versus aperture length a for different aperture widths d.

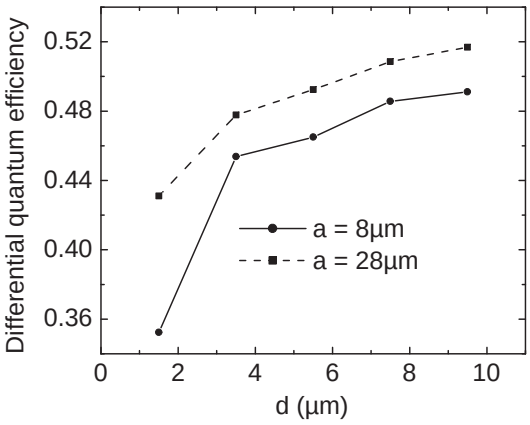

Figure 6.4: Differential quantum efficiencies from Fig. 6.2 versus aperture width d for two different aperture lengths a.

through the cavity is given by [69]

$$\alpha_s = (\phi_0^{1.19}/F^{1.3}) \exp(-0.206/(\phi_0 F)), \tag{6.2}$$

where ϕ_0 is the characteristic phase shift of the aperture, and F is the Fresnel number. They are defined as [70]

$$\phi_0 = \frac{2\pi}{\lambda} \Delta n_{ox} L_{eff}, \tag{6.3}$$

$$F = \frac{a_{eff}^2 n_1}{\lambda L_{eff}}, \tag{6.4}$$

where L_{eff} is the effective cavity length (see Sect. 2.4), a_{eff} is the effective radius of the aperture, n_1 is the refractive index at the center of the aperture and Δn_{ox} is the refractive index contrast due to oxidation according to (3.1), (3.2). The dependence of the threshold current density on the aperture length is shown in Fig. 6.6. There is a minimum in the threshold current density at 68 µm aperture length. The lowest threshold current density among the investigated VCSELs was measured to be 1.24 kA/cm^2 for 9.5 µm × 68 µm active aperture. From the current–voltage (IV) curves of these VCSELs the differential series resistance R_s can be extracted from the linear part of the curve (after threshold and below thermal rollover) [68]. With increasing the aperture area, this resistance decreases as indicated in Fig. 6.7. At an aperture area of 420 µm^2, R_s was measured as 15 Ω. The solid curve in the figure is a theoretical fitting of R_s as a function of the aperture area. Its equation is

$$R_s = \frac{5310\ \Omega\mu m^2}{d \times a}. \tag{6.5}$$

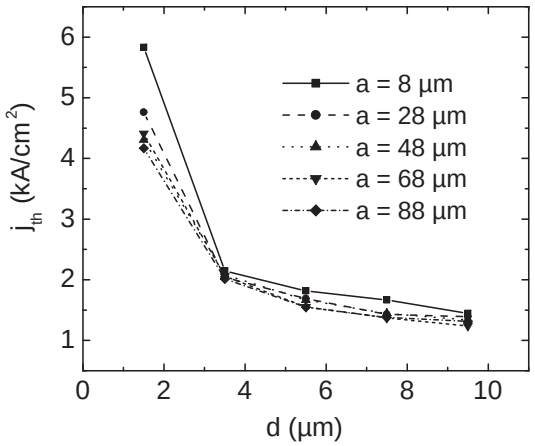

Figure 6.5: Threshold current densities j_{th} of VCSELs from Fig. 6.2 versus the aperture width d for different lengths a.

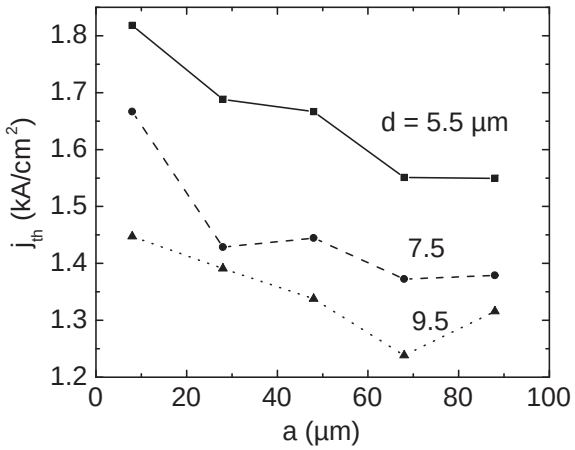

Figure 6.6: Threshold current densities j_{th} of VCSELs from Fig. 6.2 versus the aperture length a for three widths d.

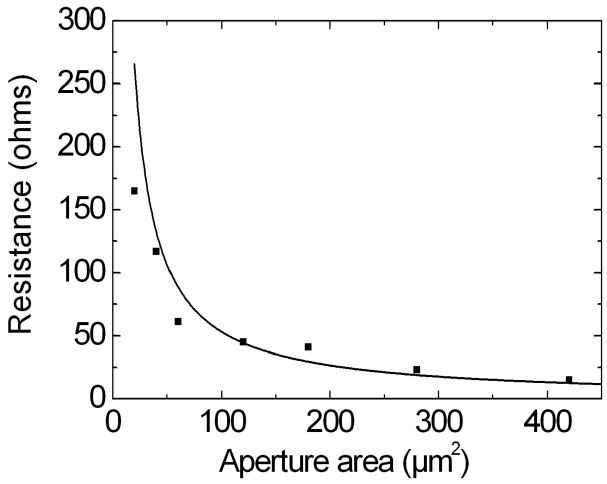

Figure 6.7: Differential series resistances of VCSELs from Fig. 6.2 (squares) plotted as a function of the aperture area. The solid curve is using (6.5).

6.1.2 Spectra Measurements

The spectra emitted from the VCSELs were recorded using an optical spectrum analyzer. Figure 6.8 shows the laser spectra emitted from a 1.5 µm × 8 µm aperture area VCSEL at different excitation currents. The side-mode suppression ratio (SMSR) between the fundamental transverse mode at 851.36 nm and the first higher-order transverse mode at 851.01 nm is 22 dB at a current of 1 mA. As the current increases to 4 mA, the peak laser wavelength of the fundamental mode shifts to 853.01 nm. Such red-shift of about 0.55 nm/mA is attributed to the temperature dependence of the Fabry-Perot cavity resonance [71]. As the current increases, the temperature increases too. The refractive index of the cavity in response to this additional current will increase (see (3.16)). Hence optical cavity length increases too and this accompanied with a change in the Fabry–Perot cavity resonance (see (2.9)). At the same

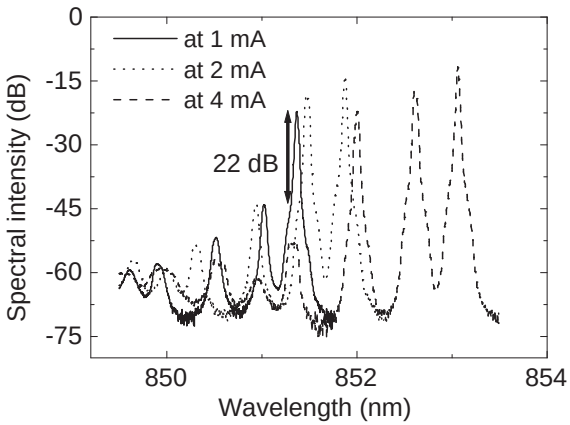

Figure 6.8: Emission spectra of a rectangular-shaped VCSEL with an aperture area of 1.5 µm × 8 µm at different currents.

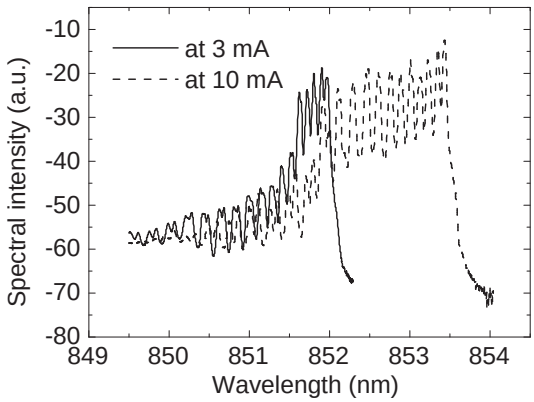

Figure 6.9: Emission spectra of a 1.5 µm × 28 µm size VCSEL at two bias points.

time, the SMSR reduces to around 5 dB. The spectra emitted from a 1.5 µm × 28 µm VCSEL, a larger-area device, are depicted in Fig. 6.9. From this figure, it is also observed that with increasing the excitation current, the number of excited transverse modes increases. This is attributed to a thermal guiding effect, i.e., an increase of the refractive index contrast from the center of the device to the edge. With a higher index contrast, the frequency parameter V increases too. The number of excited transverse modes increases with increasing the V parameter. In addition to the thermal guiding effect, spatial hole burning increases the number of mode at high laser intensity. Another feature in this figure compared with Fig. 6.8 is that with increasing the aspect ratio, the number of excited transverse modes increases and the transverse mode spacing decreases. At an aperture area of 1.5 µm × 28 µm, the transverse mode spacing between the fundamental mode and the first higher-order transverse mode is ≈ 0.08 nm at 3 mA. This transverse mode spacing increases to 0.4 nm as the aperture area is reduced to 1.5 µm × 8 µm.

6.1.3 Near-Field Measurements

A schematic sketch of the setup used to record spectrally and spatially resolved near-field intensity profiles is shown in Fig. 6.10 [72]. A single-mode fiber with an integrated lens (focal length of 12 µm) is moved by a three-axes piezoelectric stage above the VCSEL. The distance from the fiber to the VCSEL can be controlled using the stage. At every position of the two-dimensional scan, the complete spectrum of the VCSEL is measured with a multi-wavelength meter and the wavelengths and the intensities of different peaks are recorded. After the scan is ended, the different transverse modes can be extracted by sorting the peaks of the spectra recorded at the different scan positions according to their wavelengths. The measured near-field intensity profiles of some identified transverse modes are illustrated in Fig. 6.11. The active aperture of a normal rectangular-shaped VCSEL in this measurement

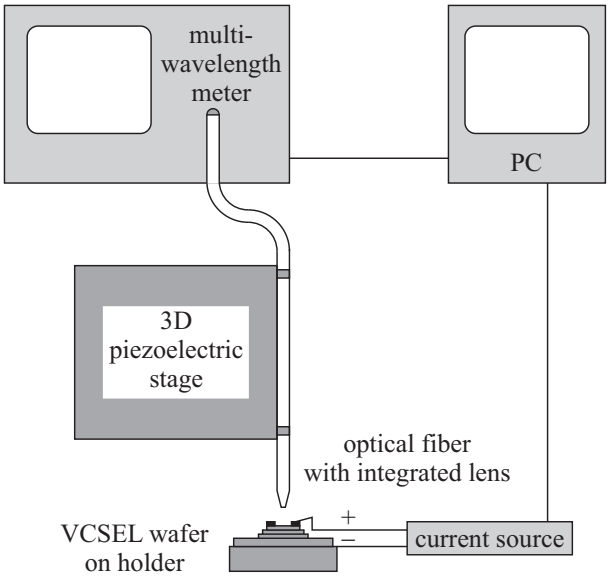

Figure 6.10: Schematic drawing of the setup used for near-field measurements.

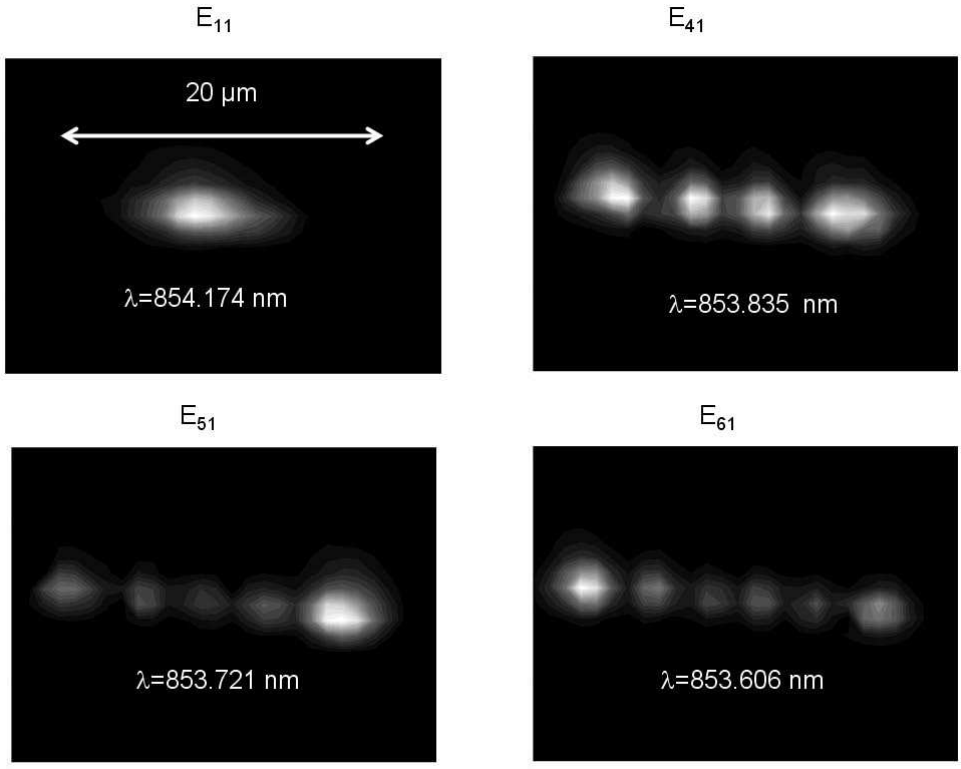

Figure 6.11: Near-field intensity profiles of some transverse modes in a rectangular-shaped VCSEL with 1.5 µm × 28 µm active aperture area. The measurements were done at 10 mA.

is 1.5 µm × 28 µm. The area scanned by the fiber is 20 µm × 30 µm with a step width of 500 nm. The transverse mode spacing between E_{41} and E_{51}, two neighboring transverse

modes, is 0.114 nm. Using (3.37) with $\Delta\lambda = 0.114\,\text{nm}$, $l = 4$, $k_l = 1.248$, $n = 3.3$, and $\lambda = 853.835\,\text{nm}$, the estimated Rayleigh range of the E_{41} mode is 53.3 µm. The estimated spot size of the fundamental mode $\omega(0)$ using (3.35) is then 9.15 µm. The corresponding mode diameter of the beam is 18.3 µm, which is smaller than the aperture length $a = 28\,\mu\text{m}$. For higher-order modes, the spot size is defined to be half the distance from the centers of the outer intensity peaks [53]. In our case, the integrated lens of the scanning fiber focuses the mode so that the spot size cannot be read from Fig. 6.11 directly.

6.1.4 Far-Field Measurements

Valuable information can be obtained using the far-field measurements such as the divergence angle of the laser beam and the single-mode behavior. The setup used for such measurements is schematically illustrated in Fig. 6.12. Illumination and monitoring of the VCSEL is done equivalent to Fig. 6.1. A photodiode moves along a semicircle with a radius of approximately 15 cm to detect the emitted radiation and the VCSEL is located in the center. Inserted on the photodiode is a slit to enhance the accuracy in the spatial-intensity measurement. The distance Z between the VCSEL and the photodiode must satisfy the far-field criterion, that is

$$Z \gg \frac{A}{\lambda}, \tag{6.6}$$

where A is the aperture area of the laser and λ is the laser wavelength in free space. Figure 6.13 demonstrates the far-field intensity profiles as a function of the far-field angle for an aperture area of 1.5 µm × 8 µm at different excitation currents. At a current of 1 mA, there is only one lobe, indicating single-mode behavior. This is in agreement with the spectra measurements in Sect. 6.1.2. The intensity full width at half maximum (FWHM) is 12°. As the current increases to 4 mA, two peaks are observed, indicating multi-transverse mode operation with E_{21} as the dominant mode. This can be interpreted as follows: With increasing the current, the heat will increase, and thus the lateral change of the effective refractive index Δn increases too (Sect. 3.1.3). Such an increase in refractive index contrast leads to an increase of the frequency parameter, that is associated with a larger number of excited modes (Sect. 3.2). Figure 6.14 shows similar characteristics for an aperture area of 1.5 µm × 28 µm except that there are narrow peaks superimposed to broad peaks at 10 mA, which indicates a much increased number of lasing modes.

6.1.5 Polarization-Resolved LIV Characteristics

For polarization-sensitive applications such as magneto-optic discs and coherent detection, the polarization state of the VCSEL must be defined. Firstly, we will discuss the polarization emitted from rectangular-shaped VCSELs operating in the multi-transverse mode regime. For single-mode single-polarization emission from multi-spot rectangular-shaped VCSELs, we refer to Sect. 6.2.5. The identification of crystal direction as given from the manufacturer is indicated in Fig. 6.15. It is worth to mention that for VCSELs grown on (100)-oriented

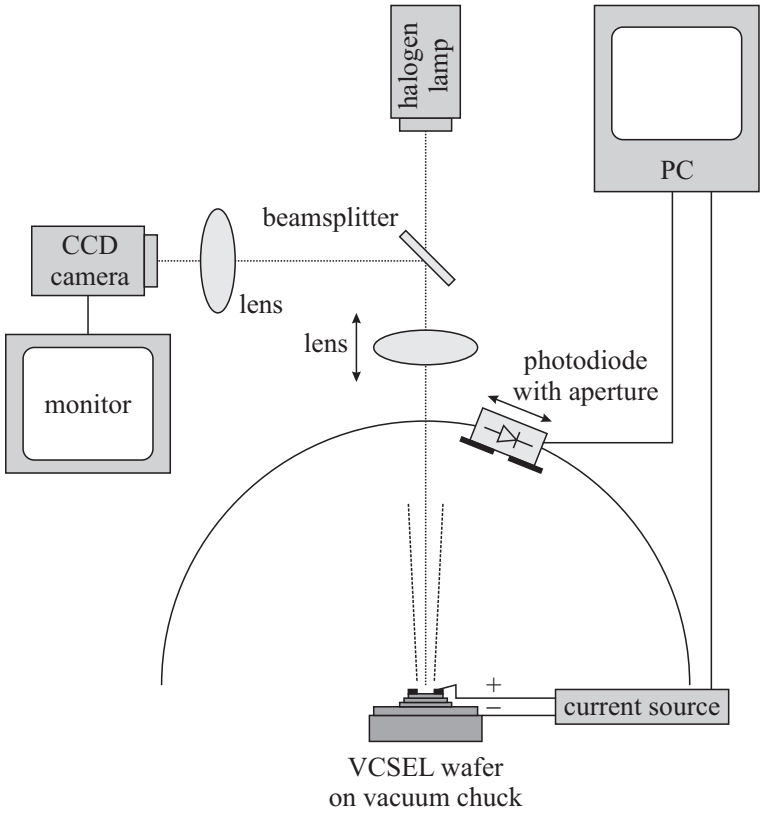

Figure 6.12: Sketch of the far-field setup.

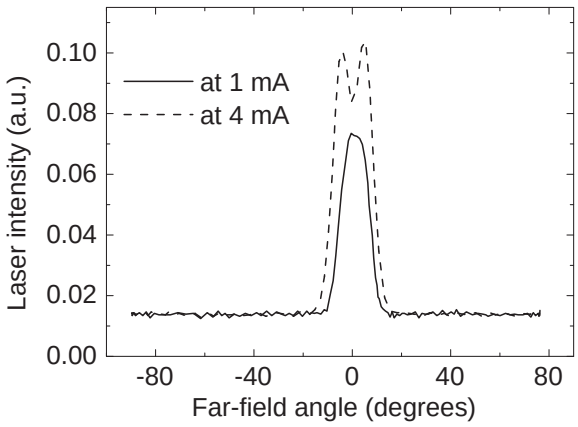

Figure 6.13: Far-field intensities in the direction of the long aperture axis measured as a function of the far-field angle for a VCSEL with an aperture area of 1.5 µm × 8 µm. The currents at which the measurements were done are indicated in the legends.

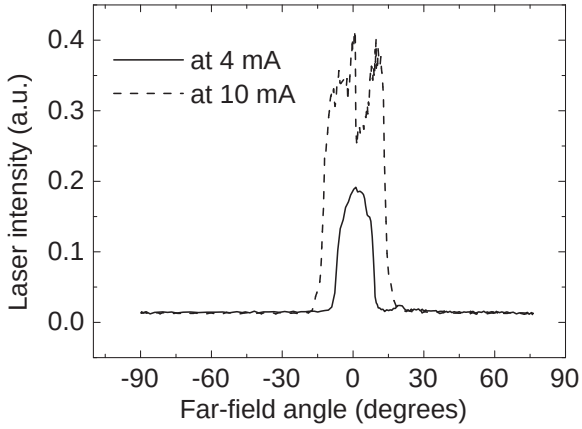

Figure 6.14: Far-field intensities like in Fig. 6.13 for a 1.5 µm × 28 µm size VCSEL at two different currents.

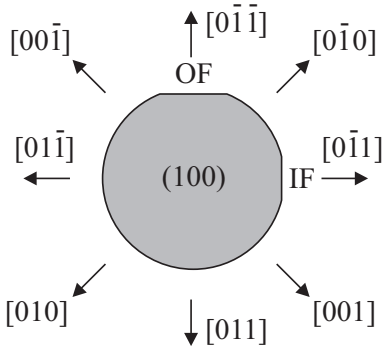

Figure 6.15: Sketch of a (100)-GaAs substrate with orientation flat (OF, also called major flat) and identification flat (IF or minor flat) defining the crystal directions according to the manufacturer. Such crystal direction notation is used throughout the thesis.

GaAs substrates there is a primarily preferred polarization of the output power, which is parallel to the [011] or [01$\bar{1}$] crystal directions even for circular-mesa VCSELs [73]–[75].

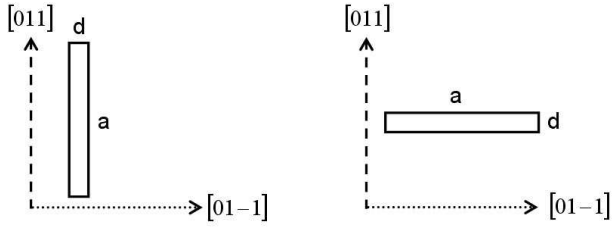

Figure 6.16: Orientation of the aperture length a and aperture width d relative to the crystal directions [011] and [01$\bar{1}$]. Case 1 (left) and case 2 (right).

In order to investigate the dominant polarization mode of the output power in rectangular-shaped VCSELs operating in the multi-mode regime, we refer to Fig. 6.16. There are two cases. In case 1, the aperture length is oriented parallel to the [011] crystal direction and the aperture width is oriented parallel to the [01$\bar{1}$]-crystal direction (Fig. 6.16 (left)). In case 2, the aperture length is oriented parallel to the [01$\bar{1}$] crystal direction and the aperture width is [011]-oriented (Fig. 6.16 (right)). Figure 6.17 shows polarization-resolved LIV characteristics of the normal rectangular-shaped VCSELs for case 1. A common feature of these characteristics is that the dominant polarization of the output power is along the aperture length (along the [011] crystal direction) for all tested aperture dimensions. Polarization-resolved LIV characteristics for case 2 are depicted in Fig. 6.18. As seen in the top right, bottom left, and bottom right graphs, a change of the dominant polarization content occurs. Before this change, the dominant mode is parallel to the [011] crystal direction. After that, the dominant mode is along [01$\bar{1}$]. In contrast, for the active aperture of 1.5 µm × 89.5 µm (top left), no polarization switching occurs and the dominant polarization mode is along the [01$\bar{1}$] crystal direction. Hence, in order to obtain a constantly dominant polarization of a VCSEL with rectangular-shaped aperture, it is crucial that the major aperture axis be oriented along the [011] direction. In addition, these rectangular-shaped VCSELs can be used to distinguish

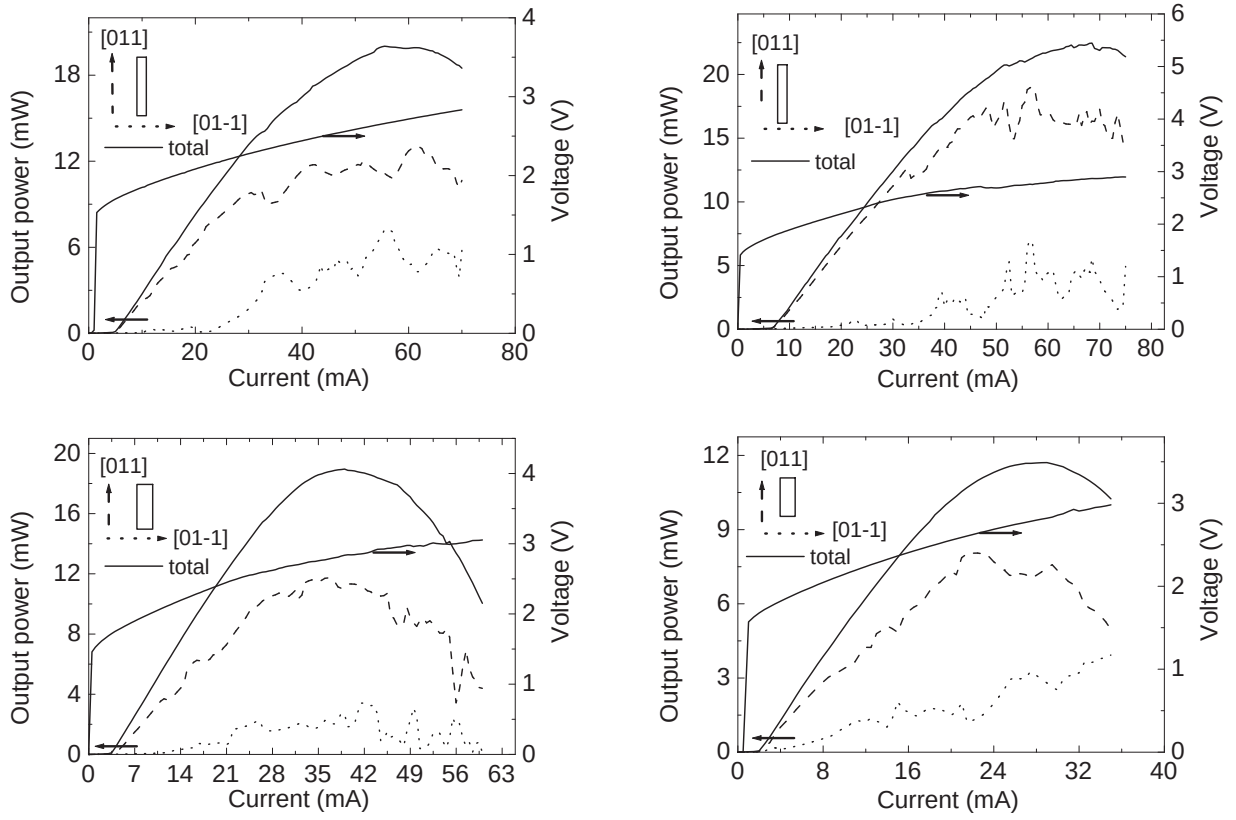

Figure 6.17: Polarization-resolved LIV characteristics of standard rectangular-shaped VCSELs with aperture areas of 2 µm × 86 µm (top left), 4 µm × 86 µm (top right), 4 µm × 46 µm (bottom left), and 4 µm × 26 µm (bottom right). The aperture length is along the [011] crystal direction.

the [011] crystal direction from the [01$\bar{1}$] crystal direction. This can be done by measuring the LI characteristics of case 1 and case 2.

6.2 Multi-Spot Surface-Etched Single-Mode Rectangular-Shaped VCSELs

In this section, the characteristics of single-mode multi-spot surface-etched VCSELs are introduced. Different patterns are applied to induce single-higher-order transverse mode emission using a shallow etching technique. A micrograph with a top view of such a fully-processed rectangular-shaped VCSEL is shown in Fig. 4.2. In the figure, eight spots are applied to stimulate the E_{81} mode.

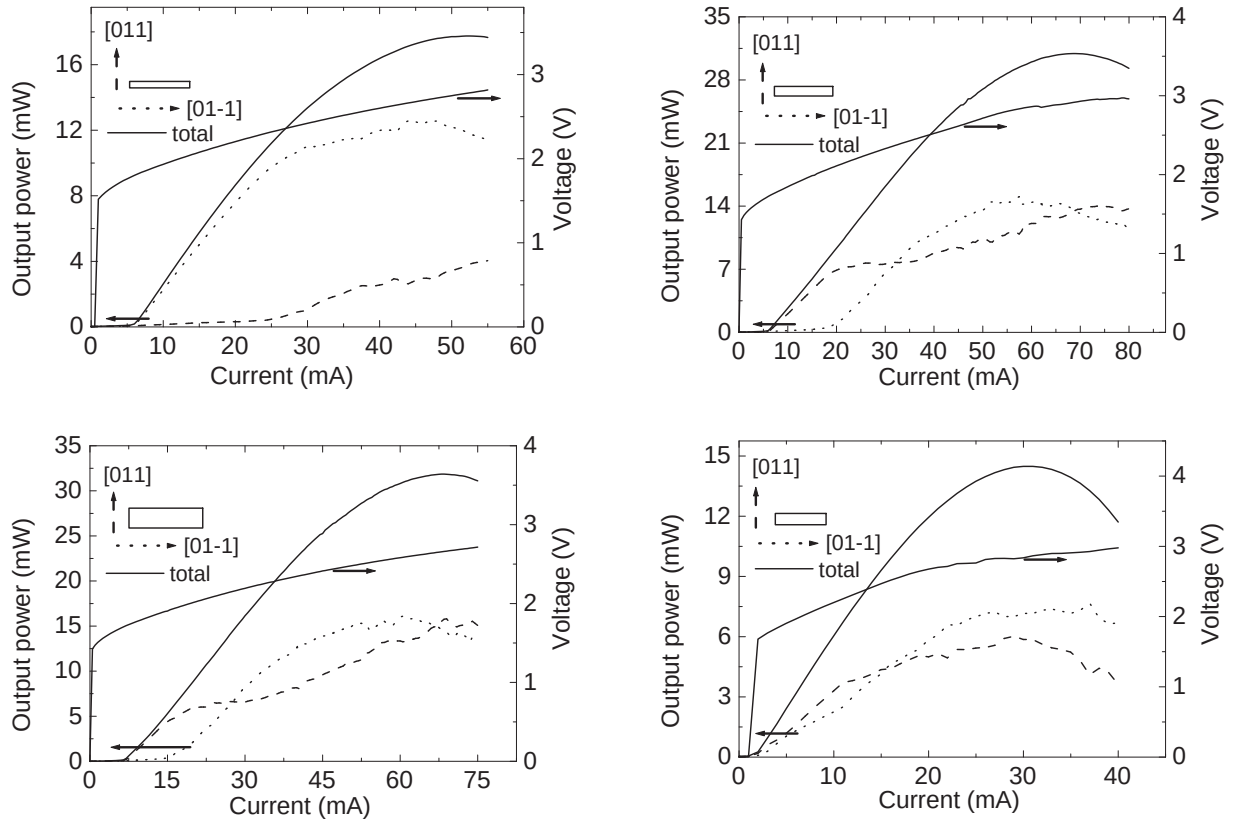

Figure 6.18: Polarization-resolved LIV characteristics of normal rectangular-shaped VCSELs with aperture areas of 1.5 µm × 89.5 µm (top left), 3.5 µm × 89.5 µm (top right), 7 µm × 68 µm (bottom left), and 3.5 µm × 49 µm (bottom right). The aperture length is along the $[01\bar{1}]$ crystal direction.

6.2.1 LIV Characteristics and Spectra

Figure 6.19 shows LIV characteristics of a VCSEL with an 8-spot surface etch, each spot diameter is 6 µm and the active aperture area is 6.3 µm × 68.3 µm. The calculated threshold gains inside and outside the spot are $g_{\mathrm{in}} = 1401\,\mathrm{cm}^{-1}$ and $g_{\mathrm{out}} = 6318\,\mathrm{cm}^{-1}$, respectively (structure 2 in Sect. 4.3). The 8-spot surface etch has been designed to force the transverse mode E_{81} to lase in single-mode operation. Let us refer to this laser as device 1. Its threshold current is 12.8 mA, which is higher than that of a standard rectangular-shaped VCSEL having the same aperture dimension due to reduction of the reflectivity of the p-DBR caused by selective etching of the antiphase layer. The output power at rollover emitted from device 1 is 12 mW, which is a record for CW single transverse mode VCSELs operating at room temperature using the shallow etching technique [76]–[78]. The differential quantum efficiency of the device is 39.5 %. The emitted spectra at different currents are shown in Fig. 6.20. Up to thermal rollover the spectra show single-mode behavior with a side-mode suppression ratio of about 35 dB. Such a laser can be tuned by current or by temperature. The current tuning coefficient is ≈ 0.08 nm/mA. This small current coefficient is of practical

interest when fine-tuning is needed in this range of wavelengths. Such red-shift of the laser wavelength is due to the temperature dependence of the Fabry–Perot cavity resonance as discussed before in Sect. 6.1.2.

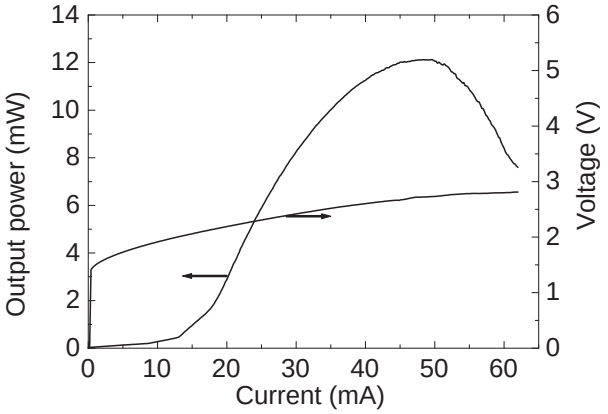

Figure 6.19: LIV characteristics of an 8-spot surface-relief VCSEL with an active aperture area of $6.3 \times 68.3\,\mu m^2$.

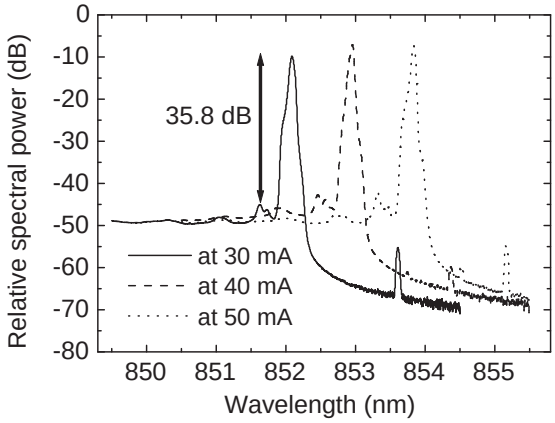

Figure 6.20: Spectra of the VCSEL from Fig. 6.19 at different currents.

Figure 6.21 shows the LIV characteristics emitted from a reference device (rectangular-shaped VCSEL without pattern) having the same aperture size. It has a laser threshold current of 7 mA, a maximum output power at thermal rollover of 34 mW, and a differential quantum efficiency of 51 %. All these parameters are better than those of the corresponding surface-relief VCSEL. However, the spectral purity of the standard device is very "poor". Figure 6.22 shows emitted spectra. From the graph it is obvious that a lot of transverse modes are oscillating in the standard device.

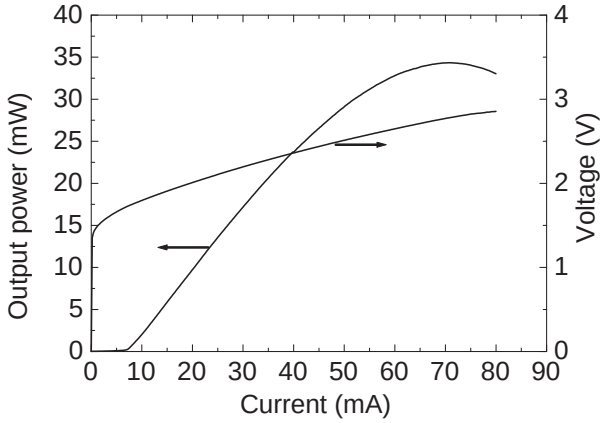

Figure 6.21: LIV characteristics of a standard VCSEL with $6.3\,\mu m \times 68.3\,\mu m$ aperture area.

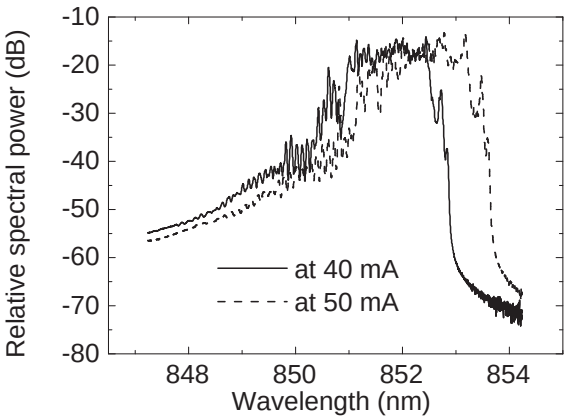

Figure 6.22: Spectra of the VCSEL from Fig. 6.21 at different currents.

Two additional patterns have been designed to force the $E_{10\,1}$ and E_{41} modes to lase in single-mode operation. The LIV characteristics of a 10-spot rectangular-shaped VCSEL designed to

stimulate the $E_{10\,1}$ mode are shown in Fig. 6.23. The active aperture area is 6.3 µm × 68.3 µm and the spot diameter is 5 µm. This laser is referred to as device 2. The decrease of the relief diameter from 6 µm in device 1 to 5 µm in device 2 leads to an increase of the laser threshold as well as a decrease of the emitted power. The laser threshold from Fig. 6.23 is ≈ 16.7 mA and the thermal rollover output power is ≈ 10 mW. The spectra measurements of this device show that it works in single-mode operation. Figure 6.24 demonstrates the emitted spectra at different laser currents. At 30 mA, the device shows an SMSR of 37 dB. The current tuning coefficient is ≈ 0.08 nm/mA.

The LIV characteristics of a 4-spot rectangular-shaped VCSEL designed to stimulate the E_{41} mode are shown in Fig. 6.25. The active aperture area is 6 µm × 30 µm and the relief diameter is 4 µm. The laser threshold current is ≈ 9.6 mA and the maximum output power is 4 mW. The device shows single-mode behavior as indicated in Fig. 6.26.

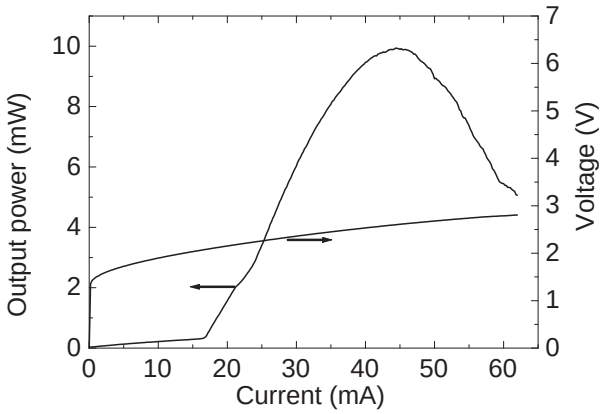

Figure 6.23: LIV characteristics of a 10-spot surface-etched VCSEL. The active aperture area is 6.3 µm × 68.3 µm .

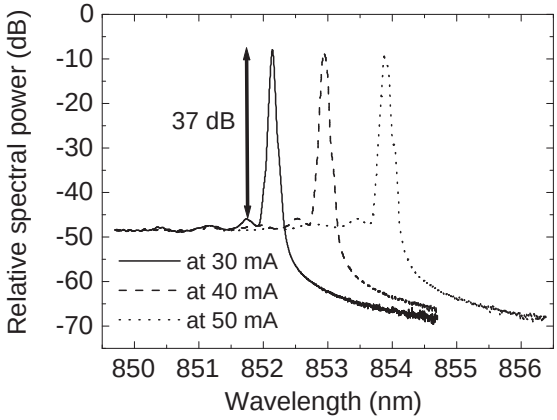

Figure 6.24: Spectra of the VCSEL from Fig. 6.23 at different currents.

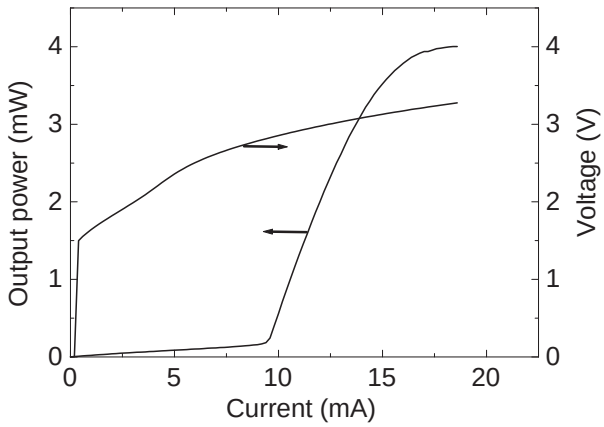

Figure 6.25: LIV characteristics of a 4-spot surface-etched VCSEL with 6 µm × 30 µm aperture area.

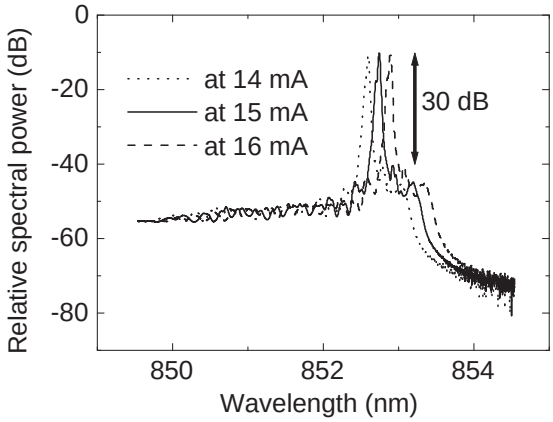

Figure 6.26: Spectra of the VCSEL from Fig. 6.25 at different currents.

Effect of Aperture Increment on LIV Characteristics

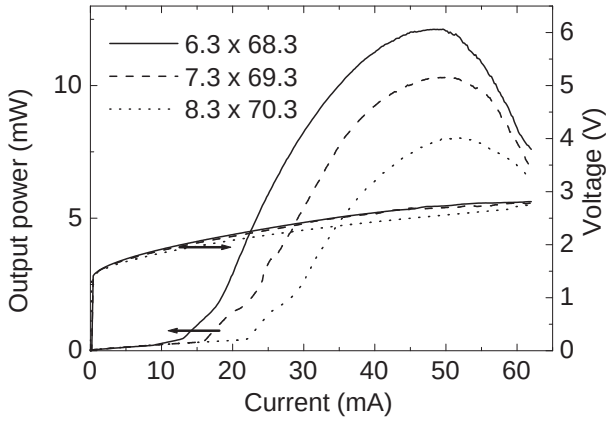

Figure 6.27: LIV characteristics of 8-spot surface-etched rectangular-shaped VCSELs with different size. The aperture areas in μm^2 are indicated in the graph.

Amongst the most critical processes in multi-spot single-mode rectangular-shaped VCSELs is the oxidation rate control. For this reason, different mesa sizes were designed such that the difference between them is 1 µm ×1 µm to tolerate the error in the expected oxidation rate. The surface relief remains at the same position. However, the single mode operation is strongly affected with this increment in the active aperture area. Figure 6.27 shows the LIV characteristics of VCSELs with different aperture areas in the same unit cell. As the aperture area increases from 6.3 µm × 68.3 µm to 8.3 µm × 70.3 µm, the laser threshold increases from 12.7 mA to 22 mA and the maximum output power at thermal rollover decreases from 12 mW to 8 mW. The decrease in the output power with increasing the aperture area is due to the decrease in the overlap between the relief pattern and the active aperture (see Fig. 4.16) in Sect. 4.3. In addition, as the active aperture area increases, the threshold gain also increases (see Sect. 4.3, Fig. 4.17).

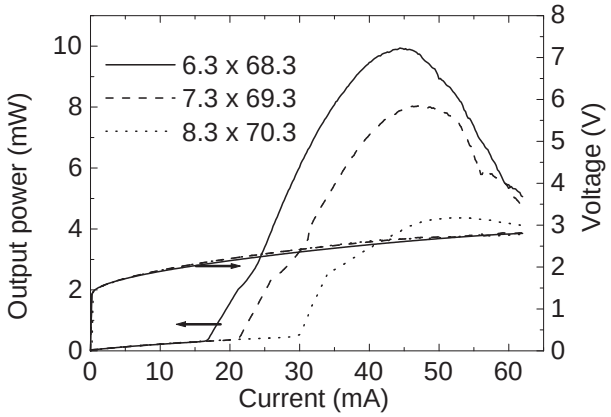

Figure 6.28: LIV characteristics of a 10-spot surface relief rectangular-shaped VCSELs with different aperture areas. The aperture areas are indicated in the legend.

For device 2, similar characteristics were observed. Figure 6.28 shows the LIV characteristics

for different active aperture areas. The maximum output power of the device at thermal rollover decreases from 10 mW to 4 mW as the aperture area increases from 6.3 µm × 68.3 µm to 8.3 µm × 70.3 µm. For the same increment, the threshold current increases from 17 mA to 30 mA. Moreover, there are kinks in the light–current curves due to polarization instabilities. The modal gains of the two orthogonal polarizations are a function of the laser wavelength and the heat dissipation [79]. As the current increases, the dissipation of heat increases too. This leads to a change in the modal gains of the two orthogonal polarizations [79]. From this section, it is concluded that the bottle-neck of enhancing the laser performance of multi-spot shallow-relief single-mode VCSEL is the controlling of oxidation process. Once it is controlled accurately, the laser threshold and the maximum output power at thermal rollover can be optimized.

6.2.2 Statistical Investigations

Since the layer thickness are not the same throughout the wafer, the VCSEL characteristics such as the threshold current and maximum output power at thermal rollover vary from one position on the wafer to another. When the resonator design matches exactly the peak gain in the wafer, the VCSEL threshold is minimum and the extracted output power is maximum. Moreover, as discussed above, the VCSEL characteristics are influenced strongly with the active aperture area. The following are the statistics of an 8-spot surface-etched single-mode VCSEL with different active aperture areas.

- For an active aperture area of 6.3 µm × 68.3 µm, 141 devices were investigated. Concerning the threshold current I_{th}, 27 devices (19.1 %) have $I_{\mathrm{th}} \leq 12\,\mathrm{mA}$, 77 devices (54.6 %) have $12\,\mathrm{mA} < I_{\mathrm{th}} \leq 15\,\mathrm{mA}$, and 37 devices (26.2 %) have $I_{\mathrm{th}} > 15\,\mathrm{mA}$. A maximum output power $P_{\mathrm{max}} \geq 12\,\mathrm{mW}$ is obtained from 26 devices (96.3 %) with $I_{\mathrm{th}} \leq 12\,\mathrm{mA}$, 48 devices (62.4 %) with $12\,\mathrm{mA} < I_{\mathrm{th}} \leq 15\,\mathrm{mA}$, and 9 devices (24.3 %) with $I_{\mathrm{th}} > 15\,\mathrm{mA}$. From these statistics, it is understood that the smaller is the threshold current, the higher is the maximum output power at thermal rollover. For the devices with a low threshold current and a high maximum output power, there is a matching between the resonator design and the peak gain.

- For an active aperture area of 7.3 µm × 69.3 µm, 135 devices were investigated. As mentioned in Sect. 6.2.1, with increasing the active aperture area of multi-spot surface-etched VCSELs, the threshold current increases and the maximum output power decreases. 19 devices (14 %) have $I_{\mathrm{th}} \leq 15\,\mathrm{mA}$, 51 devices (37.8 %) have $15\,\mathrm{mA} < I_{\mathrm{th}} \leq 20\,\mathrm{mA}$, and 65 devices (48.1 %) have $I_{\mathrm{th}} > 20\,\mathrm{mA}$. A maximum output power $P_{\mathrm{max}} \geq 12\,\mathrm{mW}$ is obtained from 14 devices (82.3 %) with $I_{\mathrm{th}} \leq 15\,\mathrm{mA}$, 21 devices (41.2 %) with $15\,\mathrm{mA} < I_{\mathrm{th}} \leq 20\,\mathrm{mA}$, and 2 devices (3 %) with $I_{\mathrm{th}} > 20\,\mathrm{mA}$.

- For an active aperture area of 8.3 µm × 70.3 µm, 131 devices were investigated. 12 devices (9.2%) have $I_{\mathrm{th}} \leq 20\,\mathrm{mA}$, 84 devices (64.1 %) have $20\,\mathrm{mA} < I_{\mathrm{th}} \leq 30\,\mathrm{mA}$, and 35 devices (26.7%) have $I_{\mathrm{th}} > 30\,\mathrm{mA}$. A maximum output power $P_{\mathrm{max}} \geq 10\,\mathrm{mW}$ is

obtained from 7 devices (58.3 %) with $I_{\mathrm{th}} \leq 20\,\mathrm{mA}$ and 54 devices (64.1 %) with $20\,\mathrm{mA} < I_{\mathrm{th}} \leq 30\,\mathrm{mA}$.

6.2.3 Near-Field Results

In order to identify the main mode in the spectra in Fig. 6.20, we have performed spectrally resolved near-field measurements using a fiber with an integrated lens at its tip. The scan area in the near-field is 16 µm × 68 µm. Figure 6.29 shows the near-field intensity profiles emitted from device 1. The near-fields were recorded at a current of 30 mA and show a clear signature of the E_{81} mode. However, the emitted laser intensity from each spot is not the same, due to current density inhomogeneity [49] and temperature inhomogeneity [44] throughout the active aperture. A good image was observed as the distance between the VCSEL and the fiber tip was between 40 and 50 µm. It is worth to mention that when the distance between the VCSEL and the tip of the scanning fiber is below 30 µm, the image is misleading to identify the laser mode. For instance, when this distance is 10 µm, the image is totally confusing and one cannot recognize the laser mode. This effect is understood from the evolution of the phase front of the laser mode. It is both experimentally and theoretically investigated in [59] for a circular-shaped surface relief VCSEL.

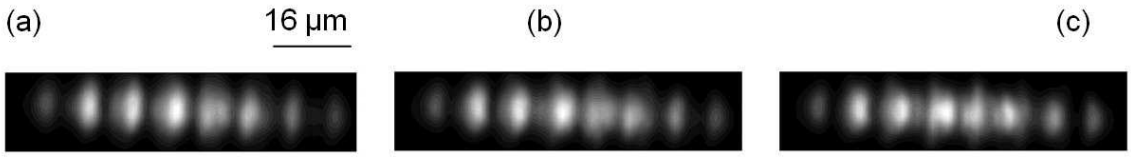

Figure 6.29: Near-field intensity profiles of an 8-spot surface-etched rectangular-shaped VCSEL at different distances from the fiber. The distances are 50 µm in (a), 45 µm in (b), and 40 µm in (c). The applied current is 30 mA. The scan area in the near-field is 16 µm × 68 µm.

In a reference rectangular-shaped VCSEL with the same aperture area (6.3 µm × 68.3 µm), a lot of transverse modes are oscillating. Figure 6.30 shows the measured near-field intensity profiles of some identified transverse modes emitted from this laser. The distance between the tip of the fiber and the laser is 25 µm and the current is 10 mA. The scan distance in this case is reduced due to the higher divergence of this multi-mode VCSEL compared with a single-mode multi-spot surface-etched VCSEL. The fiber scanned an area of 20 µm × 88 µm. The dominant transverse mode among these oscillating modes is $E_{15\,2}$. It is worth noting that no higher-order Laguerre–Gaussian modes [49], [50] were detected. This is attributed to the breaking of the circular symmetry in these rectangular-shaped VCSELs. The modes have the shape of Hermite–Gaussian profiles due to the inherent rectangular resonators of these VCSELs. The transverse mode spacing between $E_{11\,1}$ and $E_{12\,1}$, two successive transverse modes, is 0.028 nm. Note that the transverse mode spacing for an active aperture area of 1.5 µm × 28 µm VCSEL (which is also operating with multi-mode regime) is 0.115 nm (see Sect. 6.1.3). Hence, with increasing the active aperture area, the transverse mode spacing

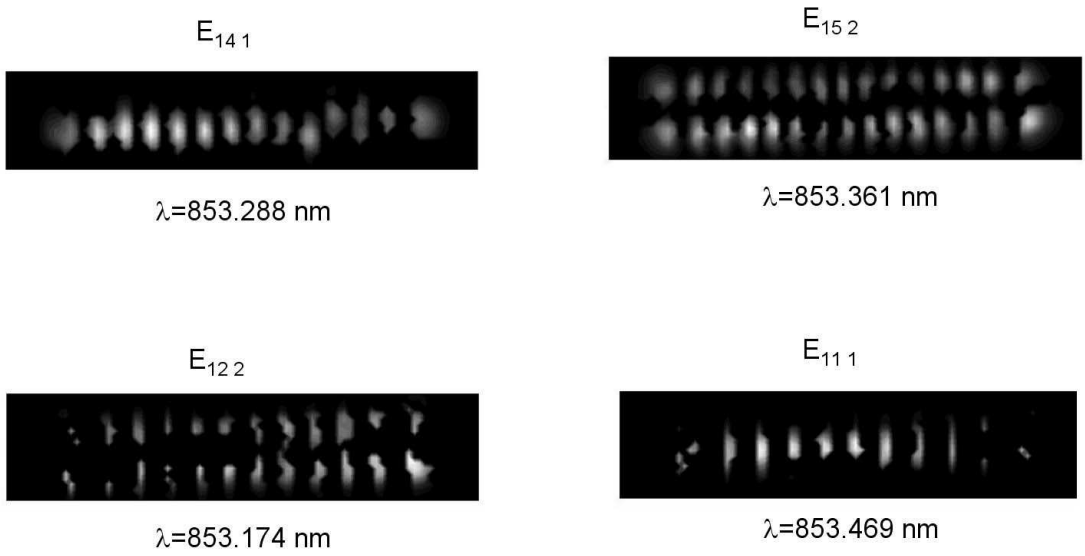

Figure 6.30: Near-field intensity profiles of a standard rectangular-shaped VCSEL with 6.3 µm × 68.3 µm aperture area. The distance from fiber to VCSEL is 25 µm, the fiber scan area is 20 µm × 88 µm, and the driving current is 10 mA.

decreases. From (3.37), it is understood that the smaller is the transverse mode spacing, the higher is the Rayleigh range. The Rayleigh range is a measure for the divergence of the beam. The higher is the Rayleigh range, the smaller is the divergence of the laser beam. Thus, as the aperture area increases from 1.5 µm × 28 µm to 6.3 µm × 68.3 µm, the transverse mode spacing decreases to a fraction of 0.243, indicating an increase of the Rayleigh range by a factor of 4.1.

6.2.4 Far-Field Intensity Measurements

In this section, the measured far-field intensity profiles of multi-spot single-mode VCSELs are reported. Let us analyze the far-field emitted from device 1 (with 8-spot shallow relief). Concerning the far-field intensity in the horizontal direction, there is an interference occurring between the coherent laser spots. The calculated and the measured far-field intensities in the horizontal direction are indicated in Fig. 6.31. For more details about the calculated profile, see Sect. 4.5. Table 6.1 shows the angles at which the peaks occur theoretically θ_{pt} and experimentally θ_{pe} for each order of interference m from (4.8). There is a good agreement between the theoretical and the experimental data.

The main difference between the measured and the calculated far-field intensities is that there is a broadening in the measured far-field compared to the calculated one. This is attributed to current-induced heating. As the current increases, heat will be higher in the center of the aperture compared to its edge. Such a temperature profile will lead to a thermal lensing of the beam in the near-field and hence a divergence of the beam in the far field. Also, calculation assumes equal spot intensities.

Table 6.1: Theoretical and measured angles θ_{pt} and θ_{pe}, respectively at which the interference pattern intensity is maximum for each observed interference order m.

m	θ_{pt} (degrees)	θ_{pe} (degrees)
1	2.72	3.1
2	8.16	8.4
3	13.7	14

The far-field intensity profile obtained from device 1 in the vertical direction is illustrated in Fig. 6.32. The intensity pattern in this direction is given by [64] (see also Sect. 4.5)

$$I(\theta) = I_0(2J_1(\alpha)/\alpha)^2, \tag{6.7}$$

where

$$\alpha = \pi d_{\mathrm{r}} \sin(\theta)/\lambda \tag{6.8}$$

with the relief diameter d_{r}. There is a good agreement between the theoretical and the measured far-fields in the vertical direction, as indicated in Fig. 6.32. The far-field measurement was done at 30 mA current.

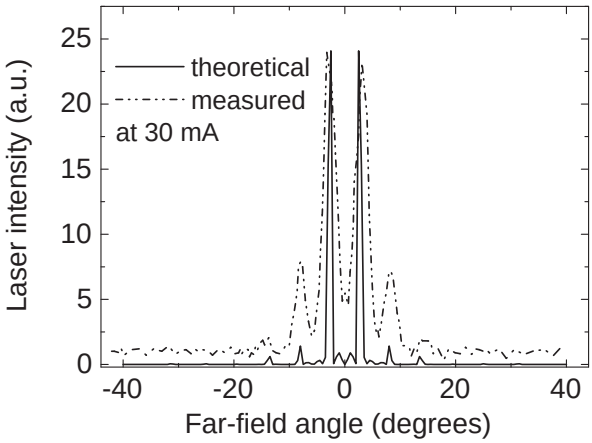

Figure 6.31: Far-field intensity profiles in the horizontal direction for an 8-spot surface relief rectangular-shaped VCSEL with 6.3 µm × 68.3 µm aperture area repeated from Fig. 4.23. The relief diameter of each spot is 6 µm and the pitch is 9 µm. The measurement was done at 30 mA current. Solid and dash-dotted curves are for theoretical and measured far-field intensities, respectively.

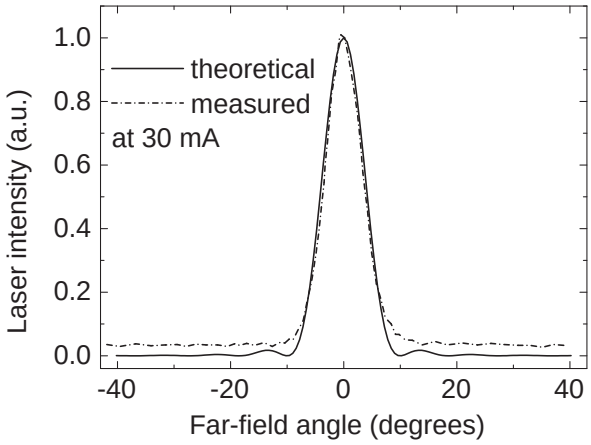

Figure 6.32: Theoretical and experimental vertical far-field profiles corresponding to Fig. 6.31.

Another effect is that with increasing the current, the FWHM divergence angle increases in the vertical direction. Fig. 6.33 shows this effect. At 30 mA the FWHM divergence angle in the vertical direction is 7.75° and at 50 mA the divergence angle is 8.58°. The underlying reason is again thermal lensing, i.e., a decrease of the near-field beam width which is associated with an increase of the far-field angle.

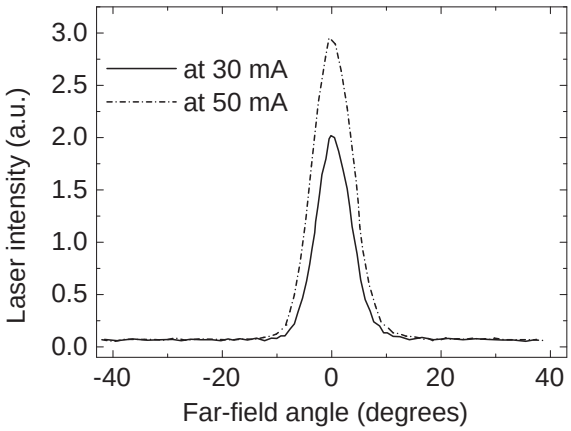

Figure 6.33: Far-field patterns in the vertical direction at 30 mA (solid) and 50 mA (dash-dotted) of an 8-spot surface relief VCSEL.

For device 2 (a 10-spot surface-etched rectangular-shaped VCSEL with a relief diameter of 5 µm for each spot and 7.3 µm pitch), similar characteristics were recorded. Both the decrease of the pitch and of the relief diameter leads to a shift of the peak far-field angles to higher values. Figure 6.34 shows the far-field intensity of the 10-spot VCSEL in the vertical direction. As can be seen, only one lobe is observed. Figure 6.35 shows the measured and calculated far-field intensity profiles in the horizontal direction for device 2. There is a good agreement between the measured and the calculated far-field intensities. The broadening in the measured far-field is attributed to thermal lensing. In addition, with increasing the current, an increase of the FWHM of the far-field is again observed (Fig. 6.36).

Figure 6.37 shows the far-field intensity profile in the vertical direction for a reference rectangular-shaped VCSEL with the same aperture area as that of the 8- or 10-spot surface relief devices. The number of peaks in the vertical direction is two. In the horizontal direction, the device shows a lot of peaks, as seen in Fig. 6.38. This indicates that the device works in the multi-mode regime. With increasing the current, the number of peaks increases, as illustrated in Fig. 6.39.

6.2.5 Polarization-Resolved LIV Characteristics

An important aspect of the radiation emitted from a VCSEL is the polarization state. This has been a research topic for many years since several applications of VCSELs require a stable polarization, such as atomic clocks, laser-based tracking systems [27], and optical interconnects [81]–[84]. Unlike an edge-emitting laser (EEL) which has the transverse electric

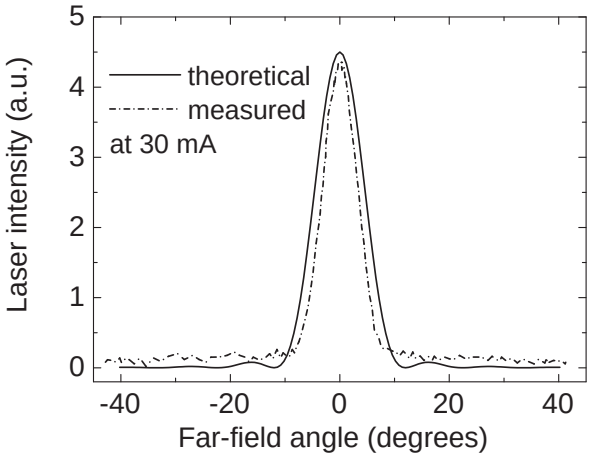

Figure 6.34: Far-field intensity profiles in the vertical direction of a 10-spot surface relief rectangular-shaped VCSEL with 6.3 µm × 68.3 µm aperture area. The relief diameter of each spot is 5 µm.

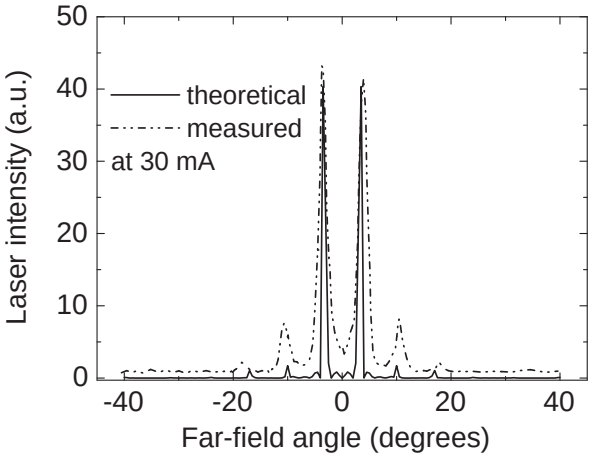

Figure 6.35: Horizontal far-field profiles corresponding to Fig. 6.34. The pitch of the surface reliefs is 7.3 µm.

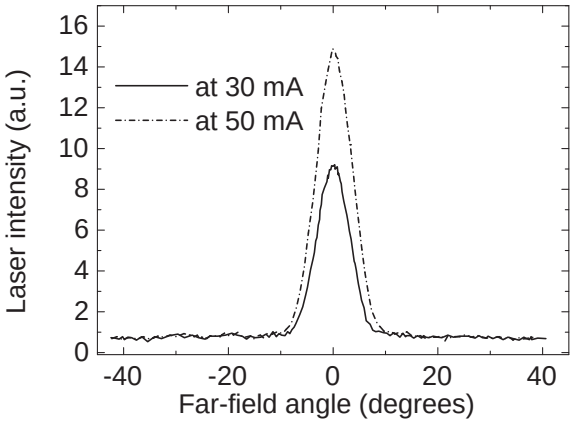

Figure 6.36: Far-field intensity profiles in the vertical direction at 30 mA (solid) and 50 mA (dash-dotted) of a 10-spot surface relief VCSEL corresponding to Fig. 6.34.

(TE) polarization as the dominant one [85], the emitted radiation of an ideal circular-shaped mesa VCSEL grown on a (100)-oriented GaAs substrate has a random polarization in the plane of the quantum wells. However, it has been established that practical VCSELs emit linearly polarized light with a tendency to align with the [011] or [01$\bar{1}$] [86]–[91]. Such preference in polarization is due to an electro-optic effect [86] induced mainly by DBR doping, and due to an elasto-optic effect arising from residual stress during the production process [91], where the optical gain is accordingly influenced by such stress [92], [93]. However, such polarization preference is not stable and switching in the polarization mode can occur due to temperature changes in the device. With respect to applications, polarization control of VCSELs is continuing to be a hot research topic.

Several methods have been considered to produce a single polarization state in a VCSEL

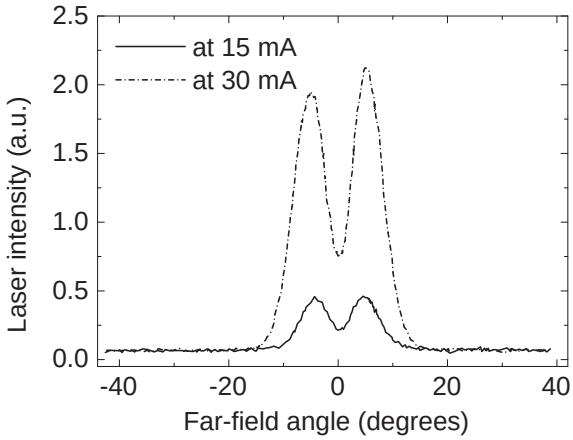

Figure 6.37: Far-field intensity profiles in the vertical direction of a reference rectangular-shaped VCSEL with 6.3 µm × 68.3 µm aperture area at laser currents of 15 and 30 mA.

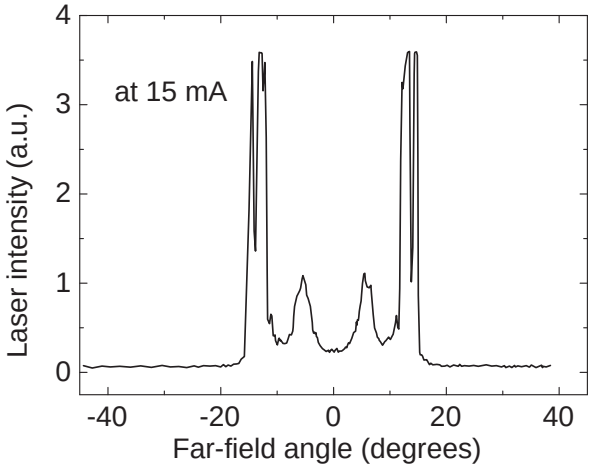

Figure 6.38: Horizontal far-field of the standard VCSEL from Fig. 6.37 at 15 mA current.

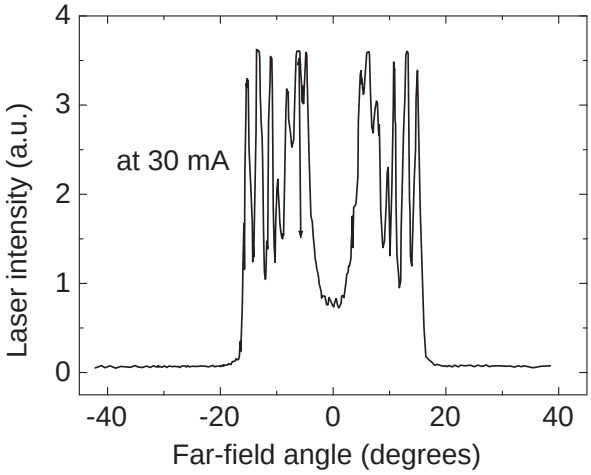

Figure 6.39: Far-field corresponding to Fig. 6.38 at 30 mA current.

[94]–[108]. All of the schemes rely in some manner on breaking the symmetry in the plane of the quantum wells [106] such as by introducing anisotropic gain [94]–[100], or loss [101]–[105] or both [75], [108] or by using an anisotropic transverse cavity geometry [109], [74], [110], [111].

In our case the anisotropic transverse cavity geometry inherent with the oblong-shaped VCSELs has been utilized to select the polarization mode after achieving single transverse mode behavior. In this case, the mirror reflection coefficient for the polarization parallel to the major axis of the cavity is higher than that for polarization parallel to the minor axis. Hence, the threshold gain along the major axis is lower than that parallel to the minor axis [112], [113]. This is valid for both TE and TM modes. Such a phenomenon leads to a single polarization for this device. In addition, the higher is the aspect ratio, the higher is the degree of polarization.

After realizing a single-higher-order transverse mode oscillation of a rectangular-shaped VCSEL, we investigated the polarization of the emitted radiation from the device, and we found the dominance of a single polarization, which is parallel to the major axis of the device. This is in agreement with [112]. In addition, since the aspect ratio of device 1 is about 11, which is large compared to [113], the preference of polarization along the major axis is large. Figure 6.40 shows the polarization-resolved LIV characteristics of device 1. Note that the length of the aperture is along the [011] direction in order to minimize polarization fluctuation of the dominant mode, as described in Sect. 6.1.5. In order to measure the power in a specific polarization, a Glan-Thompson polarizer[1] is inserted in front of the photodetector. From Fig. 6.40, the output power in the polarization parallel to the aperture length at thermal rollover is about 12 mW. This single-mode, single-polarization power value is a record for VCSEL performance. Note that the difference between the total output power and the power in polarization parallel to the aperture length is due to optical losses of the Glan-Thompson polarizer.

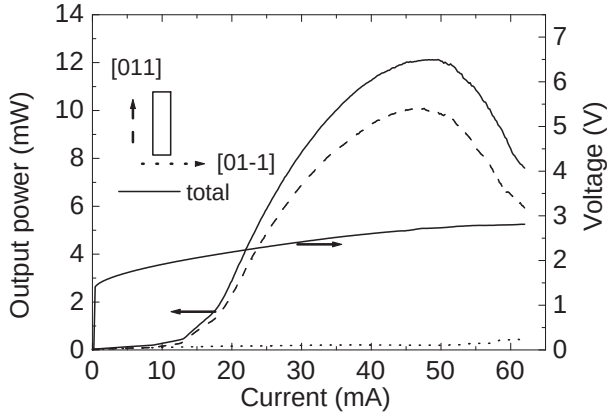

Figure 6.40: Polarization-resolved LIV curves of an 8-spot surface relief VCSEL with 6.3 × 68.3 μm^2 aperture area.

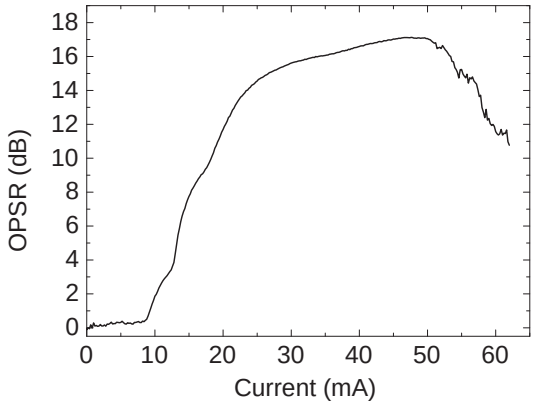

Figure 6.41: OPSR as a function of laser current corresponding to Fig. 6.40.

An important parameter to define the degree of polarization in such a VCSEL is the orthogonal polarization suppression ratio (OPSR). In logarithmic units it is defined as

$$\mathrm{OPSR} = 10\log(\mathrm{P_p}/\mathrm{P_o})\mathrm{dB}, \tag{6.9}$$

where P_p is the output power in the polarization parallel to the aperture length and P_o is the emitted power in the polarization orthogonal to the aperture length. Figure 6.41 shows the OPSR of device 1 derived from Fig. 6.40. At thermal rollover, the OPSR peaks at 17 dB.

An alternative definition of the OPSR is the ratio between the spectral intensities of the polarizations parallel to and normal to the aperture length. In the definition of the OPSR in terms of output powers, one sums over all wavelengths. On the other hand, in the definition of OPSR in terms of spectra measurements, the comparison is restricted to the

[1] B. Halle GmbH, model: PGT 2.12, short version, usable spectral range is 300–2700 nm, 50 dB extinction.

laser wavelength only. At 40 mA and 50 mA, the spectral OPSR in Fig. 6.42 is 25.3 dB and 27.5 dB, respectively. Similar characteristics were recorded for device 2.

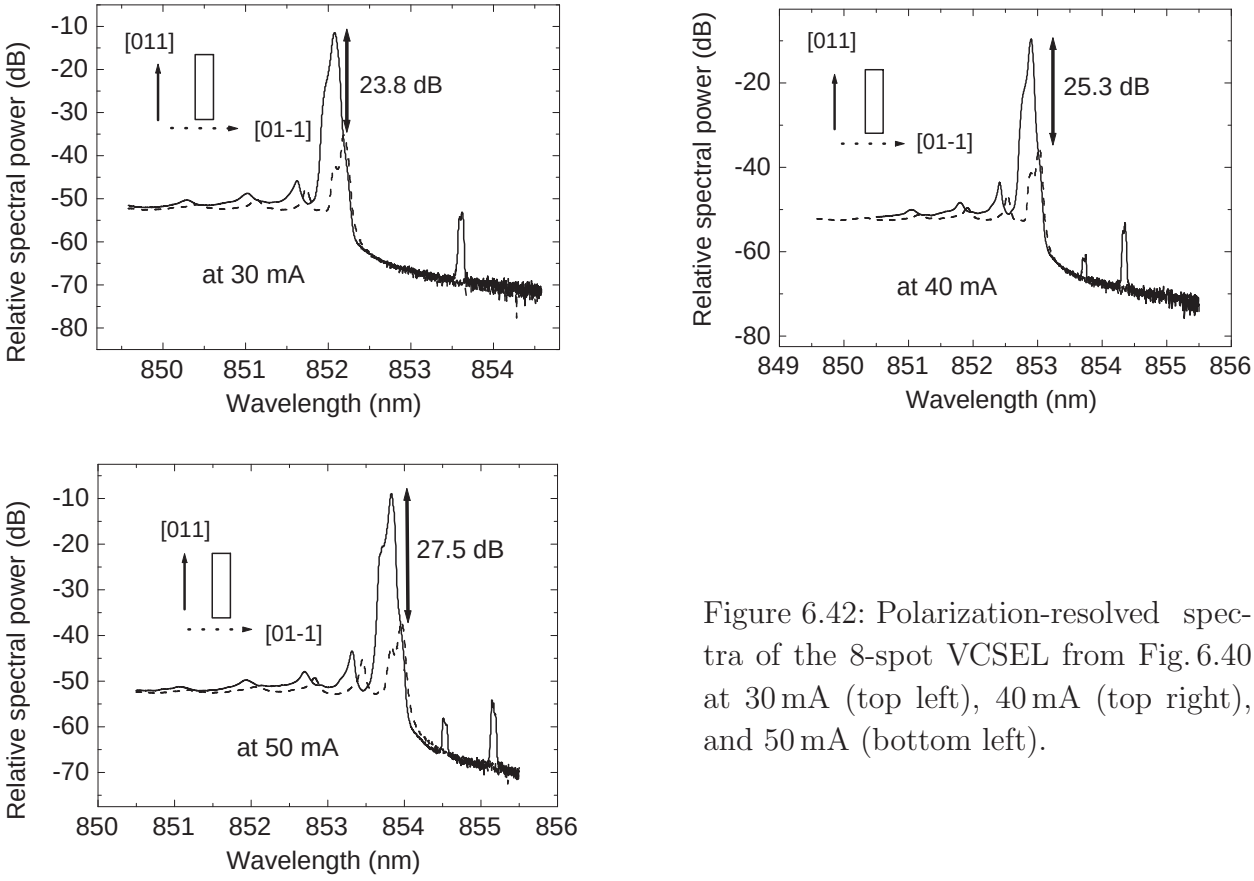

Figure 6.42: Polarization-resolved spectra of the 8-spot VCSEL from Fig. 6.40 at 30 mA (top left), 40 mA (top right), and 50 mA (bottom left).

Figure 6.43 demonstrates its polarization-resolved LIV characteristics. It is worth noting that there is a decrease in the power of the polarization mode parallel to the aperture length at ≈ 24 mA associated with an increase in the power of the polarization mode normal to the aperture length. Also such an effect occurs in the device above the thermal rollover, as shown in Fig. 6.43. This is attributed to the dependence of the modal gain of each polarization mode on the heat dissipation and current [79]. Figure 6.44 shows the OPSR of device 2 as a function of the current. At 40 mA, the maximum OPSR of the device is 16 dB. However, at 24 mA, the OPSR is only around 8.3 dB. The polarization-resolved spectra of device 2 at different currents are indicated in Fig. 6.45. At a current of 40 mA, the spectral OPSR is 29 dB.

Figure 6.46 demonstrates the current-dependent OPSR of an 8-spot rectangular-shaped VCSEL with a slightly larger active aperture area of 8.3 µm × 70.3 µm. The maximum OPSR is 12.5 dB at 37 mA. Consequently, compared to Fig. 6.41, there is a decrease of 4.5 dB as the aperture area increases from 6.3 µm × 68.3 µm to 8.3 µm × 70.3 µm.

A similar behavior was observed for the 10-spot surface-etched rectangular-shaped VCSEL. Figure 6.47 shows its OPSR behavior for a 8.3 µm × 70.3 µm active area. The OPSR at thermal rollover is 11.5 dB. So there is a decrease of 4.5 dB compared to an aperture area of 6.3 µm × 68.3 µm, see Fig. 6.44.

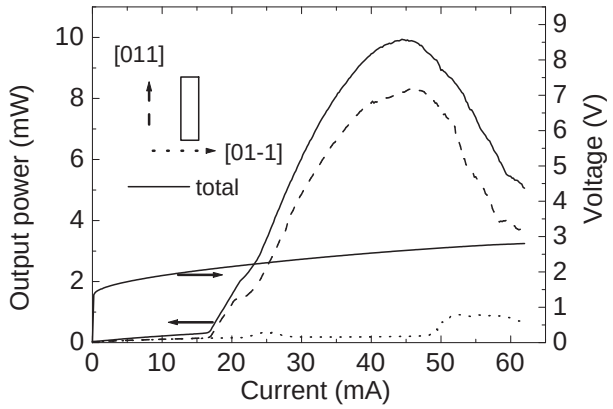

Figure 6.43: Polarization-resolved LIV curves of a 10-spot surface relief VCSEL with 6.3 µm × 68.3 µm aperture area.

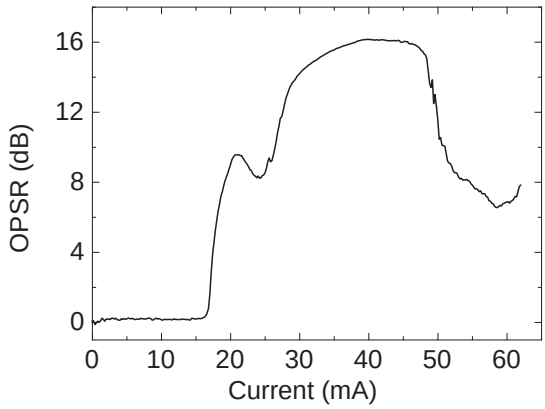

Figure 6.44: Current-dependent OPSR corresponding to Fig. 6.43.

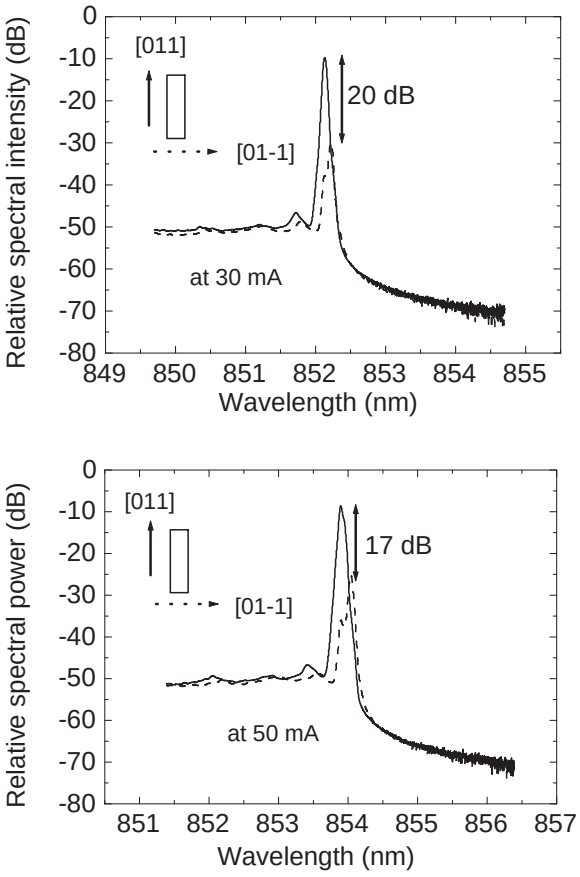

Figure 6.45: Polarization-resolved spectra of the 10-spot VCSEL from Fig. 6.43 at 30 mA (top left), 40 mA (top right), and 50 mA (bottom left).

6.3 Application of Multi-Spot Surface-Etched VCSELs in Optical Manipulation

Optical manipulation of micrometer-sized particles has attracted much interest in the field of biophotonics. By non-mechanical means, the radiation force is used to transport or sort particles or biological cells [114], [23]–[25]. In addition, it can be used to study the mechanical

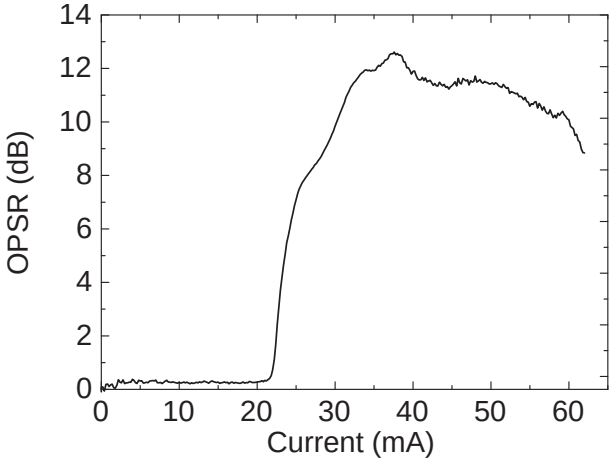

Figure 6.46: OPSR versus current of an 8-spot surface relief VCSEL with a 8.3 µm × 70.3 µm aperture area.

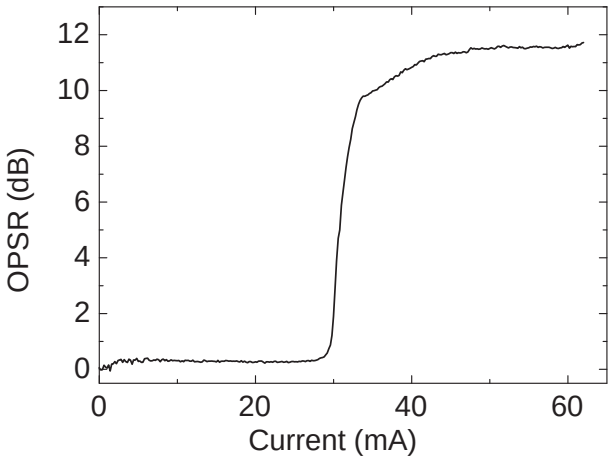

Figure 6.47: OPSR dependence of a 10-spot surface relief VCSEL with a 8.3 µm × 70.3 µm aperture area.

and spectral properties of biological materials such as DNA or cells [115]. The mechanism of these optical manipulations is based on the momentum transfer from the laser source to the transparent particles [116]. Figure 6.48 shows the near-field intensity emitted from an 8-spot relief rectangular-shaped VCSEL. The oscillating laser mode is E_{81} since there are 8 maxima in the horizontal y-direction and 1 maximum in the vertical x-direction; the inset in Fig. 6.50 shows the coordinates. Here, this single-higher-order transverse mode is utilized for optical manipulation of micrometer-sized particles.

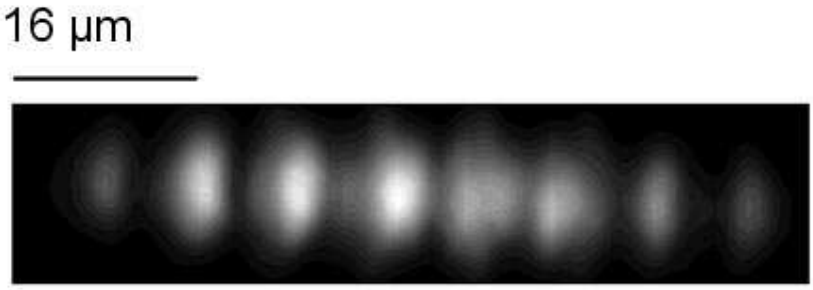

Figure 6.48: Near-field intensity profile of an 8-spot surface relief rectangular-shaped VCSEL.

Figure 6.49 shows a sketch of the setup used for optical manipulation. The VCSEL is at a fixed position and contacted to a current source. The emitted radiation from the VCSEL is then collimated and focused by means of high numerical aperture (NA) lenses so that the focus of the beam is located at the sample plane, wherein polystyrene particles are moving in a liquid. In order to control the position of the focus of the beam relative to the particles, the sample is connected to computer-controlled micropositioning system. The CCD camera with a beamsplitter and a white light source are used to observe the experiment. An infra-red (IR) cutoff filter is utilized to prevent the laser to reach the CCD camera so that the laser is not visible in the image.

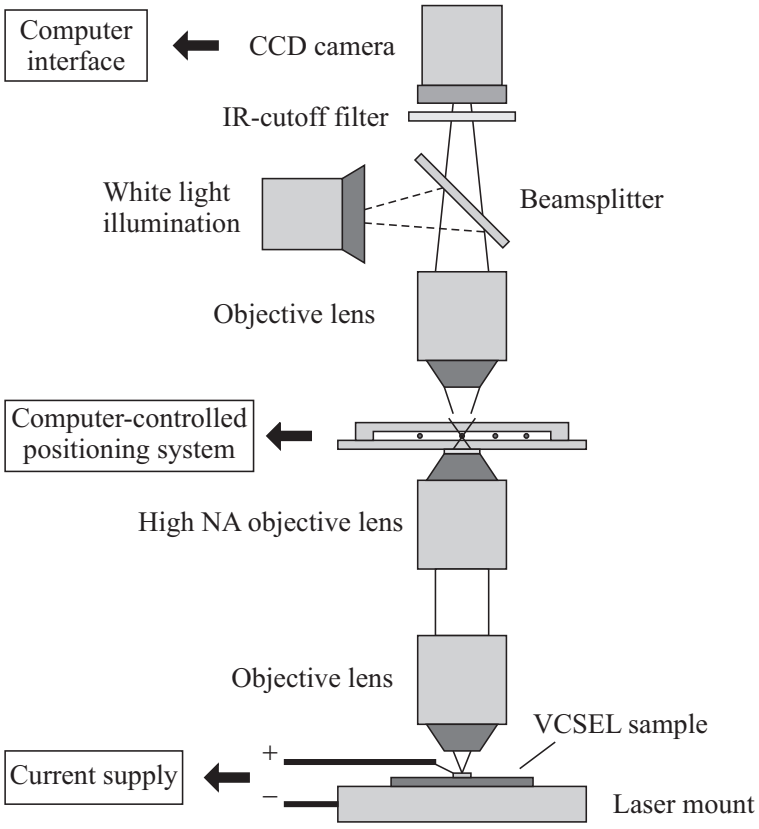

Figure 6.49: Sketch of optical tweezers setup for micro-particle manipulation.

An example for manipulation with such a VCSEL is trapping of particles. Figure 6.50 shows the trapping of two polystyrene particles. The insets in the figure demonstrate the coordinates and the orientation of the VCSEL in the experiment. At the beginning, the particles are moving in the xy-plane with a velocity of about 10 µm/s, where one particle is behind the other, as indicated in snapshot a) in Fig. 6.50. Then the first particle is attracted to the laser beam due to the gradient force, as demonstrated in snapshot b). Then the trapped particle is lifted up in z-direction by the scattering force, corresponding to snapshot c). Afterwards, the second particle is also attracted to the laser and aligned under the first particle, as depicted in d). This trapping was recorded at an output power of 10 mW.

Another example for optical manipulation is deflection. Figure 6.51 shows snapshots of a deflection experiment. One 10 µm polystyrene particle moves in y-direction with a velocity of a few µm/s. It is pulled towards the first laser spot due to the gradient force, as indicated in snapshot a). Since the drag force of the liquid is larger than the trapping force, the particle is not trapped but moves along the next laser spots, as indicated in snapshots b) and c). As the VCSEL is tilted, the particle is deflected from its initial direction. The deflection in x-direction is about 10 µm. This deflection has been shown with an output power of about 6 mW. In a microfluidic channel with a Y-junction, such particle deflections can be employed for all-optical sorting [23].

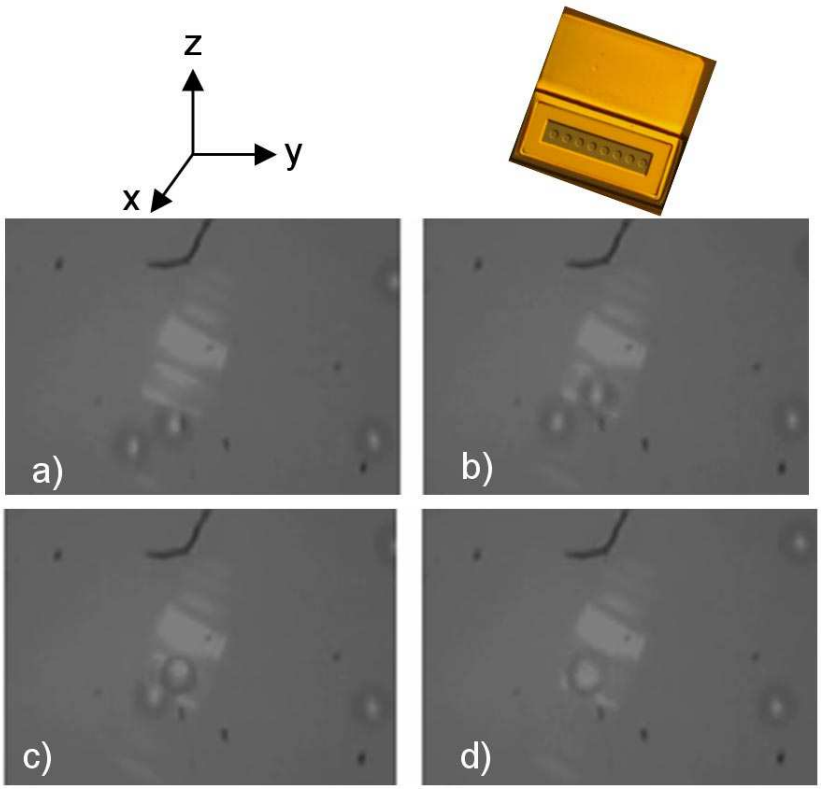

Figure 6.50: Successive optical trapping of two 10 µm diameter polystyrene particles. The insets show the coordinates as well as the orientation of the VCSEL in the experiment.

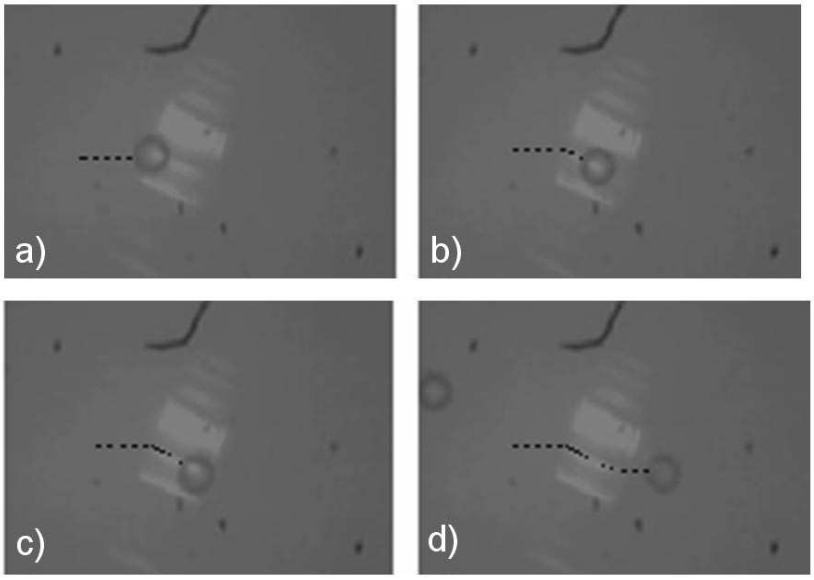

Figure 6.51: Optical deflection of a flowing 10 µm diameter polystyrene particle.

Chapter 7

Experimental Results: Densely Packed Matrix-Addressable VCSEL Arrays

In this chapter, we report on the fabrication and characterization of densely packed top-emitting 4×4 and 16×16 elements wire-bonded matrix-addressable (VCSEL) arrays, which may find future applications such as non-mechanical particle movement with optical multi-tweezers, confocal microscopy or free-space communications with beam steering capability. The factors that control the packing density such as layer structure, mask design and VCSEL processing are investigated aiming to minimize the pitch between VCSELs in the array.

7.1 Introduction

The impressive performance of VCSELs such as low power consumption, circular beam output perpendicular to the wafer surface, on-wafer testing before packaging, and efficient high-frequency modulation is providing the motivation for a continued search for new device types. Such characteristics make VCSELs the ideal light sources for datanet applications [117]. Besides, VCSELs are ideally suited to form two-dimensional arrays of compact optical sources owing to their low threshold currents and high packing density. Such two-dimensional VCSEL arrays are attractive for display technology [118], [119], optical scanners [120], optical interconnects and confocal microscopy [121]. All of these applications require convenient addressing of VCSELs in these arrays. In order to allow operation with high packing density, it is important to decrease the number of contact pads required to address the elements in the array. Figure 7.1 shows how the elements in 4×4 two-dimensional arrays can be addressed using two different architectures. It becomes clear that individual addressing requires a lot of metallic traces. This increases the connection complexity and limits the packing density compared with the matrix addressing scheme. Matrix addressing [122] has the advantage of requiring only $M + N$ contact pads for an $M \times N$ element array, unlike its individually addressable counterpart, which requires $M \times N$ contacts. In addition, when such arrays are

monolithically integrated with resonant-cavity photodetectors [123], this will enable a variety of applications such as high-density interconnects, position sensors, and imaging devices. A recent trend in VCSEL arrays is to obtain a coherent laser emission by utilizing photonic crystal VCSELs [124]–[128] as a potential way to increase the emitted power from a single transverse mode.

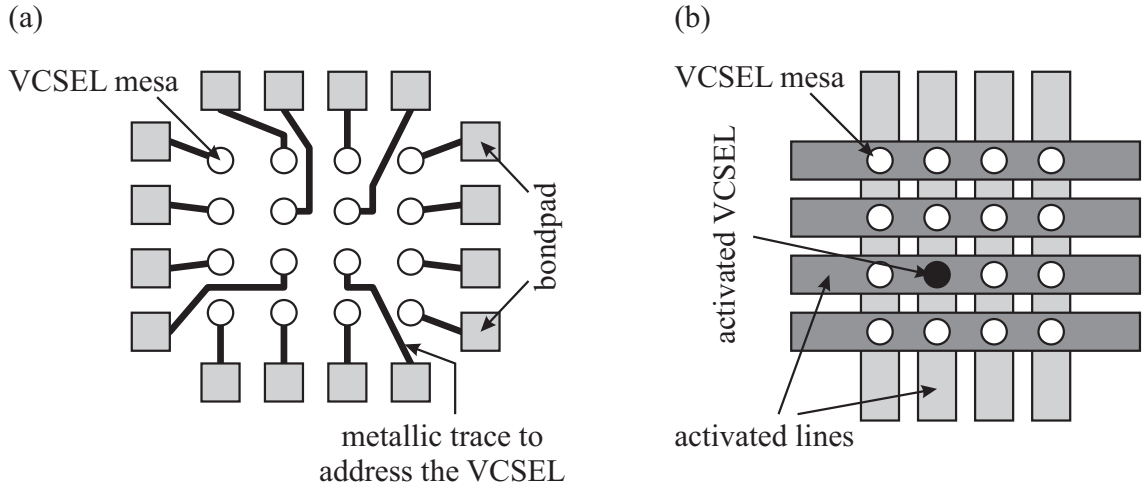

Figure 7.1: Sketches of 4×4 VCSEL arrays with (a) independent addressing and (b) matrix addressing schemes.

7.2 Layer Structure

In order to fabricate matrix-addressable VCSEL arrays, there are some differences in the layer structure compared with common n-contact arrays. For instance, in matrix-addressable arrays the epitaxial structure is grown on an undoped GaAs substrate to allow electrical isolation of columns, in contrast to the common n-contact scheme, which requires an n-doped GaAs substrate. Above the undoped GaAs substrate, there is a thick heavily n-doped GaAs layer to allow n-metalization. In the first generation of our manufacturing of matrix-addressable VCSEL arrays, the thickness of this buffer layer was 2 µm and the doping level was 1.7×10^{18} cm^{-3}. In the second generation these values were increased to 2.5 µm and 6×10^{18} cm^{-3}. Both the increase in the thickness and doping level enhance the electrical properties of the arrays, or in other words, decreases the column resistance. However, such increase in both the doping level and thickness of the buffer layer is limited by the epitaxial growth, i.e., there is a trade-off between the enhancement of the electrical properties of the array and the quality of epitaxial growth.

The n- and p-type DBRs consist of 38.5 Si-doped $Al_{0.2}Ga_{0.8}As/Al_{0.9}Ga_{0.1}As$ DBR pairs and 23 C-doped $Al_{0.2}Ga_{0.8}As/Al_{0.9}Ga_{0.1}As$ pairs, respectively. The DBRs are graded in composition and doping concentration for minimizing the free-carrier absorption and decreasing the electrical resistance. The active region composed of three 7.9 nm thick GaAs quantum wells (QWs) separated by 9.9 nm thick $Al_{0.27}Ga_{0.73}As$ barriers is positioned in an optical

cavity with a thickness of one material wavelength. The laser emission wavelength using these materials together with the cavity design is in the vicinity of 850 nm. A 32 nm thick AlAs oxidation layer is placed above the QWs. The function of this layer is twofold: When a part of it is oxidized to form the active aperture, not only the excitation current is confined but also optical guiding of the laser radiation occurs. For more details about the epitaxial layer structures that have been processed for manufacturing of matrix-addressable VCSEL arrays, see App. B.

7.3 Fabrication Processes

7.3.1 Wet-Chemical Etching

In the first device generation, we have utilized wet-chemical etching, just to realize the matrix-addressable VCSEL array scheme. Firstly, the VCSEL mesas have been defined by photolithography followed by an etching process. Two different schemes for etching can be utilized, namely wet-chemical etching and dry-etching. The main advantages of wet-etching are low cost, ease of use, and stopping at the buffer layer is easily recognized by observation. However, it cannot provide high packing densities in the VCSEL arrays. Hence, in order to obtain a high packing density it is not possible to use wet-chemical etching, because the mesa side-walls will not be vertical but instead have a slope. In addition, wet-etching causes an undercut of the AlAs layer for long etching times, as indicated in the scanning electron micrograph in Fig. 7.2 (left). This undercut is due to the higher etching rate of this layer compared with that of GaAs/AlGaAs. Such an undercut causes stress in the layer structure and makes planarization difficult. The unit cell in this generation contains 4×4 VCSEL elements. The distance from center to center between two neighboring elements is 120 µm. Etching was done down to the depth of the n-buffer layer. Another etching process is done to separate the columns. This etching extends 1 µm down into the substrate to ensure electrical column separation. After this, selective thermal oxidation of a part of the AlAs layer is done to induce electrical and optical confinement. N-metalization is evaporated above the heavily-doped buffer layer to form the n-columns. Two different masks were designed for this process; one to allow the n-metalization to be deposited throughout the columns, except the VCSEL mesas in the columns and the other is just to allow n-metalization at the ends of the columns which act as n-bondpads. The most challenging process in wet-etched matrix-addressable VCSEL array fabrication is planarization of the arrays after this deep etching. The planarization worked successfully with four polyimide coating steps. Thin polyimide has been utilized to avoid an accumulated thick layer above the mesa top, which can cut the thin evaporated metal and thus prevent current flow through the p-rows. The final step is the evaporation of p-metalization throughout the rows.

7.3.2 Reactive-Ion Etching

In the second generation, we utilized reactive-ion etching (RIE) to define the mesa and separate the columns. This is in order to allow manufacturing of densely packed matrix-addressable VCSEL arrays. Figure 7.2 (right) shows a scanning electron micrograph of the RIE-etched mesa. In this process, a radio frequency power of 35 W has been used and the gas pressure was 9 mTorr. $SiCl_4$ and Ar with gas flow rates of 10 sccm and 6 sccm, respectively have been employed. Etching was done down to the depth of the n-buffer layer. Amongst the most challenging processes for densely packed two-dimensional matrix-addressable VCSEL arrays is the separation of columns. The distance between these columns can be as small as 5 µm and the photolithography resolution is not sufficient for the topology resulting from the first etching process. For this reason, two different pitches have been chosen to guarantee the success of processing. The fabrication was successful when the separation between columns was 12 µm instead of 5 µm. The pitch (distance from center to center of two neighboring VCSEL mesas) is 84 µm. After column isolation had been carried out, oxidation was done. Then, n-metalization was applied on the buffer layer. In order to planarize the etched regions, four polyimide planarization steps were made to allow evaporation of p-metalization through the rows. After this, an 800 nm thick Ni/Au metallic layer was evaporated to serve as bondpads for wire bonding in an integrated chip package. To allow a higher packing density, alternating bondpads have been utilized on all sides of the chip. Figure 7.3 shows a scanning laser microscope top view of a fabricated VCSEL array after wire bonding. A photo of the packaged chip is illustrated in Fig. 7.4.

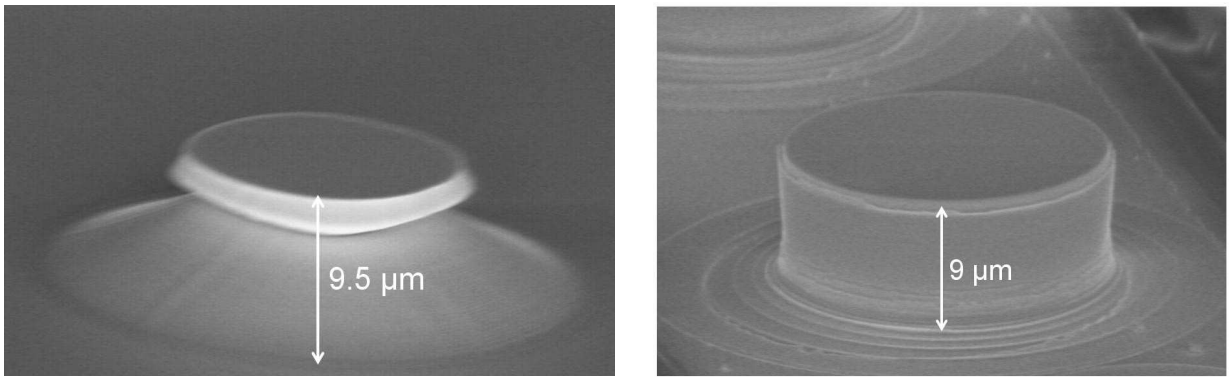

Figure 7.2: Scanning electron micrographs of an etched mesa using wet-chemical etching (left) and reactive-ion etching (right).

7.4 Laser Characteristics

In this section, we will discuss the VCSEL characteristics of both the wet-etched and dry-etched matrix-addressable VCSEL arrays.

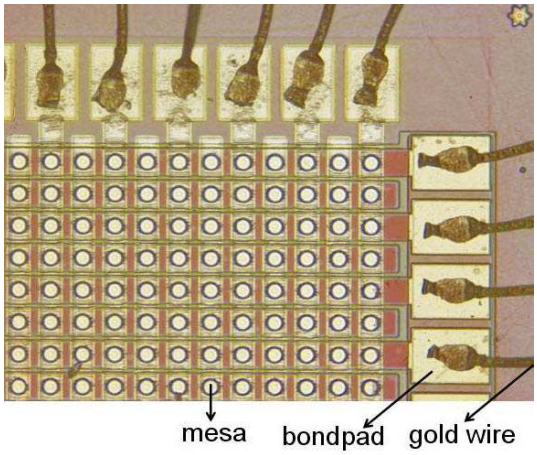

Figure 7.3: Scanning laser micrograph of part of a 16×16 elements matrix-addressable VCSEL array. Dimensions are 84 µm pitch, 36 µm mesa diameter, 64 µm width of the row and column metal tracks, $200 \times 138\,\mu m^2$ bondpad area, and 25 µm diameter of the gold wires.

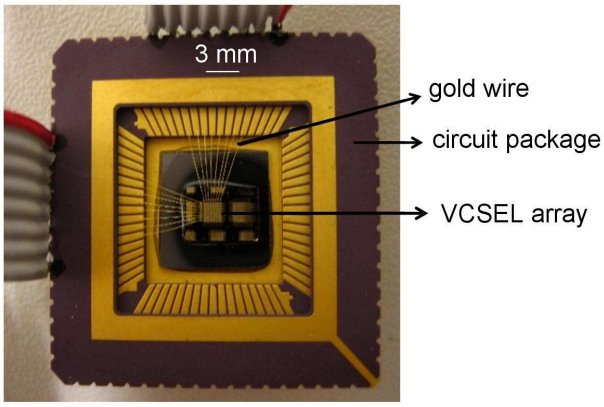

Figure 7.4: Photograph of the packaged and partly wire-bonded VCSEL array. The laser chip size is $1.886 \times 1.88\,mm^2$.

7.4.1 Wet-Etched Arrays

The light–current–voltage characteristics of 15 devices in a fully processed 4×4 elements VCSEL array are displayed in Fig. 7.5. The active diameter of the aperture is 10.8 µm. The threshold current varies from 6.2 mA to 8.7 mA and the maximum output power at thermal rollover is between 4.6 and 5.7 mW except one device, which has 2 mW at thermal rollover. Such variations are due to a gradient in layer thicknesses during crystal growth by the available research-scale molecular beam epitaxy equipment which causes variations in the reflectivities of n- and p-type DBRs and the gain throughout the wafer. One VCSEL within the array shows no lasing operation for unknown reasons. The voltage drop at thermal rollover varies from 3.3 to 3.7 V. A reduction in threshold current was achieved by utilizing a smaller aperture size. Figure 7.6 shows the LIV curves of 15 devices in a fully processed 4×4 elements VCSEL array with an oxide aperture of 6.9 µm. The threshold current now varies

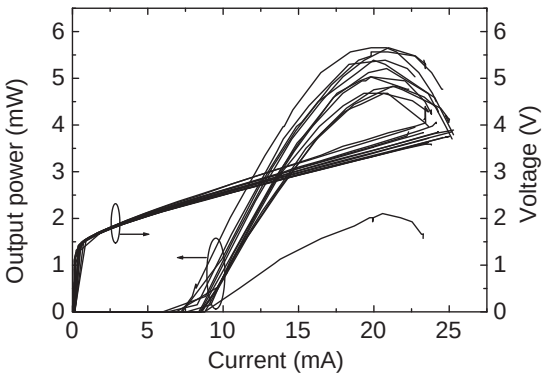

Figure 7.5: LIV characteristics of 15 devices within a processed wet-etched matrix-addressable VCSEL array. The active aperture diameter is 10.8 µm.

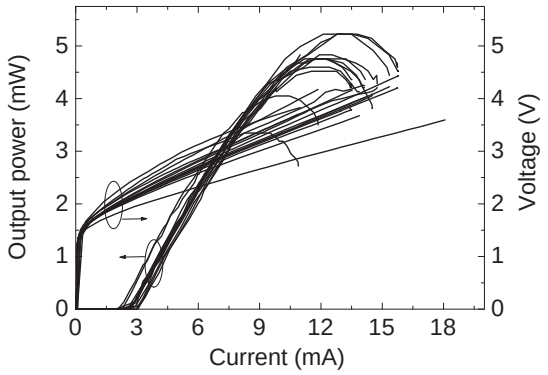

Figure 7.6: LIV curves of 15 VCSELs in an array like in Fig. 7.5, however, with 6.9 µm active diameter.

from 2 to 3 mA, the maximum output power at thermal rollover ranges between 3.3 mW and 5.2 mW, and the corresponding voltage varies from 3 to 4 V. Like before, there is a failure of one of the lasers.

7.4.2 Dry-Etched Arrays

The LIV characteristics of some devices in a fully processed 16 × 16 elements VCSEL array using dry-etching are displayed in Fig. 7.8. The distance between centers of two neighboring VCSELs is reduced to 84 µm using dry-etching instead of 120 µm in case of wet-etching. The active diameter of the aperture is 10 µm. The threshold current varies from 0.5 to 1.6 mA and the maximum output power at thermal rollover is between 2.4 and 4 mW. The difference in voltage drop from one VCSEL to another is due to a change in the parasitic resistance, namely the longer is the distance from the bondpad to the VCSEL, the higher is the corresponding resistance. A simple analysis of this resistance has been done, based on measuring the resistances of the p-row, n-column and the mesa separately using contact needles. These individual components were summed up (since the resistors are connected in series) and compared to the resistances extracted from the current–voltage curves. The contact resistance R_c is taken into account by determining it. Using linear transfer length method [129], sheet resistance R_{sh} and R_c of both n-column and p-row are determined. In this method, the distance d between the contact needles above the p-row or n-column is varied and the corresponding resistance is measured. The measured resistance $R(d)$ is related to R_c and R_{sh} through [129]

$$R(d) = 2R_c + \frac{R_{sh}d}{w} \ , \tag{7.1}$$

where w is the width of column or row. Figure 7.7 shows the measured $R(d)$ versus d for both p-row (squares) and n-column (circles). The solid lines are fitted according to (7.1). From the figure, the extracted contact resistance of p-row and n-column are respectively 0.95 and 1 Ω, and the extracted sheet resistance of p-row and n-column are 0.88 and 1 Ω, respectively.

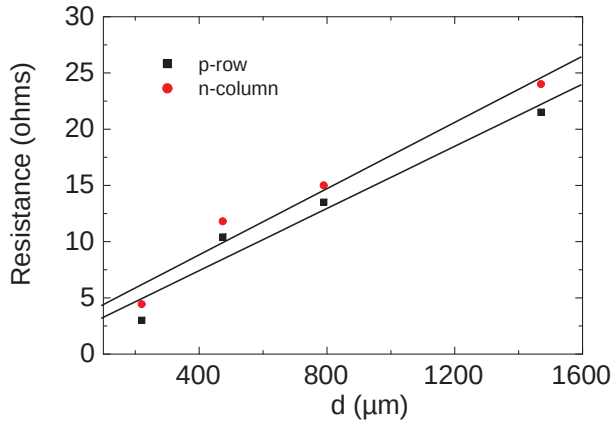

Figure 7.7: Measured p-row resistance (squares) and n-column resistance (circles) versus the spacing between the contact needles . The solid curves are fitted according to (7.1).

In this analysis, the mesa resistance is assumed to be the resistance of the VCSEL when the nearest electrodes are activated minus the contact resistance. The mesa resistance varies throughout the wafer due to different etch depths caused by the gradient in layer thickness. Table 7.1 summarizes the resistances for different mesas.

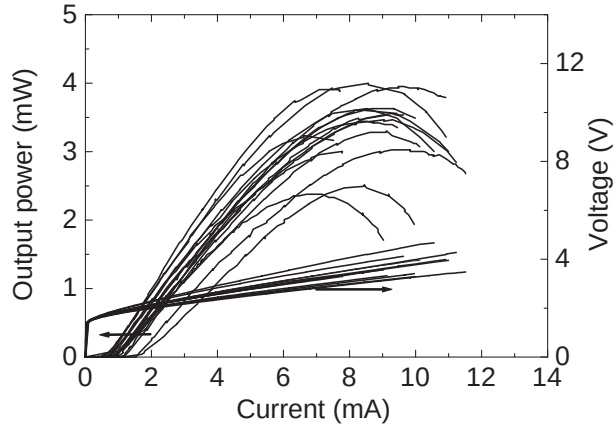

Figure 7.8: Light–current–voltage characteristics of some devices within a processed dry-etched matrix-addressable VCSEL array.

Concerning the spectral purity of the lasers in the array, the spatial filtering technique [130] has been utilized to obtain a single transverse mode. In this technique, the opening of the p-ring contact is small to allow oscillation preferentially of the fundamental mode. Figure 7.9 shows the active aperture and the opening of the p-ring contact using an infra-red microscope. The active aperture is 10 µm and the p-ring opening is 14 µm. Figure 7.10 (top right) shows

Table 7.1: Resistances extracted from the IV curves in Fig. 7.8 and accumulated measured resistances at different positions within the VCSEL array, where the mesa resistance varies.

Resistance from IV curve (Ω)	Accumulated resistance (Ω)	Mesa resistance (Ω)
174	175	127
153	151	103
144	144	96
138	140	92

the spectra at different currents according to the laser characteristics in Fig. 7.10 (top left). Up to 4 mA current only the fundamental LP_{01} mode oscillates. Above this current, the first higher-order LP_{11} transverse mode begins to lase. Figure 7.10 (bottom left) shows the far-fields at different currents. A single peak is observed up to 4 mA, then at thermal rollover two lobes are observed, indicating the onset of the LP_{11} mode.

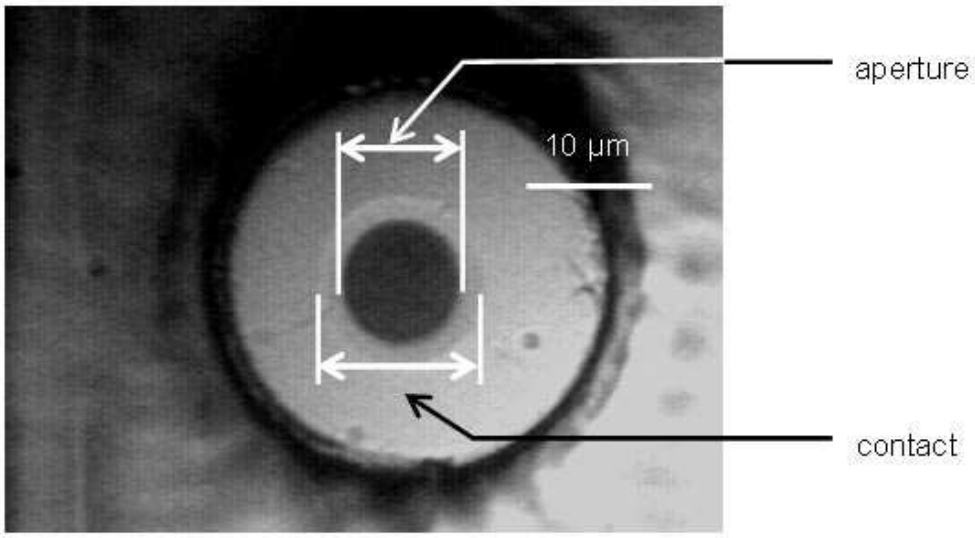

Figure 7.9: Micrograph of a VCSEL in the array in Fig. 7.3 showing the oxide aperture and the p-ring opening. It is recorded with an infra-red microscope.

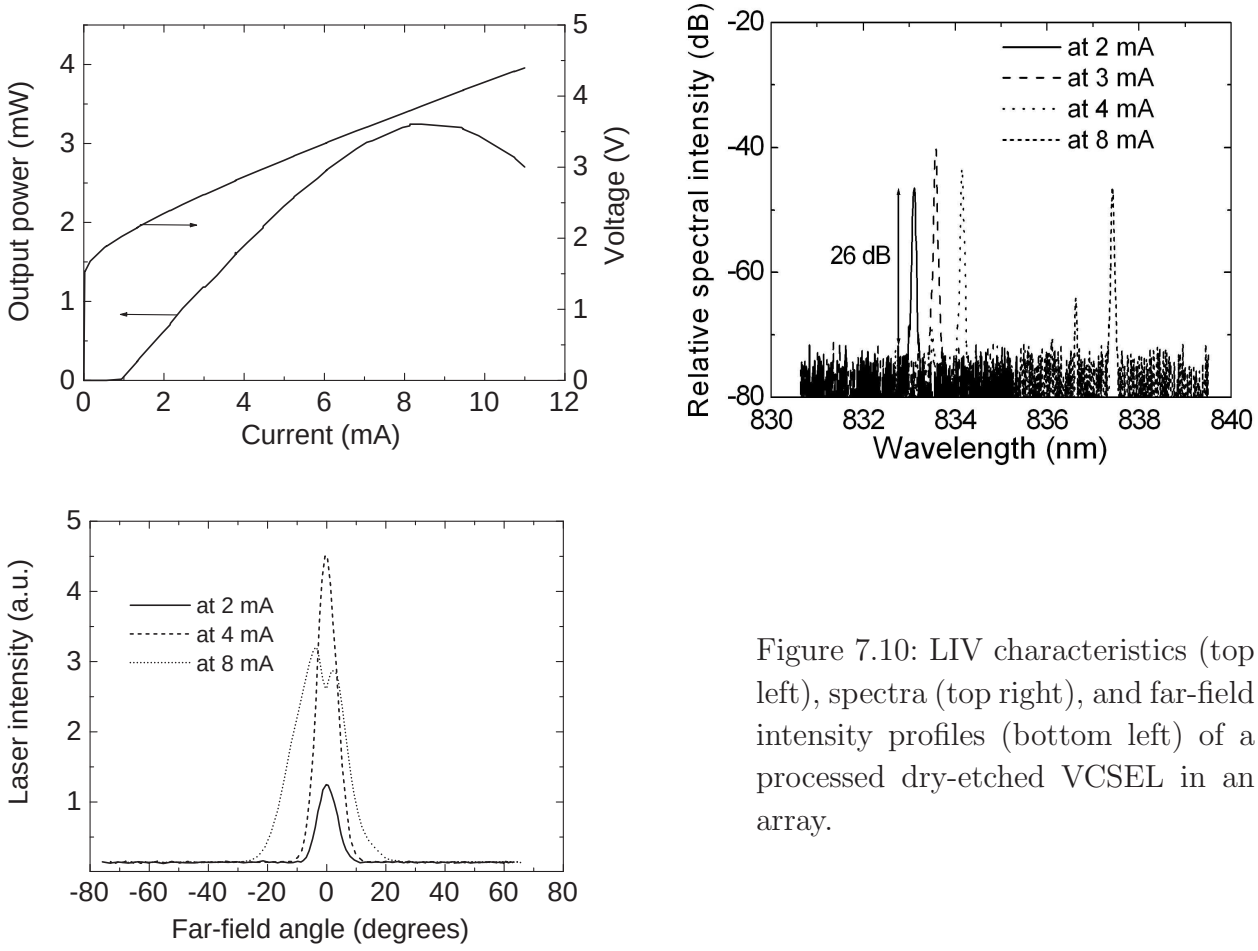

Figure 7.10: LIV characteristics (top left), spectra (top right), and far-field intensity profiles (bottom left) of a processed dry-etched VCSEL in an array.

Chapter 8

Conclusions

The scope of this work is centered around the investigations and improvements of two particular VCSEL concepts. The major part of the thesis deals with mode selection in multi-spot shallow surface relief rectangular-shaped VCSELs. Both theoretical and experimental investigations into this type of VCSEL are introduced in the context of the thesis. The improvements in the performance of this VCSEL such as high-power single transverse mode oscillation and low differential resistance are of practical interest in different applications such as in spectroscopy, sensing and more.

The oscillating transverse mode in the device is a higher-order transverse mode such as E_{81} or $E_{10\,1}$. The technique that has been utilized to select the single mode is based on the inverted shallow relief, where an antiphase layer is added to the topmost layer in order to induce excess loss. In a single processing step, this added layer is selectively etched such that the loss of the desired mode is smaller than that of any other mode. With this technique, in the ideal case, only the desired mode oscillates, and the other modes can not. In addition, the asymmetric transverse cavity produced by the oblong geometry allows selection of a single polarization.

The governing equations that control the operation of a single-higher-order transverse mode in this device are introduced. An interesting application that we show with this device is optical manipulation of micrometer-sized particles such as optical deflection and trapping.

Aside from mode selection in multi-spot shallow surface relief rectangular-shaped VCSELs, we report on densely packed two-dimensional matrix-addressable VCSEL arrays. The design, fabrication and characterization of these arrays emitting in the vicinity of 850 nm are discussed. The main obstacle that limits the packing density of the arrays is the finite resolution in photolithography after deep etching.

The main achievements that we realized in this thesis are summarized in the next two sections.

8.1 Multi-Spot Surface-Etched Rectangular-Shaped VCSELs

The following are the experimental highlights that we achieved using multi-spot shallow-relief rectangular-shaped VCSELs:

- A single-higher-order transverse mode output power of more than 12 mW, emitted in the vicinity of 850 nm, which is the highest single-mode power ever reported using the technique of surface etching (Sect. 6.2.1). The side-mode suppression ratio at thermal rollover exceeds 35 dB (Sect. 6.2.1).
- A single-higher-order transverse mode, single-polarization output power about 12 mW at about 850 nm wavelength, which is the highest single-mode, single-polarization output power ever reported using this technique (Sect. 6.2.5). The spectral peak-to-peak suppression of the orthogonal polarization is 27.5 dB (Sect. 6.2.5).
- A differential resistance of 18 Ω, which is the lowest differential resistance ever reported with a single transverse mode VCSEL (Sect. 6.2.1).

To realize the above mentioned items, it was necessary to investigate theoretically the competition that occurs between the transverse modes. For this reason, we calculated the following parameters as a function of the active aperture area to obtain single transverse mode behavior:

- The three-dimensional confinement factor of each mode (Sect. 4.3).
- The threshold gain of each mode (Sect. 4.3).

These parameters are optimized for the desired mode, i.e., maximum confinement factor and minimum threshold gain for the desired mode compared with all other competitive modes. For this reason, different surface patterns have been used with different relief diameters.

8.2 Matrix-Addressable VCSEL Arrays

Design, fabrication, and characterization of two generations of matrix-addressable VCSEL arrays are reported. The first generation are top-emitting 4×4 elements VCSEL arrays emitting in the vicinity of 850 nm. Wet-chemical etching is utilized to define the mesa and separate the columns in this generation. The pitch is 120 µm. With an oxide aperture diameter of 6.9 µm, the threshold current varies from 2 to 3 mA in a unit cell of the array. The maximum output power at thermal rollover varies from 3.3 to 5.2 mW and the corresponding voltage from 3 to 4 V.

In the second generation, top-emitting 16×16 elements wire-bonded 850 nm range VCSEL arrays are designed, fabricated, and characterized. Reactive-ion etching is utilized to define the mesa and separate the columns in this generation. The pitch is 84 µm and the active aperture of the devices is 10 µm. The threshold current of an element in the array varies from

0.5 to 1.6 mA and the maximum output power at thermal rollover is between 2.4 and 4 mW. Like in the first generation, this variation is due to the gradient in layer thickness caused during molecular beam epitaxial growth. A spatial filtering technique has been used to select the fundamental mode. Far-field measurements are done to show up to which current the emitted radiation is still single transverse mode. From these measurements, it is seen that the VCSELs oscillate in a single mode until around 10 times the threshold current.

Appendix A

VCSEL Processing

A.1 Multi-Spot Surface-Etched Rectangular-Shaped VCSELs

1. Cleaning the Sample

- Clean in acetone for 5 minutes to remove any contaminants, particles and organics.
- Clean in isopropanol (propanol-2) for 5 minutes which dissolves acetone residuals.
- Dry with N_2 to remove water.
- Dry the wafer at 120°C for 10 minutes to remove water residuals.

2. Etching of Multi-Spots

- Spin-coat the resist AZ1512HS on the wafer with 9000 rev/min, program 9, for 40 s.
- Clean the edge of the wafer using edge bead remover.
- Softbake the wafer at 90°C for 10 minutes to make the resist photosensitive.
- Clean the back-side of the wafer using cotton buds and acetone.
- Expose the resist for 16 s with 12 mW/cm^2 using the mask "Relief".
- Dip the wafer for 18 s in AZ400K : H_2O = 1:4.
- Hardbake the wafer at 120°C for 7 minutes, 140°C for 7 minutes, 170°C for 15 minutes to make the resist very stable against the etchant.
- Use O_2 plasma for 2 minutes, 10 % O_2, 33.3 % RF (100 W) to remove the residual resist.
- Prepare citric acid : H_2O mixture with ratio 1:1.
- Add H_2O_2 to the above mixture with ratio 1:30 and mix well to obtain the final etching solution.
- Dip the wafer in HCl : H_2O with ratio 1:1 for 15 s before etching.
- Insert the wafer in the etching solution for about 45 s, the etching rate is about 1.3 nm/s.

3. Passivation of the Mesa

- Dry the wafer at 120°C for 2 minutes.
- Spin-coat the resist AZ1512HS on the wafer with 6000 rev/min for 40 s, program 6.
- Softbake the wafer at 90°C for 10 minutes to make the resist photosensitive.
- Expose at 12 mW/cm^2 for 16 s, mask "Passivation".
- Dip the wafer in the developer AZ400K : H_2O = 1:4 for 18 s.
- Hardbake the wafer at 120°C for 2 minutes.

4. Etching of the Mesa and Oxidation

- Use the wet-chemical etchant H_2SO_4 : H_2O_2 : $H_2O = 1:6:40$ for 3 minutes.
- Check the etch depth in Alpha-Step profilometer and optical microscope.
- Remove the resist by Methyl-Pyrrolidone (MP) at 90°C for 10 minutes.
- Cleave the wafer to prepare a dummy.
- Measure the diameter of the AlAs layer with an infra-red camera to observe its undercut.
- Keep the wafer in the beaker with methanol at 20°C to prevent the oxidation until the oxidation machine is ready.
- Rinse in acetone, then isopropanol for 2 minutes, which dissolves methanol residues.
- Oxidize two dummy samples in the furnace at 400°C for 35 minutes and 40 minutes.
- Calculate the oxidation rate.
- Oxidize the hot wafer for about 40 minutes 40 s in the furnace.

5. N-Metalization

- Clean the wafer with acetone and isopropanol.
- Dip the wafer in HCl : H_2O mixture with ratio 1:1 for about 30 s.
- Evaporate the following materials with these thicknesses: Ge (17 nm), Au (50 nm), Ni (10 nm), Au (50 nm).
- Anneal the wafer up to 400°C for 90 seconds using the rapid thermal annealer.
- Wait until the temperature reaches room temperature.

6. Passivation with Polyimide

- Clean the wafer with acetone and isopropanol.
- Dry the wafer using a hotplate at 120°C for 10 minutes.
- Spin-coat the resist Durimide 7505 on the wafer using 6000 rev/min, 40 s.
- Softbake at 100°C for 2 minutes.
- Expose the wafer with the dose 12 mW/cm^2 for 14 s using the mask "Polyimide".
- Postbake using a hotplate at 100°C for 1 minute.

- Develop the wafer using HTRD2 for 80 s and stop the process using isopropanol for 1 minute.
- Hardbake the polyimide by heat treatment from 100 to 300°C with a rate of 20°C/3 minutes. Then leave the wafer at 300°C for 1 hour, then switch off the hotplate and leave the wafer to cool down for about 1 hour.

7. Bondpad Metalization

- Spin-coat the photoresist TI35ES on the wafer at 4000 rev/min.
- Softbake for 3 minutes at 90°C.
- Expose the wafer to UV light with the dose 12 mW/cm^2 for 48 s with the mask "P-METALS".
- Wait 10 minutes to allow diffusion of nitrogen from the photoresist.
- Reversebake for 2 minutes at 125°C.
- Flood exposure for 2 minutes without mask.
- Develop with AZ 726 MIF for 50 s.
- Stop the reaction by immersing the wafer in H_2O for 30 s.
- Dry the wafer with nitrogen.
- Put the wafer inside the metalization chamber on a rotary wheel.
- Evaporate with Ti (20 nm), Pt (30 nm), Au (150 nm).
- Lift-off process using MP for 30 minutes at 120°C.
- Clean the wafer using acetone and isopropanol.
- Dry the wafer with nitrogen.

A.2 Wet-Etched Matrix-Addressable VCSEL Arrays

1. Cleaning the Sample

- Clean in acetone for 5 minutes to remove any contaminants, particles and organics.
- Clean in isopropanol (propanol-2) for 5 minutes which dissolves acetone residuals.
- Dry with N_2 to remove water.
- Dry the wafer at 120°C for 10 minutes to remove water residuals.

2. Mesa Formation

- Spin-coat with AZ1512HS photoresist using 6000 rev/min, program 6, for 40 s.
- Clean the edge of the wafer using edge bead remover.
- Softbake the wafer at 90°C for 10 minutes to make the resist photosensitive.
- Clean the back-side of the wafer using cotton buds and acetone.

- Expose at 12 mW/cm^2 for 16 s, mask "MESA POS".
- Dip the wafer in AZ400K : H_2O = 1 : 4, for 18 s.
- Hardbake the wafer at 120°C for 2 minutes to make the resist very stable against the etchant.
- Use O_2 plasma for 2 minutes, 10 % O_2, 33.3 % RF (100 W) to remove the residual resist.

3. Wet Etching of Mesa

- Use the wet-chemical etchant H_2SO_4 : H_2O_2 : H_2O = 1 : 6 : 40 for 3 minutes.
- Check the etch depth in Alpha-Step profilometer and optical microscope.
- Remove the resist by MP at 90°C for 10 minutes.

4. Column Isolation

- Clean the wafer using acetone and isopropanol.
- Spin-coat the resist AZnLOF 2070 with 4000 rev/min for 40 s, program 4.
- Clean the edge of the wafer by edge bead remover.
- Softbake the wafer at 110°C for 2 minutes.
- Remove the resist from the back-side of the wafer by acetone.
- Expose the resist for 8 s with 12 mW/cm^2 using the mask "COLUMN ISOL".
- Postbake at 110°C for 90 s.
- Dip the wafer in AZ826MIF for 110 to 115 s.
- Use O_2 plasma for 2 minutes 30 s, 10 % O_2, 0.1 Torr, 33.3 % RF (100 W).
- Hardbake the wafer at 110°C for 1 minute.
- Use the etchant $H_2SO_4 : H_2O_2 : H_2O$ = 1 : 6 : 40 for 3 minutes 40 s for column isolation.
- Check the etch depth in Alpha-Step profilometer and optical microscope.
- Remove the resist by MP at 90°C for 25 minutes.

5. Oxidation

- Cleave the wafer to prepare dummies.
- Measure the diameter of AlAs layer with infra-red camera to observe the undercut.
- Keep the wafer in the beaker with methanol at 20°C to prevent the oxidation until the oxidation machine ready.
- Rinse in isopropanol which dissolves methanol residuals for 2 minutes.
- HF dip (0.1 %) for 5 s to remove the native oxides from the surface.
- Stop the etching by immersing the wafer quickly in H_2O for 15 s.
- Oxidize different dummies at 382°C for 13 minutes.
- Calculate the oxidation rate and depth.

- Oxidize at 382°C for 13 minutes 30 s.

6. N-Metalization

- Clean the wafer using acetone and isopropanol.
- Spin-coat resist AZnLOF 2070 on the wafer with 4000 rev/min for 40 s, program 4.
- Clean the edge of the wafer by edge bead remover.
- Softbake the wafer at 110°C for 2 minutes.
- Remove the resist from the back-side of the wafer by acetone.
- Expose the wafer for 8 s with 12 mW/cm^2 using the mask "N CONTACT".
- Postbake at 110°C for 90 s.
- Dip the sample in AZ826MIF for 110 to 115 s.
- Control in the microscope.
- Use O_2 plasma for 2 minutes, 10 % O_2, 0.1 Torr, 33.3 % RF (100 W).
- Dip the sample in HCl : H_2O = 1 : 1 for 30 s to remove oxides.
- Stop the reaction by immersing the wafer in H_2O for 15 s.
- Load the wafer inside the metallization chamber, evacuate for 6 hours.
- Evaporate Ge (17 nm), Au (50 nm), Ni (10 nm), Au (50 nm).
- Immerse the wafer in MP at 150°C for about one hour and use ultrasonic both for 15 minutes.
- Check the wafer under optical microscope. If lift-off works well, then clean it with acetone and isopropanol.
- Anneal the wafer up to 400°C for 90 s using the rapid thermal annealer. Then wait until the temperature reaches room temperature.

7. Polyimide Passivation 1

- Take the polyimide out of the refrigerator 2 hours before usage to avoid the moisture-picking problem.
- Clean the sample using acetone and isopropanol.
- Spin-coat with Durimide 7505 with 3000 rev/min for 40 s, program 3.
- Softbake the wafer at 100°C for 3 minutes.
- Expose the wafer for 16 s with 12 mW/cm^2 using the mask "POLYIMIDE-1".
- Immediately after exposure, postbake for 1 minute at 100°C.
- Delay 12 to 14 minutes.
- Dip the sample in HTRD2 for 90 s for development.
- Stop the development reaction by immersing the wafer in isopropanol for 1 minute.

- Heat the wafer in the annealing machine, with a heat ramp from 100 to 300°C using the program "POLY-3".

8. Polyimide Passivation 2

- Take the polyimide out of the refrigerator 2 hours before usage to avoid the moisture-picking problem.
- Clean the sample using acetone and isopropanol.
- Spin-coat Durimide 7505 with 4000 rev/min for 40 s, program 4.
- Delay 3 minutes to let the polyimide diffuse into the AlAs layer.
- Softbake the wafer at 100°C for 3 minutes.
- Expose with 12 mW/cm^2 for 16 s using the mask "POLYIMIDE-2".
- Immediately after exposure, postbake for 1 minute at 100°C.
- Delay for about 12 to 14 minutes.
- Develop with HTRD2 for 90 s.
- Stop the development reaction by immersing the wafer in isopropanol for 1 minute.
- Use O_2 plasma for 3 minutes, 10 % O_2, 0.1 Torr, 33 % RF (100 W).
- Heat the wafer in the annealing machine"OPTO ANNEALER" in a heat ramp from 100 to 300°C using the program "POLY-3".

9. Polyimide Passivation 3

- Repeat the entire processing steps mentioned in the previous section and use the same mask: "POLYIMIDE-2".

10. P-Metallization

- Clean the wafer using acetone and isopropanol.
- Spin-coat AZnLOF 2070 with 4000 rev/min for 40 s, program 4.
- Softbake the wafer at 110 °C for 2 minutes.
- Expose the wafer for 8 s with 12 mW/cm^2 using the mask "P CONT BOND".
- Postbake at 110°C for 90 s.
- Dip the wafer in AZ 826 MIF for 105 to 115 s for developing the wafer.
- Check using microscope.
- Use O_2 plasma, 2 minutes, 10 % O_2, 0.1 Torr, 33 % RF (100 W).
- Dip the sample in HCl : H_2O = 1 : 1 for 30 s to remove oxides.
- Stop the reaction by immersing the wafer in H_2O for 15 s.
- Load the wafer inside the metalization chamber, evauate for 6 hours.
- Evaporate using Ti (20 nm), Pt (50 nm), Au (150 nm).

- Immerse the wafer in MP at 150°C for about one hour and use ultrasonic both for 15 minutes.
- Check the wafer under optical microscope. If lift-off works well, then clean it with acetone and isopropanol.
- Anneal the wafer up to 400°C for 90 s using the rapid thermal annealer. Then wait until the temperature reaches room temperature.

A.3 Dry-Etched Matrix-Addressable VCSEL Arrays

1. Cleaning the Wafer

- Immerse the wafer in acetone for 5 minutes.
- Immerse the wafer in isopropanol for 5 minutes.
- Dry the wafer at 120°C for 10 minutes to get rid of residual moisture.

2. Mesa Formation

- Spin-coating the photoresist AZ1512HS using program 2 (2000 rev/min) for 40 s.
- Prebake at 100°C for 50 s.
- Expose for 8 s, 12 mW/cm^2, mask "MESA"
- Dip the wafer in AZ726MIF for 25 s, stop with water for 30 s.
- Check the wafer under optical microscope and make sure there is no residual photoresist.
- Use O_2 plasma for 2 minutes.
- Hardbake for 50 s at 120°C.
- Use reactive-ion etching for 98 minutes in order to get the mesa height of 9 μm.

3. Column Isolation

- Clean the sample.
- Spin-coat with AZnLOF 2070 photoresist using program 10, (10000 rev/min) for 40 s.
- Prebake at 110°C on the hotplate for 2 minutes.
- Expose for 7 s with 12 mW/cm^2 using mask "COL_ISO"
- Postbake at 110°C on the hotplate for 90 s.
- Dip the wafer in AZ826MIF for 5 minutes for development, then stop with water for 30 s.
- Check the sample under optical microscope and make sure there is no residual photoresist.
- Use O_2 plasma for 2 minutes.

- Use reactive-ion etching for 48 minutes to isolate columns.

4. Oxidation

- Immerse the wafer in MP at about 130°C to remove the residual photoresist.
- Clean the wafer.
- Put the wafer in methanol until the oxidation machine is ready.
- Cleave two small pieces from the wafer as dummies. Oxidize those two dummies first to estimate the oxidation rate.
- Oxidize the hot sample by the estimated oxidation rate.

5. N-Metalization

- Immerse the sample in MP at about 150°C to remove the residual photoresist. AZnLOF 2070 is very hard to remove after dry-etching. It took 3 to 4 hours. Long time in ultrasonic bath is necessary
- Clean the wafer.
- Spin-coat AZnLOF 2070 photoresist using program 4 (4000 rev/min) for 40 s.
- Prebake the sample at 110°C on the hotplate for 2 minutes.
- Expose for 23 s, 12 mW/cm^2 using the mask "N_ CONTACT".
- Postbake at 110°C on the hotplate for 90 s.
- Dip the sample in AZ826MIF for 2 minutes and 10 s, stop with water for 30 s.
- Check the wafer under optical microscope and make sure there is no residual photoresist.
- Use O_2 plasma for 2 minutes.
- Dip the wafer in HCl:H_2O=1:1 for 30 s to remove oxides.
- Stop the reaction by immersing the wafer in H_2O for 15 s.
- Load the wafer inside the metalization chamber for 6 hours to achieve an optimal vacuum condition.
- Evaporate Ge (17 nm), Au (50 nm), Ni (10 nm), Au (50 nm).
- Immerse the wafer in MP at 150°C for about one hour and use ultrasonic bath for 15 minutes.
- Check the wafer under optical microscope. If lift-off works well, then clean it with acetone and isopropanol.
- Anneal the wafer up to 400°C for 90 s using the rapid thermal annealer. Then wait until the temperature reaches room temperature.

6. Polyimide Planarization 1

- Clean the sample.

- Spin-coat Durimide 7505 photoresist using program 5, (5000 rev/min) for 40 s.
- Prebake the wafer at 100°C on the hotplate for 3 minutes.
- Expose for 16 s, 12 mW/cm^2, using the mask "POLYIMIDE_1".
- Postbake the wafer at 100°C on the hotplate for 1 minute.
- Delay 12 to 14 minutes.
- Dip the wafer in HTRD2 for 90 s, then stop with isopropanol for 1 minute.
- Heat treatment:
  1. Heat the wafer from 100 to 300°C, the heating rate is 20°C per 3 minutes.
  2. Keep the wafer at 300°C for 1 hour.
  3. Turn off the heat but leave the wafer on the hotplate for 1 hour so it will cool down.

7. Polyimide Planarization 2

- Like the previous procedure, here using the mask "POLYIMIDE_2".

8. Polyimide Planarization 3

- Like step "polyimide planarization 1", here using the mask "POLYIMIDE_3"

9. Polyimide Planarization 4

- Repeat exactly the same processing steps as for "planarization 3".

10. P-Metalization

- Clean the sample.
- Spin-coat AZnLOF 2070 photoresist using program 4 (4000 rev/min) for 40 s.
- Prebake the sample at 110°C on the hotplate for 2 minutes.
- Expose the sample for 8 s, 12 mW/cm^2 using the mask "P_ CONTACT".
- Postbake the sample at 110°C on the hotplate for 90 s.
- Dip the sample in AZ826MIF for 2 minutes and 10 s, then stop with water for 30 s.
- Check the sample under optical microscope and make sure there is no residual photoresist.
- Use O_2 plasma for 2 minutes.
- Dip the wafer in HCl:H_2O=1:1 for 30 s to remove oxides.
- Stop the reaction by immersing the sample in H_2O for 15 s.
- Load the sample inside the metalization chamber for 6 hours to achieve an optimal vacuum condition.
- Evaporate Ti (20 nm), Pt (50 nm), Au (150 nm).
- Immerse the sample in MP at 150°C for about one hour and use ultrasonic both for 15 minutes.

- Check the sample under optical microscope. If lift-off works well, then clean it with acetone and isopropanol.

11. Metalization for Wire Bonding

- Heat treatment needs to be done before photolithography:
  1. Adjust the temperature of the hotplate to 400°C and then start the heating.
  2. Keep the wafer at 400°C for one hour.
  3. Switch off the hotplate and leave the wafer on the hotplate for one and a half hours.
- Clean the wafer.
- Spin-coat with AZnLOF 2070 photoresist using program 4 (4000rev/min) for 40 s.
- Prebake at 110°C on the hotplate for 2 minutes.
- Expose the wafer for 8 s, 12mW/cm^2 using the mask "EP_3".
- Postbake at 110°C on the hotplate for 90 s.
- Dip the sample in AZ826MIF for 2 minutes and 10 s, then stop with water for 30 s.
- Check the sample under optical microscope and make sure there is no residual photoresist.
- Use O_2 plasma for 2 minutes.
- Evaporate Ni (300 nm), Au (100 nm), Ni (300 nm), Au (100 nm).
- Immerse the sample in MP at 150°C for about one hour and use ultrasonic bath for 15 minutes.
- Check the sample under optical microscope. If lift-off works well, then clean it with acetone and isopropanol.

Appendix B

Epitaxial Structures

In this appendix, some of the processed VCSEL layer structures are listed in tables. The common feature of these structures is top-side emission in the vicinity of 850 nm wavelength. A standard VCSEL layer structure is shown in Table B.1. Let us refer to this structure as M04-050. It is used for the simulation of the total reflectivity spectrum. Table B.2 provides the VCSEL layer structure with an antiphase layer on the top of the p-DBR mirror, a wafer which was utilized for shallow surface relief etching. Let us refer to this structure as M04-064. The two structures named M06-016 and M06-035, which were processed into matrix-addressable VCSEL arrays, are listed in Tables B.3 and B.4. For the shallow surface relief, a common n-contact on the back side has been utilized. For this purpose, the substrate in Table B.2 is n-doped. On the other hand, for matrix-addressable VCSEL arrays it is necessary to separate the n-columns, which requires an undoped substrate, as written in Tables B.3 and B.4. The main difference between structure M06-016 and M06-035 are the thickness and doping of the buffer layer. Both the thickness and the n-doping level are higher in structure M06-035. The wafers according to the tables have been grown by F. Rinaldi and D. Wahl in the Institute of Optoelectronics. The wafer material for devices 1 and 2 in Sect. 6.2.1 has been provided by Philips Technologie GmbH U-L-M Photonics, Ulm, Germany.

Table B.1: Standard VCSEL structure (M04-050).

No. of pairs	Layer thickness (nm)	Material	Al composition	Doping concentration (cm^{-3})
substrate	500000	GaAs		n-doped
1×				
	500	GaAs		undoped
	49.1	AlGaAs	0.2	1.3e18 to 2.4e18
38×				
	12.4	AlGaAs	0.27 to 0.47	2.2e18 to 2.6e18
	19.2	AlGaAs	0.47 to 0.9	2.6e18 to 2.9e18
n-DBR	29.7	AlGaAs	0.9	2.9e18 to 1.6e18
	19.2	AlGaAs	0.9 to 0.47	1.6e18 to 1.4e18
	12.4	AlGaAs	0.47 to 0.27	1.4e18 to 1.2e18
	36.8	AlGaAs	0.2	1.3e18 to 2.4e18
1×				
	12.4	AlGaAs	0.27 to 0.47	2.2e18 to 2.6e18
	19.2	AlGaAs	0.47 to 0.9	2.6e18 to 2.9e18
	29.7	AlGaAs	0.9	2.9e18
	19.2	AlGaAs	0.9 to 0.47	2.9e18 to 1.3e18
	12.5	AlGaAs	0.47	1.3e18 to 3.0e17
	44.3	AlGaAs	0.47	3.0e17 to 1.1e17
n-cladding	36.5	AlGaAs	0.47 to 0.27	
	9.9	AlGaAs	0.27	
2×				
	7.9	GaAs		
	9.9	AlGaAs	0.27	
1×				
	7.9	GaAs		
	9.9	AlGaAs	0.27	
p-cladding	37.1	AlGaAs	0.27 to 0.47	
	25.8	AlGaAs	0.47	6.6e16 to 1.2e18
	61.5	AlGaAs	0.47	1.2e18 to 1.7e18
	19.2	AlGaAs	0.47 to 0.9	1.7e18 to 1.1e19
oxide layer	32	AlAs	1	1.2e19
	19.2	AlGaAs	0.47 to 0.9	1.1e19 to 1.7e18
	31	AlGaAs	0.47	1.7e18
	19.2	AlGaAs	0.47 to 0.9	1.7e18 to 2.0e18
	29.7	AlGaAs	0.9	2.0e18 to 3.0e18
	19.2	AlGaAs	0.9 to 0.47	3.0e18 to 2.6e18
	12.4	AlGaAs	0.47 to 0.27	1.7e18 to 1.5e18
23×				
	36.8	AlGaAs	0.2	1.7e18
	12.4	AlGaAs	0.27 to 0.47	1.5e18 to 1.7e18
p-DBR	19.2	AlGaAs	0.47 to 0.9	1.7e18 to 2.2e18
	29.7	AlGaAs	0.9	2.2e18 to 3.0e18
	19.2	AlGaAs	0.9 to 0.47	3.0e18 to 4.0e18
	12.4	AlGaAs	0.47 to 0.27	4.0e18 to 1.5e18
1×				
	9.7	AlGaAs	0.2	1.7e18 to 3.9e18
p^+- layer	8.4	GaAs		4.9e18
	29	GaAs		8.1e19 to 1.6e20

Table B.2: VCSEL structure for inverted relief formation (M04-064).

No. of pairs	Layer thickness (nm)	Material	Al composition	Doping concentration (cm^{-3})
substrate	500000	GaAs		n-doped
1×				
	500	GaAs		undoped
	49.1	AlGaAs	0.2	1.3e18 to 2.4e18
38×				
	12.4	AlGaAs	0.27 to 0.47	2.2e18 to 2.6e18
	19.2	AlGaAs	0.47 to 0.9	2.6e18 to 2.9e18
n-DBR	29.7	AlGaAs	0.9	2.9e18 to 1.6e18
	19.2	AlGaAs	0.9 to 0.47	1.6e18 to 1.4e18
	12.4	AlGaAs	0.47 to 0.27	1.4e18 to 1.2e18
	36.8	AlGaAs	0.2	1.3e18 to 2.4e18
1×				
	12.4	AlGaAs	0.27 to 0.47	2.2e18 to 2.6e18
	19.2	AlGaAs	0.47 to 0.9	2.6e18 to 2.9e18
	29.7	AlGaAs	0.9	2.9e18
	19.2	AlGaAs	0.9 to 0.47	2.9e18 to 1.3e18
	12.5	AlGaAs	0.47	1.3e18 to 3.0e17
	44.3	AlGaAs	0.47	3.0e17 to 1.1e17
n-cladding	36.5	AlGaAs	0.47 to 0.27	
	9.9	AlGaAs	0.27	
2×				
	7.9	GaAs		
	9.9	AlGaAs	0.27	
1×				
	7.9	GaAs		
	9.9	AlGaAs	0.27	
p-cladding	37.1	AlGaAs	0.27 to 0.47	
	25.8	AlGaAs	0.47	6.6e16 to 1.2e18
	61.5	AlGaAs	0.47	1.2e18 to 1.7e18
	19.2	AlGaAs	0.47 to 0.9	1.7e18 to 1.1e19
oxide layer	32	AlAs	1	1.2e19
	19.2	AlGaAs	0.47 to 0.9	1.1e19 to 1.7e18
	31	AlGaAs	0.47	1.7e18
	19.2	AlGaAs	0.47 to 0.9	1.7e18 to 2.0e18
	29.7	AlGaAs	0.9	2.0e18 to 3.0e18
	19.2	AlGaAs	0.9 to 0.47	3.0e18 to 2.6e18
	12.4	AlGaAs	0.47 to 0.27	1.7e18 to 1.5e18
23×				
	36.8	AlGaAs	0.2	1.7e18
	12.4	AlGaAs	0.27 to 0.47	1.5e18 to 1.7e18
p-DBR	19.2	AlGaAs	0.47 to 0.9	1.7e18 to 2.2e18
	29.7	AlGaAs	0.9	2.2e18 to 3.0e18
	19.2	AlGaAs	0.9 to 0.47	3.0e18 to 4.0e18
	12.4	AlGaAs	0.47 to 0.27	4.0e18 to 1.5e18
1×				
	9.7	AlGaAs	0.2	1.7e18 to 3.9e18
p^+- layer	56.7	GaAs		4.9e18
	29	GaAs		8.1e19 to 1.6e20

Table B.3: Layer structure for matrix-addressable VCSEL arrays (M06-016).

No. of pairs	Layer thickness (nm)	Material	Al composition	Doping concentration (cm^{-3})
substrate	500000	GaAs		undoped
	99.9	GaAs		undoped
1×				
	200	GaAs		1.7e18 to 6e18
buffer	2299.9	GaAs		6e18
	200	GaAs		6e18 to 1.7e18
	49.1	AlGaAs	0.2	1.3e18 to 2.4e18
38×				
	12.4	AlGaAs	0.27 to 0.47	2.2e18 to 2.6e18
	19.2	AlGaAs	0.47 to 0.9	2.6e18 to 2.9e18
n-DBR	29.7	AlGaAs	0.9	2.9e18 to 1.6e18
	19.2	AlGaAs	0.9 to 0.47	1.6e18 to 1.4e18
	12.4	AlGaAs	0.47 to 0.27	1.4e18 to 1.2e18
	36.8	AlGaAs	0.2	1.3e18 to 2.4e18
1×				
	12.4	AlGaAs	0.27 to 0.47	2.2e18 to 2.6e18
	19.2	AlGaAs	0.47 to 0.9	2.6e18 to 2.9e18
	29.7	AlGaAs	0.9	2.9e18
	19.2	AlGaAs	0.9 to 0.47	2.9e18 to 1.3e18
	12.5	AlGaAs	0.47	1.3e18 to 3.0e17
	44.3	AlGaAs	0.47	3.0e17 to 1.1e17
n-cladding	36.5	AlGaAs	0.47 to 0.27	
	9.9	AlGaAs	0.27	
2×				
	7.9	GaAs		
	9.9	AlGaAs	0.27	
1×				
	7.9	GaAs		
	9.9	AlGaAs	0.27	
p-cladding	37.1	AlGaAs	0.27 to 0.47	
	25.8	AlGaAs	0.47	6.6e16 to 1.2e18
	61.5	AlGaAs	0.47	1.2e18 to 1.7e18
	19.2	AlGaAs	0.47 to 0.9	1.7e18 to 1.1e19
oxide layer	32	AlAs	1	1.2e19
	19.2	AlGaAs	0.47 to 0.9	1.1e19 to 1.7e18
	31	AlGaAs	0.47	1.7e18
	19.2	AlGaAs	0.47 to 0.9	1.7e18 to 2.0e18
	29.7	AlGaAs	0.9	2.0e18 to 3.0e18
	19.2	AlGaAs	0.9 to 0.47	3.0e18 to 2.6e18
	12.4	AlGaAs	0.47 to 0.27	1.7e18 to 1.5e18
23×				
	36.8	AlGaAs	0.2	1.7e18
	12.4	AlGaAs	0.27 to 0.47	1.5e18 to 1.7e18
p-DBR	19.2	AlGaAs	0.47 to 0.9	1.7e18 to 2.2e18
	29.7	AlGaAs	0.9	2.2e18 to 3.0e18
	19.2	AlGaAs	0.9 to 0.47	3.0e18 to 4.0e18
	12.4	AlGaAs	0.47 to 0.27	4.0e18 to 1.5e18
1×				
	9.7	AlGaAs	0.2	1.7e18 to 3.9e18
p^+- layer	8.4	GaAs		4.9e18
	29	GaAs		8.1e19 to 1.6e20

Table B.4: Modified layer structure for matrix-addressable VCSEL arrays (M06-035).

No. of pairs	Layer thickness (nm)	Material	Al composition	Doping concentration (cm^{-3})
substrate	500000	GaAs		undoped
	99.9	GaAs		undoped
1×				
	200	GaAs		1.7e18 to 6e18
buffer	2299.9	GaAs		6e18
	200	GaAs		6e18 to 1.7e18
	49.1	AlGaAs	0.2	1.3e18 to 2.4e18
38×				
	12.4	AlGaAs	0.27 to 0.47	2.2e18 to 2.6e18
	19.2	AlGaAs	0.47 to 0.9	2.6e18 to 2.9e18
n-DBR	29.7	AlGaAs	0.9	2.9e18 to 1.6e18
	19.2	AlGaAs	0.9 to 0.47	1.6e18 to 1.4e18
	12.4	AlGaAs	0.47 to 0.27	1.4e18 to 1.2e18
	36.8	AlGaAs	0.2	1.3e18 to 2.4e18
1×				
	12.4	AlGaAs	0.27 to 0.47	2.2e18 to 2.6e18
	19.2	AlGaAs	0.47 to 0.9	2.6e18 to 2.9e18
	29.7	AlGaAs	0.9	2.9e18
	19.2	AlGaAs	0.9 to 0.47	2.9e18 to 1.3e18
	12.5	AlGaAs	0.47	1.3e18 to 3.0e17
	44.3	AlGaAs	0.47	3.0e17 to 1.1e17
n-cladding	36.5	AlGaAs	0.47 to 0.27	
	9.9	AlGaAs	0.27	
2×				
	7.9	GaAs		
	9.9	AlGaAs	0.27	
1×				
	7.9	GaAs		
	9.9	AlGaAs	0.27	
p-cladding	37.1	AlGaAs	0.27 to 0.47	
	25.8	AlGaAs	0.47	6.6e16 to 1.2e18
	61.5	AlGaAs	0.47	1.2e18 to 1.7e18
	19.2	AlGaAs	0.47 to 0.9	1.7e18 to 1.1e19
oxide layer	32	AlAs	1	1.2e19
	19.2	AlGaAs	0.47 to 0.9	1.1e19 to 1.7e18
	31	AlGaAs	0.47	1.7e18
	19.2	AlGaAs	0.47 to 0.9	1.7e18 to 2.0e18
	29.7	AlGaAs	0.9	2.0e18 to 3.0e18
	19.2	AlGaAs	0.9 to 0.47	3.0e18 to 2.6e18
	12.4	AlGaAs	0.47 to 0.27	1.7e18 to 1.5e18
23×				
	36.8	AlGaAs	0.2	1.7e18
	12.4	AlGaAs	0.27 to 0.47	1.5e18 to 1.7e18
p-DBR	19.2	AlGaAs	0.47 to 0.9	1.7e18 to 2.2e18
	29.7	AlGaAs	0.9	2.2e18 to 3.0e18
	19.2	AlGaAs	0.9 to 0.47	3.0e18 to 4.0e18
	12.4	AlGaAs	0.47 to 0.27	4.0e18 to 1.5e18
1×				
	9.7	AlGaAs	0.2	1.7e18 to 3.9e18
p^+- layer	8.4	GaAs		4.9e18
	29	GaAs		8.1e19 to 1.6e20

Appendix C

List of Symbols and Acronyms

a	aperture length
a_{eff}	effective aperture radius
B	phase parameter
B_{eff}	effective recombination coefficient
C_u	correction factor for the mode with order u
d	aperture width
F	Fresnel number
g_{th}	laser threshold gain
Δg_{th}	threshold gain difference
$g_{eff,i}$	effective gain of the i-th mode
g	material gain
g_{in}	threshold gain inside the aperture opening
g_{out}	threshold gain outside the aperture opening
h	Planck's constant
I_{th}	laser threshold current
I	pumping current
j_{th}	threshold current density
k	wavenumber
L	inner cavity length
L_{w}	thickness of each quantum well
L_{eff}	effective cavity length
$l_{\text{eff,t}}$	effective top mirror length
$l_{\text{eff,b}}$	effective bottom mirror length
n_{B}	average refractive index of the Bragg mirror
$n_{\text{B,l}}$	low index material of Bragg mirror
$n_{\text{B,h}}$	high index material of Bragg mirror
n_{cav}	average refractive index in the cavity
n_1	refractive index of the core

n_2	refractive index of the cladding
N_w	number of quantum wells
P_out	emitted output power
P_A	power in the active aperture
P_i	power of the i-th mode
P_p	power in the area of the etch pattern
P_t	total power of the mode
P_IV	electric power
q	electron charge
R_a	radius of phase front curvature along the aperture length
R_d	radius of phase front curvature along the aperture width
R_s	differential resistance or differential resistance
$r_\mathrm{m,t,b}$	maximum amplitude reflectivity of the top or bottom mirror
R_t	power reflectivity of the top DBR
R_b	power reflectivity of the bottom DBR
u	normalized radial propagation constant for the waveguide core
V	frequency parameter
v	normalized radial propagation constant for the waveguide cladding
z_0	Rayleigh range
α_i	internal modal power loss
α_m	output mirror loss
α_a	free-carrier loss within the active segments
α_p	free-carrier loss within the passive segments
α_sc	scattering loss throughout the cavity, scattering loss for a single pass
β	axial propagation constant
Γ	three-dimensional mode confinement factor
Γ_{xy}	lateral confinement factor
Γ_z	axial confinement factor
$\Gamma_{xy,A,i}$	lateral confinement factor of the aperture for the mode i
Γ_s	confinement factor of the selected mode
Γ_c	confinement factor of the competitive mode
$\Gamma_{xy,p}$	lateral confinement factor in the presence of the surface pattern
$\Delta\lambda_\mathrm{ox}$	cavity resonance shift
Δn	difference in refractive indices between core and cladding
Δn_B	contrast in refractive indices of a Bragg mirror pair
ΔT	temperature difference

ϵ_0	permittivity in free space
ξ	axial enhancement factor
η_d	differential quantum efficiency
λ	vacuum wavelength
ν	laser frequency
σ_T	thermal conductivity
ϕ_0	characteristic phase shift
ψ	electric or magnetic field amplitude
ω_a	spot size along the aperture length
ω_d	spot size along the aperture width

Al	aluminum
AlGaAs	aluminum gallium arsenide
CAIBE	chemically assisted ion beam etching
CCD	charge coupled device
CW	continuous wave
DBR	distributed Bragg reflector
EEL	edge-emitting laser
FWHM	full width at half maximum
GaAs	gallium arsenide
IR	infra-red
InGaAs	indium gallium arsenide
LI	light–current
LIV	light–current–voltage
LP	linearly polarized
MBE	molecular beam epitaxy
MOVPE	metal-organic vapor phase epitaxy
NA	numerical aperture
OPSR	orthogonal polarization suppression ratio
PR	polarization-resolved
PDE	partial differential equation
RIE	reactive-ion beam etching
QW	quantum well
SMSR	side-mode suppression ratio
TE	transverse electric
TM	transverse magnetic
UV	ultra-violet
VCSEL	vertical-cavity surface-emitting laser
IV	current–voltage

Appendix D

Publications

- A. Gadallah, M. Stach, F. Rinaldi, S. Lorch, I. Kardosh, P. Gerlach, and R. Michalzik, "Fabrication and characterization of GaAs-based transceiver chips for bidirectional optical data transmission", in Proc. XXVI Conf. on Solid State Physics and Materials Science of the Egyptian Materials Research Society, Eg-MRS 2006 & Workshop on Nanostructures: Science, Fabrication, Characterization and Devices, p. 128. Alexandria, Egypt, Sept. 2006.
- A. Kroner, A. Gadallah, I. Kardosh, F. Rinaldi, and R. Michalzik, "Integrated VCSEL trap arrays for microfluidic particle separation and sorting", in Proc. EOS Topical Meeting on Biophotonics and Biomedical Optics, pp. 140–141. Paris, France, Oct. 2006.
- M. Stach, F. Rinaldi, A. Gadallah, S. Lorch, I. Kardosh, P. Gerlach, and R. Michalzik, "1 Gbit/s bidirectional data transmission over 100 m graded-index glass optical fiber with monolithically integrated transceiver chips", in Proc. 32nd Europ. Conf. on Opt. Commun., ECOC 2006, vol. 3, pp. 493–494. Cannes, France, Sept. 2006.
- A. Gadallah, A. Kroner, I. Kardosh, F. Rinaldi, and R. Michalzik, "Oblong-shaped VCSELs with pre-defined mode patterns", in Semiconductor Lasers and Laser Dynamics III, K.P. Panayotov, M. Sciamanna, A.A. Valle, R. Michalzik (Eds.), Proc. SPIE, 6997, pp. 69971R-1–9, 2008.

Bibliography

[1] H.J. Unold, S.W.Z. Mahmoud, R. Jäger, M. Grabherr, R. Michalzik, and K.J. Ebeling, "Large area single-mode VCSELs and self-aligned surface relief", *IEEE J. Select. Topics Quantum Electron.*, vol. 7, no. 2, pp. 386–392, 2001.

[2] L.A. Coldren and E.R. Hegblom, "Fundamental issues in VCSEL design", Chap. 2 in *Vertical-cavity surface-emitting lasers design, fabrication, characterization, and applications*, C. Wilmsen, H. Temkin, and L.A. Coldren (Eds.), pp. 32–65. Cambridge: Cambridge University Press, 1999.

[3] H. Li and K. Iga (Eds.), *Vertical-Cavity Surface-Emitting Laser Devices*, Berlin: Springer-Verlag, 2003.

[4] R. Michalzik and K.J. Ebeling, "Generalized BV diagrams for higher order transverse modes in planar vertical-cavity laser diodes", *IEEE J. Quantum Electron.*, vol. 31, no. 8, pp. 1371–1379, 1995.

[5] G.M. Yang, M.H. MacDougal, and P.D. Dapkus, "Ultralow threshold current vertical-cavity surface-emitting lasers obtained with selective oxidation", *Electron. Lett.*, vol. 31, no. 11, pp. 886–888, 1995.

[6] K.D. Choquette, R.P. Schneider, Jr., K.L. Lear, and K.M. Geib, "Low threshold voltage vertical-cavity lasers fabricated by selective oxidation", *Electron. Lett.*, vol. 30, no. 24, pp. 2043–2044, 1994.

[7] B. Tell, K.F. Brown-Goebeler, R.E. Leibenguth, F.M. Baez, and Y.H. Lee, "Temperature dependence of GaAs-AlGaAs vertical cavity surface emitting lasers", *Appl. Phys. Lett.*, vol. 60, no. 6, pp. 683–685, 1992.

[8] K.D. Choquette, R.P. Schneider, M.H. Crawford, K.M. Geib, and J.J. Figiel, "Continuous wave operation of 640–660 nm selectively oxidized AlGaInP vertical-cavity lasers", *Electron. Lett.*, vol. 31, no. 14, pp. 1145–1146, 1995.

[9] D.I. Babic, K. Streubel, R.P Mirin, N.M. Margalit, E.L. Hu, J.E. Bowers, D.E. Mars, L. Yang, and K. Carey, "Room-temperature continuous-wave operation of 1.54 μm vertical-cavity lasers", *IEEE Photon. Technol. Lett.*, vol. 7, no. 11, pp. 1225–1227, 1995.

[10] K.D. Choquette, K.L Lear, R.P Schneider, Jr., K.M. Geib, J.J. Figiel, and R. Hull, "Fabrication and performance of selectively-oxidized vertical-cavity lasers", *IEEE Photon. Technol. Lett.*, vol. 7, no. 1, pp. 1237–1239, 1995.

[11] J.W. Scott, B.J. Thibeault, D.B. Young, L.A. Coldren, and F.H. Peters, "High efiicienc sub-milliamp vertical cavity lasers with intra-cavity contacts", *IEEE Photon. Technol. Lett.*, vol. 6, no. 6, pp. 678–680, 1994.

[12] D.B. Young, A. Kapila, J.W. Scott, V. Malhotra, and L.A. Coldren, "Reduced threshold vertical-cavity surface-emitting lasers", *Electron. Lett.*, vol. 30, no. 3, pp. 233–234, 1994.

[13] R.H. Yan, Z.M. Chuang, S.W. Corzine, and L.A. Coldren, "Simultaneous gain and phase-shift enhancement in periodic gain structures", *J. Appl. Phys.*, vol. 67, no. 9, pp. 4387–4389, 1990.

[14] S.W. Crozine, R.S. Geels, J.W. Scott, R-H. Yan, and L.A. Coldren, "Design of Fabry-Perot surface-emitting lasers with a periodic gain structure", *IEEE J. Quantum Electron.*, vol. 25, no. 6, pp. 1513–1524, 1989.

[15] R. Michalzik and K.J. Ebeling, "Operating principles of VCSELs", Chap. 3 in *Vertical-Cavity Surface-Emitting Laser Devices*, H. Li and K. Iga (Eds.), pp. 53–98. Berlin: Springer-Verlag, 2003.

[16] D.I. Babic and S.W. Corzine, "Analytical expressions for the reflection delay, penetration depth and absorpance of quarter-wave dielectric mirrors", *IEEE J. Quantum Electron.*, vol. 28, no. 2, pp. 514–524, 1992.

[17] A. Yariv, *Quantum Electronics*. 3rd ed. New York: Wiley, 1989.

[18] J.W. Scott, R.S. Geels, S.W. Corzine, and L.A. Coldren, "Modeling temperature effects and spatial hole burning to optimize vertical-cavity surface-emitting laser performance", *IEEE J. Quantum Electron.*, vol. 29, no. 5, pp. 1295–1308, 1993.

[19] S.S. Kutateladze and V.M. Borishansskii, "A concise encyclopedia of heat transfer", Oxford: Pergamon, 1966.

[20] R. Szweda, "VCSEL applications diversify as technology matures", *III-Vs Review*, vol. 19, no. 1, pp. 34–38, 2006.

[21] M. Stach, F. Rinaldi, M. Chandran, S. Lorch, and R. Michalzik, "Monolithically integrated GaAs-based transceiver chips for bidirectional optical data transmission", *Electron. Lett.*, vol. 42, no. 12, pp. 716–718, 2006.

[22] G. Steinle, F. Mederer, M. Kicherer, and R. Michalzik, G. Kristen, A.Y. Egorov, H. Riechert, H.D. Wolf, and K.J. Ebeling, "Data transmission up to 10 Gbit/s with 1.3 μm wavelength InGaAsN VCSELs", *Electron. Lett.*, vol. 37, no. 10, pp. 632–634, 2001.

[23] R. Michalzik, A. Kroner, A. Bergmann, and F. Rinaldi, "VCSEL-based optical trapping for microparticle manipulation", in *Vertical-Cavity Surface-Emitting Lasers XIII*, K.D. Choquette, C. Lei (Eds.), Proc. SPIE 7229, pp. 722908-1–13, 2009.

[24] A. Kroner, I. Kardosh, F. Rinaldi, and R. Michalzik, "Towards VCSEL-based integrated optical traps for biomedical applications", *Electron. Lett.*, vol. 42, no. 2, pp. 93–94, 2006.

[25] A. Kroner, F. Rinaldi, R. Rösch, and R. Michalzik, "Optical particle manipulation by application-specific densely packed VCSEL arrays", *Electron. Lett.*, vol. 44, no. 5, pp. 353–354, 2008.

[26] M. Naruse and M. Ishikawa, "Parallel confocal laser microscope system using smart pixel arrays", in *Novel Optical Systems Design and Optimization III*, J.M. Sasian (Ed.), Proc. SPIE 4092, pp. 94–101, 2000.

[27] M. Grabherr, R. King, R. Jäger, D. Wiedenmann, P. Gerlach, D. Duckeck, and C. Wimmer, "Volume production of polarization controlled single mode VCSELs", in *Vertical-Cavity Surface-Emitting Lasers XII*, C. Lei, J.K. Guenter (Eds.), Proc. SPIE. 6908, pp. 690803-1–9, 2008.

[28] E.G. Paek, J.R. Wullert, A. Von Lehmen, A. Scherer, J. Harbison, L.T. Florez, H.J. Yoo, R. Martin, J.L. Jewell, and Y. Lee, "Compact and ultrafast holographic memory using a surface emitting microlaser array", *Opt. Lett.*, vol. 15, no. 6, pp. 341–343, 1990.

[29] J.M. Ostermann, F. Rinaldi, P. Debernardi, and R. Michalzik, "VCSELs with enhanced single-mode power and stablized polarization for oxygen sensing", *IEEE Photon. Technol. Lett.*, vol. 17, no. 11, pp. 2256–2258, 2005.

[30] D.K. Serkland, K.M. Geib, G.M. Peake, R. Lutwak, A. Rashed, M. Varghese, G. Tepolt and M. Prouty, "VCSELs for atomic sensors", in *Vertical-Cavity Surface-Emitting Lasers XI, K.D. Choquette, J.K. Guenter (Eds.)*, Proc. SPIE 6484, pp. 648406-1–10, 2007.

[31] M.K. Haldar, "Introducing the finite element method in electromagnetics to undergraduates using MATLAB", International J. Electrical Engineering Education, vol. 43, no. 3, pp. 232–244, 2006.

[32] R. Michalzik, W. Schmid, S.W.Z. Mahmoud, and R. Jäger, Ulm University, Institute of Optoelectronics.

[33] E.A.J. Marcatili, "Dielectric rectangular waveguide and directional coupler for integrated optics", *Bell Syst. Tech. J.*, vol. 148, no. 9 pp. 2071–2102, 1969.

[34] A. Valle, J. Sarma, and K.A. Shore, "Spatial holeburning effect on the dynamics of vertical-cavity surface-emitting laser diodes", *IEEE J. Quantum Electron.*, vol. 31, no. 8, pp. 1423–1431, 1995.

[35] S.A. Schecanoff, *Electromagnetic Waves*, New York: D. Van Nostrand, 1943.

[36] M. Brunner, K. Gulden, R. Hövel, M. Moser, and M. Ilegems, "Thermal lensing effects in small oxide confined vertical-cavity surface-emitting lasers", *Appl. Phys. Lett.*, vol. 76, no. 1, pp. 7–9, 2000.

[37] N.K. Dutta, L.W. Tu, G. Hasnain, G. Zydzik, Y.H Wang, and A.Y. Cho, "Anomalous temporal resonance of gain guided surface emitting lasers", *Electron. Lett.*, vol. 27, no. 3, pp. 208–210, 1990.

[38] P.W.A. Mc Ilroy, A. Kurobe, and Y. Uematsu, "Analysis and application of theoretical gain curves to the design of multi-quantum well lasers", *IEEE J. Quantum Electron.*, vol. QE-21, no. 12, pp. 1958–1963, 1985.

[39] M. Asada, A. Kameyama, and Y. Suematsu, "Gain and intervalence band absorption in quantum-well lasers", *IEEE J. Quantum Electron.*, vol. QE-20, no. 7, pp. 745–753, 1984.

[40] K. Stubkjaer, M. Asada, S. Arai, and Y. Suematsu, "Spontaneous recombination, gain and refractive index variation for 1.6 µm wavelength InGaAsP/InP lasers", *Jap. J. Appl. Phys.*, vol. 20, no. 8, pp. 1499–1505, 1981.

[41] H. Namizaki, H. Kan, M. Ishii, and A. Ito, "Current dependence of spontaneous carrier lifetimes in GaAs-GaAlAs double hetrostructure lasers", *Appl. Phys. Lett.*, vol. 24, no. 10, pp. 486–487, 1974.

[42] R. Michalzik, *Modellierung und Design von Laserdioden mit Vertikalresonator*, Ph.D. Thesis, Fakultät für Ingenieurwissenschaften der Universität Ulm, 1996. Erschienen in: Fortschritt-Berischte, VDI-Reihe 9, Nr. 257. Düsseldorf: VDI Verlag, 1997.

[43] H. Kogelnik and T. Li, "Laser beams and resonators", *Appl. Opt.*, vol. 5, no. 10, pp. 1550–1567, 1966.

[44] W. Nakwaski and R.B. Sarzała, "Transverse modes in gain-guided vertical-cavity surface-emitting lasers", *Opt. Comm.*, vol. 148, no. 1–3, pp. 63–69, 1998.

[45] K.J. Ebeling, *Integrated Optoelectronics*. Berlin: Springer-Verlag, 1993.

[46] D. Marcuse, *Light Transmission Optics*. New York: Van Nostrand, Reinholt, 1972.

[47] W.T. Silvfast, *Laser Fundamentals*. New York: Cambridge University Press, 1996.

[48] C.J. Chang-Hasnain, M. Orenstein, A. Von Lehmen, L.T. Florez, J.P. Harbison, and N.G. Stoffel, "Transverse mode characteristics of vertical-cavity surface emitting lasers", *Appl. Phys. Lett.*, vol. 57, no. 3, pp. 218–220, 1990.

[49] C. Degen, I. Fischer, and W. Elsäßer, "Transverse modes in oxide confined VCSELs: influence of pump profile, spatial hole burning, and thermal effects", *Optics Express*, vol. 5, no. 3, pp. 38–47, 1999.

[50] H. Li, T.L. Lucas, J.G. McInerney, and R.A. Morgan, "Transverse modes and patterns of electrically pumped vertical-cavity surface-emitting semiconductor lasers", *Chaos, Solitons & Fractals*, vol. 4, no. 8–9, pp. 1619–1635, 1994.

[51] J.E. Epler, S. Gehrsitz, K.H. Gulden, M. Moser, H.C. Sigg, and H.W. Lehmann, "Mode behavior and high resolution spectra of circularly-symmetric GaAs-AlGaAs air-post vertical cavity surface emitting lasers", *Appl. Phys. Lett.*, vol. 69, no. 6, pp. 722–724, 1996.

[52] D.R. Tompkins, Jr. and P.F. Rodney, "Six-parameter Gaussian modes in free space", *Phys. Rev. A*, vol. 12, no. 2, pp. 599–610, 1975.

[53] J.T. Luxon and D.E. Parker "Practical spot size definetion for single higher-order rectangular-mode laser beams", *Appl. Opt.*, vol. 20, no. 10, pp. 1728–1729, 1981.

[54] W.H. Carter, "Spot size and divergence for Hermite Gaussian beams of any order", *Appl. Opt.*, vol. 19, no. 7, pp. 1027–1029, 1980.

[55] J.T. Luxon, D.E. Parker, and J. Karkheck, "Waist location and Rayleigh range for high-order mode laser beams", *Appl. Opt.*, vol. 23, no. 13, pp. 2088-2090, 1984.

[56] J.T. Luxon,"Propagation of laser light", Chap. 2 in *Laser Materials Processing*, L. Migliori (Ed.), pp. 31–48. New Yourk: Marcel Decker, Inc, 1996.

[57] R.J. Pressley, *CRC Laser Handbook.* Cleveland: CRC Press, 1971.

[58] R.P. Sarzała, W. Nakwaski, and M. Osiński, "Effects of carrier diffusion on thermal properties of proton-implanted top-surface emitting lasers", in *Physics and Simulation of Optoelectronic Devices III*, M. Osiński, W.W. Chow (Eds.), Proc. SPIE 2399, pp. 583–604, 1995.

[59] P. Debernardi, A. Kroner, F. Rinaldi, and R. Michalzik, "Surface relief vs. standard VCSELs: a comparison between experimental and hot-cavity model results", *IEEE J. Select. Topics Quantum Electron.*, vol. 15, no. 3, pp. 828–837, 2009.

[60] H. C. Casey, Jr. and M.B. Panish, *Hetrostructure Lasers*, Part A: *Fundamental Principles*, Orlando, Florida: Academic Press, 1978.

[61] D. Wiedenmann, M. Grabherr, R. Jäger, and R. King, "High volume production of single-mode VCSELs", in *Vertical-Cavity Surface-Emitting Lasers X*, C. Lei, K.D. Choquette (Eds.), Proc. SPIE 6132, pp. 1–12, 2006.

[62] A. Kroner, F. Rinaldi, R. Rösch, and R. Michalzik, "Optical particle manipulation by application-specific densely packed VCSEL arrays", *Electron. Lett.*, vol. 44, no. 5, pp. 353–354, 2008.

[63] P.R. Claisse, W. Jiang, P.A. Kiely, B. Gable, and B. Koonse, "Single high order mode VCSEL", *Electron. Lett.*, vol. 34, no. 7, pp. 681–682, 1998.

[64] M.C. Hutley, *Diffraction Gratings.* 2nd. ed. London: Academic Press, , 1990.

[65] G. Reiner, *Molekularstrahlepitaxie für hocheffiziente Laserdioden mit Vertikalresonator*, Ph.D. Thesis, Fakultät für Ingenieurwissenschaften der Universität Ulm, 1999. Published in Fortschritt-Berichte, VDI-Reihe 9, Nr. 296. Düsseldorf: VDI Verlag, 1999.

[66] R. Jäger, *Molekularstrahlepitaxie hocheffiziente Leucht- und Laserdioden* , Ph.D. Thesis, Fakultät für Ingenieurwissenschaften der Universität Ulm, 2002. Göttingen: Cuvilliar Verlag, 2003.

[67] F. Rinaldi, *MBE Growth and Characterization of Multilayer Structures for Vertically Emitting Laser Devices*, Ph.D. Thesis, Fakultät für Ingenieurwissenschaften und Informatik der Unversität Ulm, 2008.

[68] A.M. Sharizal, P.O. Leisher, K.D. Choquette, P.K. Choudhury, S.M. Mitani, Y.M. Razman and A.M. Abdul Fatah, "Effect of oxide aperture on the performance of 850 nm vertical-cavity surface-emitting lasers ", *Optik-International Journal for Light and Electron Optics*, vol. 120, no. 3, pp. 121–126, 2009.

[69] A.R. Hegblom, D.I. Babic, B.J. Thibeault, and L.A. Coldren, "Scattering losses from dielectric apertures in vertical-cavity laser", *IEEE J. Select. Topics Quantum Electron.*, vol. 3, no. 2, pp. 379–389, 1997.

[70] B.E.A. Saleh and M.C. Teich, *Fundamentals of Photonics*. New York: Wiley, 1991.

[71] G. Hasnain, K. Tai, L. Yang, Y.H. Wang, R.J. Fisher, J.D. Wynn, B.E. Weir, N.K. Dutta, and A.Y. Cho, "Performance of gain-guided surface emitting lasers with semiconductor distributed Bragg reflectors", *IEEE J. Quantum Electron.*, vol. 27, no. 6, pp. 1377–1385, 1991.

[72] K. Faltin, *Untersuchungen zur Nahfeldverteilung von Transversalmoden in Laserdioden mit Vertikalresonator*. Ph.D. Thesis, Fakultät für Ingenieurwissenschaften der Universität Ulm, 1998. Published in Berichte aus der Lasertechnik. Aachen: Shaker Verlag, 1999.

[73] K.D. Choquette and R. Leibenguth, "Control of vertical cavity laser polarization with anisotropic transverse cavities", *IEEE Photon. Technol. Lett.*, vol. 6, no. 1, pp. 40–42, 1994.

[74] B. Weigl, M. Grabherr, C. Jung, R. Jäger, G. Reiner, R. Michalzik, D. Sowada, and K.J. Ebeling, "High-performance oxide-confined GaAs VCSELs", *IEEE J. Select. Topics Quantum Electron.*, vol. 3, no. 2, pp. 409–415, 1997.

[75] G. Verschaffelt, W. van der Vleuten, M. Creeusen, E. Smallbrugge, T.G. van der Roer, F. Karouta, R.C. Striijbos, J. Danckaert, I. Veretennicoff, B. Ryvkin, H. Thienpont, and G.A. Acket, "Polarization stabilization in vertical-cavity surface-emitting lasers through asymmetric current injection", *IEEE Photon. Technol. Lett.*, vol. 12, no. 8, pp. 945–947, 2000.

[76] H.P.D. Yang, I.C. Hsu, F.I. Lai, H.C. Kuo, and J.Y. Chi, "High-power single-mode vertical-cavity surface-emitting lasers with multi-leaf holey structure", *Jap. J. Appl. Phys.*, vol. 45, no. 33, pp. L871–L873, 2006.

[77] Å. Haglund, J.S. Gustavsson, J. Vukušić, P. Modh, and A. Larsson, "Single fundamental mode output power exceeding 6 mW from VCSELs with a shallow surface relief", *IEEE Photon. Technol. Lett.*, vol. 16, no. 2, pp. 368–370, 2004.

[78] A. Kroner, F. Rinaldi, J.M. Ostermann, and R. Michalzik, "High-performance single fundamental mode AlGaAs VCSELs with mode-selective mirror reflectivities", *Opt. Comm.*, vol. 270, no. 2, pp. 332–335, 2006.

[79] K. Panajotov, B. Ryvkin, J. Danckaert, M. Peeters, H. Thienpont, and I. Veretennicoff, "Polarization switching in VCSELs due to thermal lensing", *IEEE Photon. Technol. Lett.*, vol. 10, no. 1, pp. 6–8, 1998.

[80] P. Debernardi, A. Kroner, F. Rinaldi, and R. Michalzik, "Surface relief versus standard VCSELs: A comparison between experimental and hot-cavity model results", *IEEE J. Select. Topics Quantum Electron.*, vol. 15, no. 3, pp. 828–837, 2009.

[81] U. Fiedler, D. Wiedenmann, B. Weigl, C. Jung, G. Reiner, M. Buck, and K.J. Ebeling, "Stable linearly polarized light emission from VCSELs with oxidized elliptical current aperture", in Proc. Int. Semiconduct. Laser Conf., ISLC'96, pp. 19–20, Haifa, Israel, Oct. 1996.

[82] U. Fiedler, G. Reiner, P. Schnitzer, and K.J. Ebeling, "Top surface-emitting vertical-cavity laser diodes for 10-Gb/s data transmission", *IEEE Photon. Technol. Lett.*, vol. 8, no. 6, pp. 746–748, 1996.

[83] D.V. Kuksenkov, H. Temkin, and S. Swirhun, "Polarization instability and performance of free-space optical links based on vertical-cavity surface-emitting lasers", *IEEE Photon. Technol. Lett.*, vol. 8, no. 5, pp. 703–705, 1996.

[84] T. Mukaihara, N. Ohnoki, Y. Hayashi, N. Hatori, F. Koyama, and K. Iga, "Excess intensity noise originated from polarization fluctuation in vertical-cavity surface-emitting lasers", *IEEE Photon. Technol. Lett.*, vol. 7, no. 10, pp. 1113–1115, 1995.

[85] R. Mueller, A. Klehr, A. Valle, J. Sarma, and K.A. Shore, "Effects of spatial hole burning on polarization dynamics in edge-emitting and vertical-cavity surface-emitting laser diodes", *Semicond. Sci. Technol.*, vol. 11, no. 4, pp. 587–596, 1996.

[86] M.P. van Exter, A.K.J. van Doorn, and J.P. Woerdman, "Electro-optic effect and birefriengence in semiconductor vertical-cavity lasers", *Phys. Rev. A*, vol. 56, no. 1, pp. 845–853, 1997.

[87] C.J. Chang-Hasnain, J.P. Harbison, G. Hasnain, A.C. Von Lehmen, L.T. Florez, and N.G. Stoffel, "Dynamic, polarization and transverse mode characteristics of vertical cavity surface emitting lasers", *IEEE J. Quantum Electron.*, vol. 27, no. 6, pp. 1402–1408, 1991.

[88] A.K.J. van Doorn, M.P. van Exter, and J.P. Woerdman, "Strain-induced birefrierngence in vertical-cavity semiconductor lasers", *IEEE J. Quantum Electron.*, vol. 34, no. 4, pp. 700–706, 1998.

[89] K.D. Choquette, R.P. Schneider, Jr., K.L. Lear, and R.E. Leibenguth, "Gain-dependent polarization properties of vertical-cavity lasers", *IEEE J. Select. Topics Quantum Electron.*, vol. 1, no. 2, pp. 661–666, 1995.

[90] K.D. Choquette, D.A. Richie, and R.E. Leibenguth, "Temperature dependence of gain-guided vertical-cavity surface emitting laser polarization", *Appl. Phys. Lett.*, vol. 64, no. 16, pp. 2062–2064, 1994.

[91] A.K.J. van Doorn, M.P. van Exter, and J.P. Woerdman, "Elasto-optic anisotropy and polarization orientation of vertical-cavity surface-emitting semiconductor lasers", *Appl. Phys. Lett.*, vol. 69, no. 8, pp. 1041–1043, 1996.

[92] N.P. Patel, J.E. Ripper, and P. Brosson, "Behavior of threshold current and polarization of stimulated emission of GaAs injection lasers under uniaxial stress", *IEEE J. Quantum Electron.*, vol. QE-9, no. 2, pp. 338–341, 1973.

[93] N.K. Dutta, "Effect of uniaxial stress on optical gain in semiconductors", *J. Appl. Phys.*, vol. 55, no. 2, pp. 285–288, 1984.

[94] T. Mukaihara, F. Koyama, and K. Iga, "Stress effect for polarization control of surface emitting lasers", *Electron. Lett.*, vol. 28, no. 6, pp. 555–556, 1992.

[95] T. Mukaihara, F. Koyama, and K. Iga, "Polarization control of surface emitting lasers by anisotropic biaxial strain", *Jap. J. Appl. Phys.*, vol. 31, no. 5A, pp. 1389–1390, 1992.

[96] T. Mukaihara, F. Koyama, and K. Iga, "Engineered polarization control of GaAs/AlGaAs surface-emitting lasers by anisotropic stress from elliptical etched substrate hole", *IEEE Photon. Technol. Lett.*, vol. 5, no. 2, pp. 133–135, 1993.

[97] A. Chavez-Pirson, H. Ando, H. Saito, and H. Kanbe, "Polarization properties of vertical cavity surface emitting laser using a fractional layer superlattice gain medium", *Appl. Phys. Lett.*, vol. 62, no. 24, pp. 3082–3084, 1993.

[98] M. Shimuzi, T. Mukaihara, F. Koyama, and K. Iga, "Polarization control for surface emitting lasers", *Electron. Lett.*, vol. 27, no. 12, pp. 1067–1069, 1991.

[99] T. Mukaihara, N. Ohnoki, T. Baba, F. Koyama, and K. Iga, "A novel birefriengence distributed Bragg reflector using a metal dielectric polarizer for polarization control of surface-emitting lasers", *Jap. J. Appl. Phys.*, vol. 33, no. 2B, pp. L227–L229, 1994.

[100] N. Nishiyama, A. Mizutani, N. Hatori, F. Koyama, and K. Iga, "A complete single-mode and single-polarization vertical-cavity surface emitting lasers grown on GaAs (311)B substrate", *Jap. J. Appl. Phys.*, vol. 37, no. 6A, pp. L640–L642, 1998.

[101] J.M. Ostermann, P. Debernardi, and R. Michalzik, "Surface-grating VCSELs with dynamically stable light output polarization", *IEEE Photon. Technol. Lett.*, vol. 17, no. 12, pp. 2505–2507, 2005.

[102] P. Debernardi, J.M. Ostermann, M. Feneberg, C. Jalics, and R. Michalzik, "Reliable polarization control of VCSELs through monolithically integrated surface gratings: a comparative theoretical and experimental study", *IEEE J. Select. Topics Quantum Electron.*, vol. 11, no. 1, pp. 107–115.

[103] J.M. Ostermann, P. Debernardi, A. Kroner, and R. Michalzik, "Polarization controlled surface grating VCSELs under externally induced anisotropic strain", *IEEE Photon. Technol. Lett.*, vol. 19, no. 17, pp. 1301–1303, 2007.

[104] J.M. Ostermann, P. Debernardi, C. Jalics, A. Kroner, M.C. Riedl, and R. Michalzik, "Surface gratings for polarization control of single- and multimode oxide-confined vertical-cavity surface-emitting lasers", *Optics Communications*, vol. 246, no. 4–6, pp. 511–519, 2005.

[105] Å. Haglund, J.S. Gustavsson, J. Vukušić, P. Modh, and A. Larsson, "High power fundamental mode and polarization stablized VCSELs using sub-wavelength surface grating", *Electron. Lett.*, vol. 41, no. 14, pp. 85–87, 2005.

[106] D. Vakhshoori, "Symmetry considerations in vertical cavity-surface emitting-lasers: prediction of removal of polarization anisotropy on (001) substrates", *Appl. Phys. Lett.*, vol. 65, no. 3, pp. 259–261, 1994.

[107] K. Panajotov, M.-C. Camerena, M. Moreno, H.J. Unold, R. Michalzik, H. Thirnpont, J. Danckaert, I. Veretennicoff, and G. Verschaffelt, "Polarization behavior and mode structure of vertical-cavity surface-emitting lasers with elliptical surface relief", in *Vertical-Cavity Surface-Emitting Lasers VII*, C. Lei, S.P. Kilcoyne (Eds.), Proc. SPIE. 4994, pp. 127–138, 2003.

[108] D.-S. Song, Y.-J. Lee, H.-W. Choi, and Y.-H. Lee, "Polarization-controlled, single-transverse-mode, photonic-crystal, vertical-cavity, surface-emitting lasers", *Appl. Phys. Lett.*, Proc. SPIE. 82, no. 19, pp. 3182–3184, 2003.

[109] K.D. Choquette and R. Leibenguth, "Control of vertical cavity laser polarization with anisotropic transverse cavities", *IEEE Photon. Technol. Lett.*, vol. 6, no. 1, pp. 40–42, 1994.

[110] T. Yoshikawa, H. Kosaka, K. Kurihara, M. Kajita, Y. Sugimoto, and K. Kasahara, "Complete polarization control of 8×8 vertical-cavity surface-emitting laser matrix arrays", *Appl. Phys. Lett.*, vol. 66, no. 8, pp. 908–910, 1995.

[111] T. Yoshikawa, T. Kawakami, H. Saito, H. Kosaka, M. Kajita, K. Kurihara, Y. Sugimoto, and K. Kasahara, "Polarization-controlled single mode VCSEL", *IEEE J. Quantum Electron.*, vol. 34, no. 6, pp. 1009–1014, 1998.

[112] P. Debernardi, H.J. Unold, J. Maehnss, R. Michalzik, G.B. Bava, and K.J. Ebeling, "Single-mode, single-polarization VCSELs via elliptical surface etching: experiments and theory", *IEEE J. Select. Topics Quantum Electron.*, vol. 9, no. 5, pp. 1394–1404, 2003.

[113] H.J. Unold, *Mode Control in Vertical-Cavity Surface-Emitting Laser Diodes*. Ph.D. Thesis, Fakultät für Ingenieurwissenschaften der Universität Ulm, 2003. Published in Berichte aus der Elkctrotechnik, Aachen: Shaker Verlag, 2004.

[114] K. Ladavac, K. Kasza, and D.G. Grier, "Sorting mesoscopic objects with periodic potential landscapes: optical fractionation", *Phys. Rev. E*, vol. 70, no. 1, pp. 010901-1–4, 2004.

[115] C.M. Creely, G. Volpe, G.P. Singh, M. Soler, and D.V. Petrov, "Raman imaging of floating cells", *Opt. Express*, vol. 13, no. 16, pp. 6105–6110, 2005.

[116] A. Ashkin, "Forces of a single-beam gradient laser trap on a dielectric sphere in the ray optics regime", *Biophys. J.*, vol. 61, no. 1, pp. 569–582, 1992.

[117] K.S. Giboney, L.B. Aronson, and B.E. Lemoff, "The ideal light source for datanets", *IEEE Spectrum*, vol. 35, no. 2, pp. 43–53, 1998.

[118] R.A. Morgan, G.D. Guth, C. Zimmer, R.E. Leibenguth, M.W. Focht, J.M. Freund, K.G. Glogovsky, T. Mullally, F.F. Judd, and M.T. Asom, "Two-dimensional matrix addressed vertical cavity top-surface emitting laser array display", *IEEE Photon. Technol. Lett.*, vol. 6, no. 8, pp. 913–917, 1994.

[119] A. Von Lehmen, C. Chang-Hasnain, J. Wullert, L. Carrion, N. Stoffel, L. Florez, and J. Harbison, "Independently addressable InGaAs/GaAs vertical-cavity surface-emitting laser arrays", *Electron. Lett.*, vol. 27, no. 7, pp. 583–585, 1991.

[120] E.G. Paek, J.R. Wullert, M. Jain, A. Von Lehmen, A. Scherer, J. Harbison, L.T. Florez, H.J. Yoo, R. Martin, J.L. Jewell, and Y.H. Lee, "Compact and ultrafast holographic memory using a surface-emitting microlaser diode array", *Opt. Lett.*, vol. 15, no. 6, pp. 341–343, 1990.

[121] M. Naruse and M. Ishikawa, "Parallel confocal laser microscope system using smart pixel arrays", in *Novel Optical Design and Optimization III*, J.M. Sasian, (Ed.), Proc. SPIE 4092, pp. 94–101, 2000.

[122] M. Orenstein, A.C. Von Lehmen, C. Chang-Hasnain, N.G. Stoffel, J.P. Harbison, and L.T. Florez, "Matrix addressable vertical cavity surface emitting laser array", *Electron. Lett.*, vol. 27, no. 5, pp. 437–438, 1991.

[123] K.M. Geib, K.D. Choquette, D.K. Serkland, A.A Allerman, and T.W. Hargett, "Fabrication and performance of two-dimensional matrix addressable arrays of integrated vertical-cavity lasers and resonant cavity photodetectors", *IEEE J. Select. Topics Quantum Electron.*, vol. 8, no. 4, pp. 943–947, 2002.

[124] A.J. Danner, J.C. Lee, J.J. Raftery, N. Yokouchi, and K.D. Choquette, "Coupled-defect photonic crystal vertical cavity surface emitting lasers", *Electron. Lett.*, vol. 39, no. 18, pp. 1323–1324, 2003.

[125] L. Bao, N.-H. Kim, L.J. Mawst, N.N. Elkin, V.N. Troshchieva, D.V. Vysotsky, and A.P. Napartovich, "Near-diffraction-limited coherent emission from large aperture antiguided vertical-cavity surface-emitting laser arrays", *Appl. Phys. Lett.*, vol. 84, no. 3, pp. 320–322, 2004.

[126] A.C. Lehman, J.J. Raftery, Jr., A.J. Danner, P.O. Leisher, and K.D. Choquette, "Relative phase tuning of coupled defects in photonic crystal vertical-cavity surface-emitting lasers", *Appl. Phys. Lett.*, vol. 88, no. 2, pp. 021102-1–2, 2006.

[127] J.J. Raftery, Jr., A.J. Danner, J.C. Lee, and K.D. Choquette, "In-phase evanescent coupling of two-dimensional arrays of defect cavities in photonic crystal vertical cavity surface emitting lasers", *Appl. Phys. Lett.*, vol. 89, no. 8, pp. 081119-1–3, 2006.

[128] A.C. Lehman, J.J. Raftery, Jr., P.S. Carney, and K.D. Choquette, "Coherence of photonic crystal vertical-cavity surface-emitting laser arrays", *IEEE J. Quantum Electron.*, vol. 43, no. 1, pp. 25–30, 2007.

[129] C-M. Zetterling, "*Process Technology for Silicon Carbide Devices*", London: INSPEC, 2002.

[130] R.A. Morgan, G.D. Guth, M.W. Focht, M.T. Asom, K. Kojima, L.E. Rogers, and S.E. Callis, "Transverse mode control of vertical-cavity top-surface-emitting lasers", *IEEE Photon. Technol. Lett.*, vol. 4, no. 4, pp. 375–377, 1993.

Curriculum Vitae

Personal Data

Name	Abdelsattar Mohamed Abdelsattar Gadallah
Birthdate/birthplace	19th August 1974/Fayoum, Egypt
Nationality	Egyptian

Education

since 1/2006	Ph.D. student at Institute of Optoelectronics, Ulm University, Germany
9/1998–12/2001	M.Sc. at NILES[1], Cairo University, Egypt
9/1997–6/1998	Diploma at NILES, Cairo University, Egypt
9/1992–6/1996	B.Sc. in Physics, Cairo University, Egypt
9/1989–6/1992	Secondary School, Fayoum, Egypt
9/1986–6/1989	Prep School, Fayoum, Egypt
9/1980–6/1986	Elementary School, Fayoum, Egypt

Scholarship

1/2006–1/2010	Ph.D. Scholarship of the Egyptian Government

Employment

since 12/2001	Assistant lecturer at NILES, Cairo University, Egypt
4/1997–12/2001	Demonstrator at NILES, Cairo University, Egypt

[1]NILES is an acronym of the words National Institute of Laser Enhanced Sciences